UNIVERSITA' DEGLI STUDI DI NAPOLI FEDERICO II

Scuola Politecnica e delle Scienze di Base

DIPARTIMENTO DI STRUTTURE PER

L'INGEGNERIA E L'ARCHITETTURA

CORSO DI LAUREA MAGISTRALE IN

INGEGNERIA STRUTTURALE E GEOTECNICA

TESI DI LAUREA

NUMERICAL MODELLING AND EXPERIMENTAL BEHAVIOUR OF "BOZZO SHEAR LINK" DISSIPATORS

RELATORE

Chiar.mo Prof. Ing. Giorgio Serino

CORRELATORE

Chiar.mo Prof. Ing Luis M. Bozzo

Dott. Ing. Daniele Losanno

CANDIDATO

Fabiana Cocozza

matr. M56/376

ANNO ACCADEMICO 2015/2016

Alla mia meravigliosa famiglia

ABSTRACT

This work of thesis has been developed during an internship at the professional office "Luis Bozzo, Estructuras y proyectos, S.L.", in Barcelona, in the context of the Erasmus Placement project.

It is focused on the study of Bozzo Shear Link energy dissipation devices, that are being used for new design or seismic retrofit of reinforced concrete structures in Peru. This type of dissipator belongs to metallic yielding devices group and it is obtained from a mild steel plate milled in some parts called "windows", that represent the yielding dissipative part of the device. Their principal benefit is the low cost of production. This would represent an advantage because of the development in progress and the high seismic risk of Peruvian country, that explains the need to realize a huge number of low cost seismo-resistant residential buildings. The SLB devices could be located in diagonal braces or between chevron braces and an upper beam. The present thesis describes an experimental campaign conducted at University of Naples Federico II on a few specimens and a first attempt of numerical modelling of the device mechanical behaviour.

The work is organized in five different chapters.

Chapter 1 describes the actual level of knowledge, showing the significant points of the seismic design of structure.

Chapter 2 provides a description of several seismic design procedures, differentiating conventional seismic design, based on the capacity design criterion, and seismic control systems. The attention is focused on Bozzo Shear Link energy dissipation devices, that are described into details in terms of geometry and mechanical expected behaviour .

Chapter 3 introduces the experimental campaign conducted at University of Naples Federico II to test some specimens of Bozzo Shear Link device, describing the geometry of each and the property of the material. At the beginning, a tensile test on the constitutive material was performed to obtain the constitutive law. Then, five kinds of SLB are tested, differing in terms of web dimensions and thickness of milled area. Two specimens for each kind of device were tested. A brief description of the testing machine and the properly designed setup with the measurement equipment, used to realize the experimental campaign, is provided. The realisation of ad hoc set up has been necessary in order to transmit the design shear force to the device while preserving the machine from being transmitted high level of stress, both in terms of bending and shear force. In addition to this, the boundary and load conditions of each device are

described,. The specimens have been tested changing the boundary conditions at the slotted holes and the load condition in terms of monotonic or cyclic test. At the end of the chapter experimental results are shown and analysed, obtaining design parameters and considerations about the strain distribution and deformation at collapse. Main results are summarized into tables.

Chapter 4 introduces a FEM numerical model of Bozzo Shear Link energy dissipation device; numerical models correspond to real tested specimens in terms of both geometry and material properties. The constitutive stress-strain law of the material is obtained from the nominal one with application of the corrective Bozzo's formula to get the effective stress-strain relation. In order to model the cyclic behaviour, the adopted plasticity models described in terms of constitutive parameters and calibration process. At this point a thorough investigation of devices nonlinear behaviour has been performed implementing a FEM model. Geometry of devices is first defined with the drawing program AutoCad and then imported in the software Ansys Workbench. The boundary and the load conditions in the numerical model replicate the experimental ones.

The numerical results are analysed and commented for each case, then a comparison with experimental results is proposed. This comparison contributes to validate the numerical model and calibrate numerical parameters in order to define a more accurate numerical model.

Chapter 5 is the last chapter of this thesis, where the main conclusions are summarized: the present work shows the experimental campaign of Bozzo Shear Link energy dissipation devices and their numerical modelling. The comparison between experimental response and numerical predicted one allows to draw conclusions about the accuracy of the numerical model and the points to further investigate in next future.

NUMERICAL MODELLING AND EXPERIMENTAL BEHAVIOUR OF "BOZZO SHEAR LINK" DISSIPATORS

C**ontents**

List of figures

List of tables

1 INTRODUCTION

1.1 Seismic design

The seismic design of structures is intended to prevent the collapse of the buildings and loss of human lives in case of an strong earthquake.

The modern codes of design accept the presence of a certain level of damage, that not endanger the stability of the buildings, in order to build economic structures.

The presence of damage to some elements of a structure under the action of a severe earthquake is due to the conventional seismic design based on the concepts of ductility and structural redundancy, that allows significant reduction in the forces induced by a severe earthquake. However, with the reduction of these forces and the presence of damages, the structure can work in the non linear range with the consequent yielding of some of its elements. This originates the appearance of permanent deformations, which usually generates damages in the structural and non-structural elements, especially in those structures that have low ductility, or they are very flexible.

The development of the seismic design of structures is based on experimentation and observation of the damages that occur in construction situated in seismically active areas. Through the experimental studies it was possible to improve and to correct the design methods, in order to achieve the purpose above mentioned.

The conventional seismic design is based on the concept of "capacity design", founded on ductility and structural redundancy. According to this criterion, energy is dissipated by the non linear behaviour of the structure, whose elements must be designed to allow the most dissipative performance. Theoretically there are two complementary ways of designing a seismic-resistant building without the use of particular devices, which is focusing on strength or on ductility

capacities of the structure. On one hand the building could be designed in such a way to be able to withstand the whole seismic action, assuming a linear behaviour and avoiding damages in the structure. This simplification permits a simple approach to the problem, using the modal superposition of the method of dynamic analysis, applicable to many practical situations.

On the other hand, ensuring a certain level of structural ductility and admitting structural damage, it is possible to design buildings considering a seismic action reduced by a factor R, which is between 1 and 10 in the American Uniform Building Code (UBC). The value of R depends on materials and structural systems devoted to adsorb lateral actions. This way to design implies that damages are admitted after a strong ground motion in structural elements since it is expected a nonlinear behaviour of the structure.

The main aspect to note is that the analysis is based on a linear elastic response which directly reduces the forces neglecting the nonlinear nature of the problem. This simplification permits a simple approach to the problem, using the modal superposition of the method of dynamic analysis, applicable to many practical situations.

However, this approach has several disadvantages, for example the global ductility demand may require a large local ductility and therefore the local failures may occur. In addition, the high reduction of forces involves structural damage (non-structural damage is controlled by limiting the displacement of the interstory drift) whose repair can be expensive after a strong earthquake. Finally the minimum steel reinforcement required to provide the local ductility to all elements, results an additional cost.

An alternative approach to improve the simplification mentioned is the development of structural systems which localize the non-linear response of the structure.

Examples of these systems in reinforced concrete structures are coupled walls or eccentric braces in frames of metal structures (Bozzo and Barbat, 1999). In the first system the "link" or connection between seismic walls works as a "fuse" that controls the response during earthquakes. Similarly in the second system horizontal element between the diagonal elements provides a ductile response based on stable hysteretic response of the steel under shear stress. Both alternatives have two big disadvantages: because the interaction with the adjacent elements can modify the ideal response of "seismic fuse" or "link" and they are difficult to repair because they are an integral part of the global structure.

Moreover, the alternatives for seismic design using the base-isolation (Naeim et al., 1999) and energy dissipation developed in the '80s. The base isolation is a technique used for lower

buildings, it allows a significant reduction of seismic forces changing the fundamental natural period of the building or introducing a low friction interface which limits the forces transmitted to the super-structure.

There are hundreds of buildings constructed with this technique, however, they have some important disadvantages. Among those, the nonlinear response of the super-structure can be influenced by connection of base isolation (Ordonez et al., 2003); the cost increases; it has to provide a flexible joint (every 90-120 cm) around the structure; the effectiveness is reduced when the number of floors (or the natural period) is increased.

Moreover the energy dissipators are convenient alternatives for medium or high structures because not require sophisticated analysis or special construction techniques. There are different kind of systems such as ADAS (Scholl R, 1993) or the "Honeycomb" (Kobori et al., 1992).There are also many examples of structures equipped with these systems. The seismic force reduction for the buildings which use these systems, traditionally, is assumed because the damping. For this reason, these systems are also called dampers.

However, it is known that the seismic forces reduction, which is achieved, by a significant increase of damping of the structure, is not significant, particularly compared to the achieved reductions by providing ductility. Figure 1.1 shows the reduction of the ductility demand achieved for the increment of structural damping, from 2 to 10%.

Clearly, this reduction is not significant and, for example, for a period T = 1s, the reduction is only 20%.Figure 1 (b), where $\gamma = K_2 / K_1$ (hardening coefficient) and ξ is the fraction of critical damping, shows the reduction of the seismic forces that provides ductility.

The R factor represents the relationship between the linear and nonlinear forces for different levels of ductility. This figure shows significant reductions for the all values of period which are considered, particularly for T> 0.5 s with maximum values of R = 20.

Because of this, adding damping at the energy dissipators produces a small reductions of the seismic force with respect to the base isolation or the design based on the ductility.

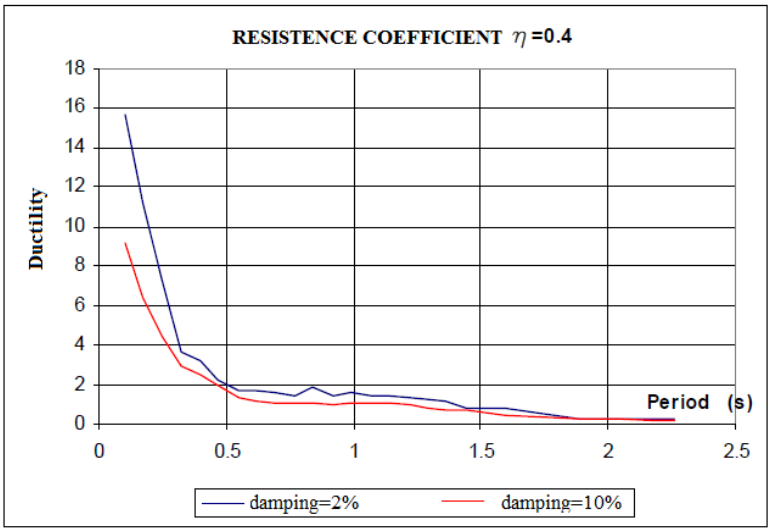

Figure 1.1 Reduction of seismic force due to an increase in damping of five times. Loma Prieta Earthquake

For all of these reasons this thesis proposes an innovative concept based on conventional seismic design and massive use of energy dissipators.

1.2 Development of the thesis

After to show different kind of energy dissipator, the attention has been focused on Bozzo's shear links. In particular, the goal is to find a numerical model which is closed as possible as to the real behaviour of devices. In this way it is possible to predict nonlinear behaviour through the definition of some parameters that are elastic stiffness, yielding force and post yielding stiffness ratio. An experimental campaign will be realized in order to compare numerical values with real values, in this way it is possible to calibrate numerical parameters in accurate way.

The experimental tests have been performed at the Laboratory of Dist, University of Naples "Federico II". Five kinds of devices are tested, two specimens for device. This has allowed to compare the behaviour of device under different load, monotonic and cyclic, and for different condition, fixed-fixed and fixed-nofixed, which are realized tightening and not tightening one extreme of the device. The experimental model was manufactured whit conventional structural steel.

The set-up ad hoc has been designed in order to perform these tests, avoiding that the buckling failure occurs before than the shear failure occurs.

The nonlinear analysis has been performed using the software Ansys Workbench, based on the use of monotonic and cyclic load history.

At the beginning the material properties have been defined, consequently, the constitutive law, tension-deformation implemented into Ansys, has been defines. It was possible through a tensile test on the specimen, which has performed at Laboratory of Dist, University of Naples "Federico II".

The second step consists into a research of the constitutive model has done, in fact a simple model of kinematic hardening didn't describe well the real behaviour, because it didn't take in account the "isotropic effect", which the device shows. The more appropriate plastic model is Chaboche model, which is defined through two parameters, C_1 and γ_1. Different analysis were performed in order to find the "correct" Chaboche's parameters.

After to define the material properties and the model of plasticity, the nonlinear numerical analysis have been done, in particular monotonic analysis and cyclic analysis.

The monotonic analysis permits to evaluated elastic stiffness, yielding force, post yielding stiffness ratio, maximum force.

In the end the numerical and the experimental results have been analysed and commented.

2 SYSTEMS OF STRUCTURAL CONTROL FOR THE SEISMIC PROTECTION

2.1 Introduction

In recent decades a lot of research about the structural behaviour of buildings located in seismic areas, have focused on the development of seismic control systems, both for the seismic design of new construction and for the rehabilitation of damaged buildings because this phenomena. This is an alternative to conventional seismic design based on the concepts of ductility and structural redundancy, which allow significantly reduction of forces due to a severe earthquake.

However, the reduction of these forces involves that the structure will suffer damage of a certain magnitude when a strong earthquake occurs; consequently there will be the plasticization of some part of structure so the structure will work in no-linear range.

The plasticization produces permanent deformations which cause damage for the structural and no structural elements (such as masonry partition walls mechanical equip, installations..), especially in the structures with low ductility or very flexible structures.

Instead the systems of structural control concentrate the damage, due to the action of a severe earthquake, in certain elements or connections; these can be easily replaced and them failures don't endanger the global safety of structures. They can deviate the seismic motion from the structure to the others elements which are designed for it, so that the vibrations caused by the earthquake, do not damage the buildings and can be damped. Another systems based on this technique are the mechanical devices which exert reactive forces that counteract the seismic action on structures.

Research has devoted to the study of four structural control systems which are classified into passive control systems, active control, semi-active control and hybrid control. They are discussed below .

In this chapter differences between these designing procedures are discussed, focusing on the shear link energy dissipation device.

2.2 Seismic control system

In recent years research is mostly oriented towards finding systems withstanding seismic action alternative to the traditional approach, based on the capacity design. Nowadays there are many different techniques available to carry out this task, working according to different principles: decrease of the seismic energy input modifying dynamic structural properties; increase of energy dissipation through the use of mechanical devices that can dissipate hysteretic or viscous energy; increase of dissipated energy introducing control force.

The state-of-art distinguishes passive and active control systems. The main difference among them consists in the fact that the passive protection doesn't need the activation of their operating, contrarily to the case of active control systems, that require external source of energy in order to work. Passive systems encompass a range of materials and devices for enhancing structural damping, stiffness and strength, and can be used both for seismic hazard mitigation and for rehabilitation of aging or deficient structures. In general, such systems are characterized by their capability to provide energy dissipation in the structural systems in which they are installed.

These devices generally operate on principles such as frictional sliding, yielding of metals, deformation of visco-elastic (VE) solids or fluids and fluid orificing. Active systems, which include active, hybrid and semi-active systems, are a natural evolution of passive control technologies. The possible use of active control systems and some combinations of passive and active systems as a means of structural protection against seismic loads has received considerable attention in recent years. Active/hybrid/semi-active control systems are force delivery devices integrated with real-time processing evaluators/controllers and sensors within the structure. They act simultaneously with the hazardous excitation to provide enhanced structural behaviour for improved service and safety.

In order to describe differences between various seismic control systems consider the single degree of freedom system (SDOF) of Figure 2.1, consisting of a mass m, supported by columns characterized by a total linear elastic stiffness k, and a damper with damping coefficient c. Consider the addition of a generic passive energy dissipation and a generic active control system. This SDOF system is then subjected to an earthquake load, where $\ddot{x}_g(t)$ is ground acceleration, and to other possible horizontal actions F(t), such as wind. The excited model responds with a lateral displacement x(t) relative to the ground (Soong et al. 2002).

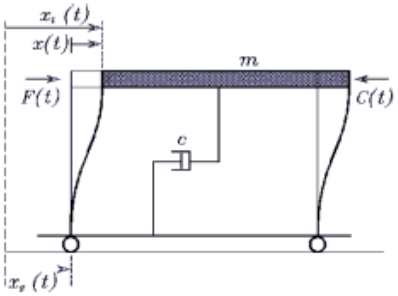

Figure 2.1 SDOF system

The equation of motion of this system is:

$$m\ddot{x} + c\dot{x} + kx + \Gamma x = -m\ddot{x}_g + F(t) - C(t) \quad \textbf{(2.1)}$$

Where Γx is the force corresponding to the device (Γ representing a generic intergro-differential operator) and C(t) is the control force.

Manipulating this equation the energy balance relation is obtained as follows:

$$E_k(t) + E_\xi(t) + [E_E(t) + E_H(t)] + E_I^C(t) = E_I^S(t) + E_I^F(t) \quad \textbf{(2.2)}$$

Where:

$E_k(t)$ is the kinetic energy,

$E_\xi(t)$is energy dissipated by damping,

$[E_E(t) + E_H(t)]$ is the structural adsorbed energy (elastic and hysteretic),

$E_I^C(t)$ is the energy dissipated by the control force

$E_I^S(t) + E_I^F(t)$ represent input energies due to earthquake and other external forces-

From the previous equation it is clear that energy balance may be satisfied reducing input energy or increasing structural capacity of dissipating energy. The input energy decreasing can be obtained by the employment of base isolation system, that belongs to passive energy dissipation techniques and generate an elongation of the structural fundamental period of vibration, thus providing a reduction of seismic action. On the other hand dissipated energy can be increased by introducing passive or active protection systems, as it will be illustrated in following paragraphs.

2.3 Passive control system

They are reactive elements which are connected to the structure such as to dissipate and / or divert the energy of seismic action. They not need to some energy source to work. Passive systems are more economical, simple, robust and reliable than the others systems; they are very efficient if designed appropriately and if the earthquakes are very similar to the expected features.

The efficiency of these systems is based on the reduction of the seismic demand on the elements of the structure, improving the energy dissipation capacity and doing that during the earthquake the structure remains into elastic linear range without significantly damage; contrarily to the conventional design which increases the energy dissipation capacity with the plasticization of the elements that dissipate the energy.

Passive control systems allow the reduction of the structural response to seismic input providing additional energy dissipation capacities or modifying dynamic structural properties. Indeed three different subgroups belonging to this type of control system can be identified:

1) base isolation

2) additional energy dissipation,

3) tuned mass/liquid damper

whose different working principles will be described in following paragraphs. It is important to highlight that the common feature of different passive protection systems is that their operation is activated by the structure's motion: thus they work in feedback, as Figure 2.2 depicts, not requiring any external source of energy.

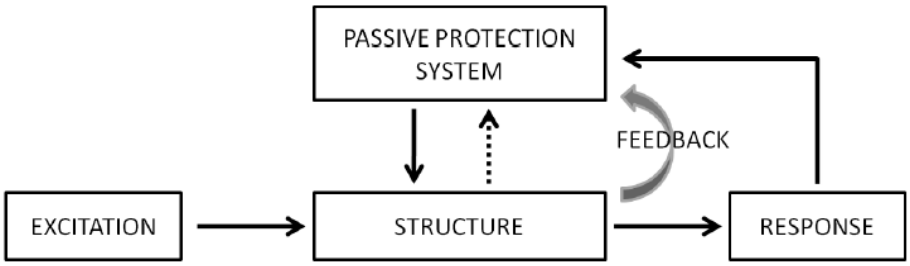

Figure 2.2 Passive control system working principle

The presence of the external excitation generates the structure's relative displacements that actuate the action of passive energy dissipation systems; consequently their action reduces the structural response.

2.3.1 Seismic base isolation

The main objective of seismic base isolation is to isolate the structure from horizontal ground accelerations, by allocating, between the top of foundation and the superstructure, dispositive which are flexible for the horizontal motion and rigid for vertical motion; they are capable of supporting the vertical loads due to the weight of structure.

They are used to limit the values of displacement of the superstructure. This kind of system is for the protection of the buildings and bridges from the earthquake, it doesn't provide security from the wind.

The base isolation systems are not both for the slender buildings and for the buildings placed on soft soil. They are used for the rigid structures founded on rigid soil, because the isolators increase the fundamental period of structure. In this case the resonance effects could occur.

The base isolation systems are also used for the seismic rehabilitation of the existent structures but in this case the complexity is greater than the case of new structures.

The Figure 2.3 shows the behaviours of two different structures under the action of severe earthquake: the first (a) is conventional building without base isolation system and the second (b) is with the base isolation system.

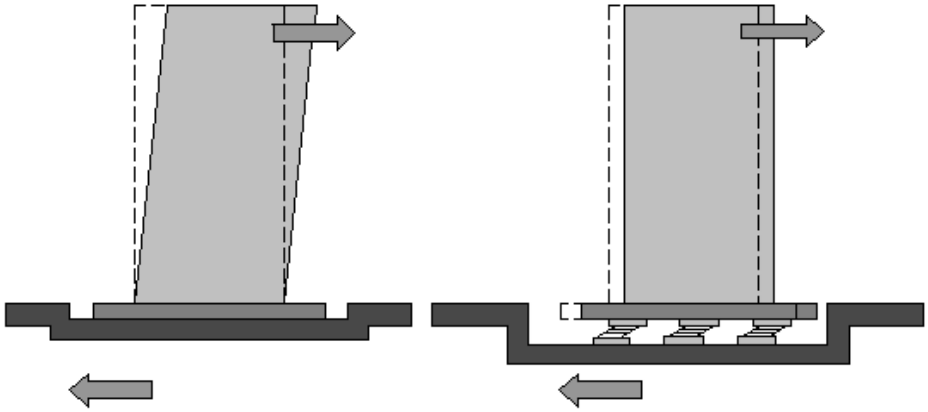

Figure 2.3 fixed base building (a) and isolated building (b)

The modern base isolation systems are the outcome of ancient system's development. It is known that from the beginning of the century there were several mechanisms to achieve the goal of to isolate the buildings from the action of earthquakes, using metal rollers, steel balls, oscillating columns wires and layers of sand.

There are some buildings that are isolated at their base by metallic spheres with small diameter, which are placed between the superstructure and foundation. Examples of this kind of systems are building in Sevastopol, Ukraine and a school of five floors in the City Mexico. Another example is the four-storey building for dormitories seismological observatory of Beijing which is isolated by a sand layer, placed between the superstructure and the foundation, designed to slide when a severe seismic event occurs.

The first types of base isolation devices introduced in last decades is the rubber bearing isolator: it consist in circular, square or rectangular cross section elements, constituted by the alternation of neoprene and steel shits that provide an impediment to the lateral rubber bulging (see Figure 2.2). In fact it is well-known that rubber is an incompressible material, characterized by a Poisson modulus ν=0.5; so, subjected to the gravitational load of the building the bearing could bulge. This element can deform just horizontally, thus there is no isolation in vertical direction; generally this is not a problem since the most danger and damaging stresses are due to the horizontal component of ground motions. In fact the vertical component just increases of a certain percentage vertical loads, but the structure is already designed to carry them. There are different types of rubber bearing according to the kind of connection between the device and the foundation:

- bolted bearing

- dowelled bearing.

In the first case the rubber bearing element is inserted between two thicker steel plates that allow the connection to the rest of the structure through bolting. The dowelled bearing, on the other hand, provides a shear connection since the bearing is inserted in a steel element. Thus the main difference between these two types of connection is that the bolted one works both in tension and in compression, while the dowelled bearing cannot sustain tension loads. For this reason in the case of very high-rise buildings, in which the overturning moment is significant, bolted bearings are necessary. Although it is important to consider that rubber can partially sustain tension since after a time it could be proven. So, when tension stresses in foundation are not expected it is better to employ dowelled bearings. A further distinction can be done between High Damping Steel Laminated Rubber Bearing (HDLRB) and Low Damping Steel Laminated Rubber Bearing (LDLRB), that respectively provide a damping ratio around 10-15% in the first case, and 5% in the second.

However this kind of isolation system gives more flexibility to the structures but not high energy dissipation capacity. For this reason it is combined with others elements as energy dissipaters or dampers to generate a more efficient system which is flexible (so the values of displacements are smaller) and able to dissipate energy at the base.

The Figure 2.4 shows the interior and exterior scheme of these kinds of isolators.

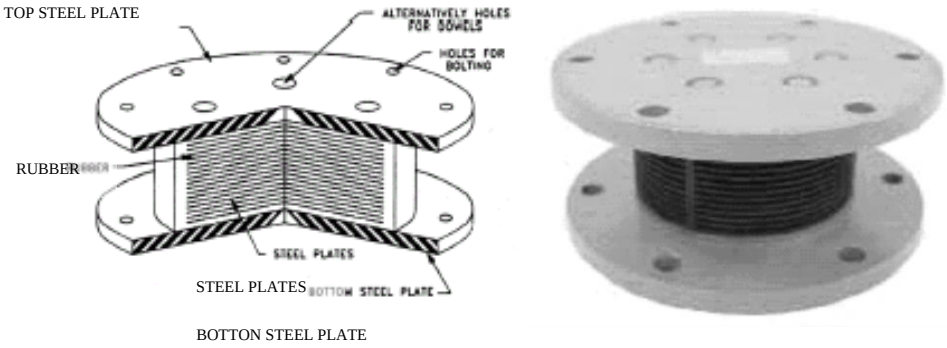

Figure 2.4 Rubber isolators reinforced with thin steel plates (RB)

In order to limit the displacements of the isolation system, in the last years a new system was developed, it is very similar to the previous but with addition of lead core (it is called LRB "Lead Rubber Bearings"). This system is very efficient with respect the previous system

because increases, considerably, the energy dissipation capacity and gives better control of base displacements.

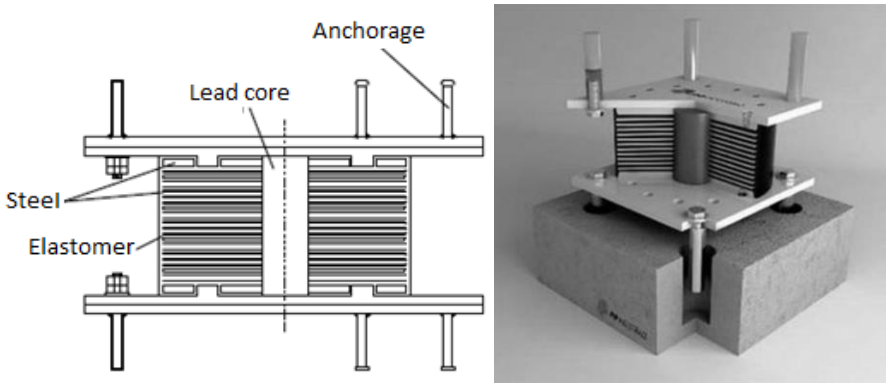

Figure 2.5 Lead Rubber Bearings

An alternative type of isolation device is given by friction isolation devices. In this case the structure is supported by sliding seals which frictional forces oppose to the structural movement dissipating energy. The main parameter in this type of isolation system is the coefficient of friction relative to the contact surfaces and its main advantage is the cost and the absence of limitation to the allowable vertical load to be transmitted. One example of frictional isolation system is the friction pendulum (FPS), depicted in Figure 2.6.

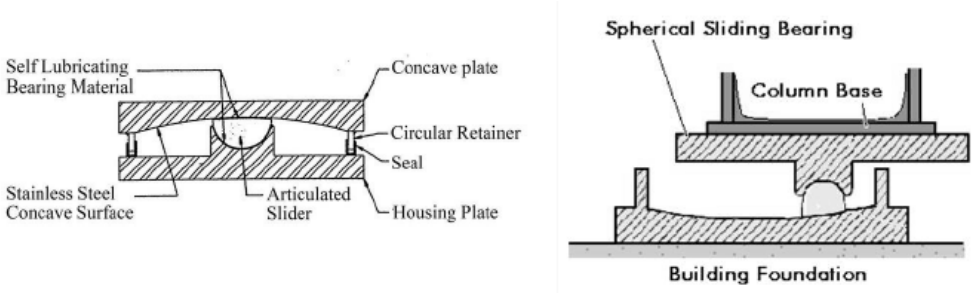

Figure 2.6 Friction pendulum system

This system consists of two sliding plates characterized by curved surfaces covered with a layer of stainless steel; between them there is an articulated slider that can move on the curved surfaces. The side of the slider in contact with the spherical surfaces is coated with a low friction material. Friction pendulum bearings use characteristics of a pendulum to lengthen the natural period of the isolated structure so that to reduce earthquake forces. The curved shape of FPS surfaces enables the structure to return to its initial position after the action of an

earthquake, using the weight of the structure itself. This is an advantage respect to other devices, not having a restoration force allowing the structure to go back to its original position, thus causing significant permanent displacements.

The Figure 2.7 shows a detail of installation in the real case

Figure 2.7 Friction pendulum system in the real case

There is another isolation system called GERB (three dimensional), which was developed in order to isolate the vibration caused by turbine. This device uses big steel coiled springs which are flexible in horizontal and vertical direction (Naeim & Kelly, 1999). This device is also used to isolate structures which have particular equipment, from the vibrations caused by vehicular traffic or subways.

The following Figure 2.8 shows the GERB device and its application in Hospital Sant Pau in Barcelona.

Figure 2.8 Base isolation device to the vibrations (GERB) and its application in Hospital San Pau (Barcelona)

Actually the base isolation devices are used in particular in the regions which have high seismic risk. There are a lot of examples are in USA and Japan, where the structures equipped with this system, have shown a good behaviour during the Northridge and Kobe earthquake, respectively. There are also structures equipped with base isolation devices in New Zealand and Italy.

2.3.2 Additional energy dissipation devices

A large number of passive control systems has been developed and installed in structures for performance enhancement under earthquake loads. These devices provide additional damping to the structure, thus increasing dissipated energy. The seismic action stressing a structure equipped with energy dissipation devices is concentrated in the devices themselves, thus avoiding damages to the rest of the structure's elements that remain essentially elastic. With respect to the case of base isolation systems, energy dissipators do not have to carry the structural weight, thus allowing easier, smaller and cheaper elements.

Furthermore their eventual substitution after a strong earthquake requires a less invasive intervention since their location is not at the interface between the bottom of the structure and foundation system. Indeed they are generally located in steel braces connecting two adjacent floors or between wall infills and beams since their correct operating needs large relative displacements under earthquake motion. The components and connections transferring forces between energy dissipation devices shall be designed to remain linearly elastic.

The employment of energy dissipation devices provides a reduction of bending moment and shear forces acting in columns next to braces. The drawback is that dissipative braces also generate an increasing of the axial force and sometimes of the base shear, thus requiring a local strengthening to the foundation system.

Energy dissipation systems may be considered in a somewhat broader context than isolation systems. For example for the taller buildings (where isolation systems may not be feasible) energy dissipation systems should be considered as a valid design strategy.

A large number of passive control systems has been developed and installed in structures for performance enhancement under earthquake loads. These devices provide additional damping to the structure, thus increasing dissipated energy. The seismic action stressing a structure equipped with energy dissipation devices is concentrated in the devices themselves, thus avoiding damages to the rest of the structure's elements that remain essentially elastic. With

respect to the case of base isolation systems, energy dissipators do not have to carry the structural weight, thus allowing easier, smaller and cheaper elements. Furthermore their eventual substitution after a strong earthquake requires a less invasive intervention since their location is not at the interface between the bottom of the structure and foundation system. Indeed they are generally located in steel braces connecting two adjacent floors or between wall infills and beams (see Figure 2.7) since their correct operating needs large relative displacements under earthquake motion. The components and connections transferring forces between energy dissipation devices shall be designed to remain linearly elastic.

The employment of energy dissipation devices provides a reduction of bending moment and shear forces acting in columns next to braces. The drawback is that dissipative braces also generate an increasing of the axial force and sometimes of the base shear, thus requiring a local strengthening to the foundation system.

Energy dissipation systems may be considered in a somewhat broader context than isolation systems.

For example for the taller buildings (where isolation systems may not be feasible) energy dissipation systems should be considered as a valid design strategy; moreover they could be useful for control of building response due to small earthquakes, wind or mechanical loads.

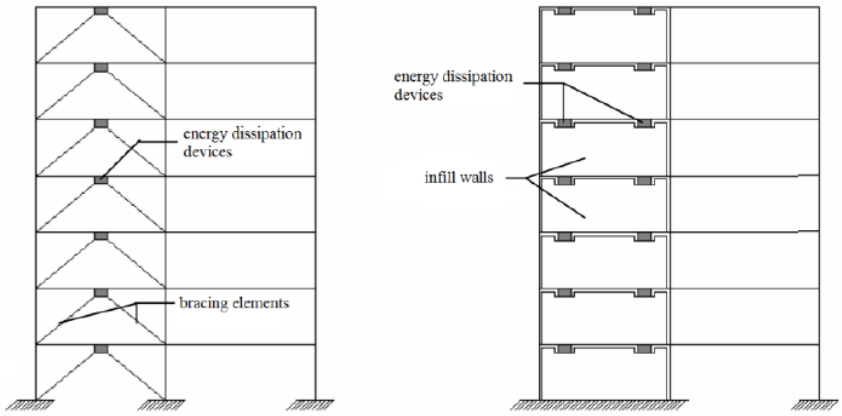

Figure 2.9 Connection between energy dissipation devices and structure

The response of damped structure depends on the choice of the device. Indeed some systems offer only damping (purely viscous), while others also stiffness.

According to the American FEMA 273 (Federal Emergency Management Agency) "NEHRP Guidelines for the seismic rehabilitation of buildings", energy dissipation devices are classified as either displacement-dependent, velocity-dependent, or other. Displacement-dependent devices may exhibit either rigid-plastic (friction devices), bilinear (metallic yielding devices), or trilinear hysteresis. The response of displacement-dependent devices should be independent of velocity and/or frequency of excitation, thus they are also called rate-independent. The force-displacement response of a displacement-dependent device is primarily a function of the relative displacement between each end of the device. Figure 2.10 shows force-displacement relations for displacement-dependent devices.

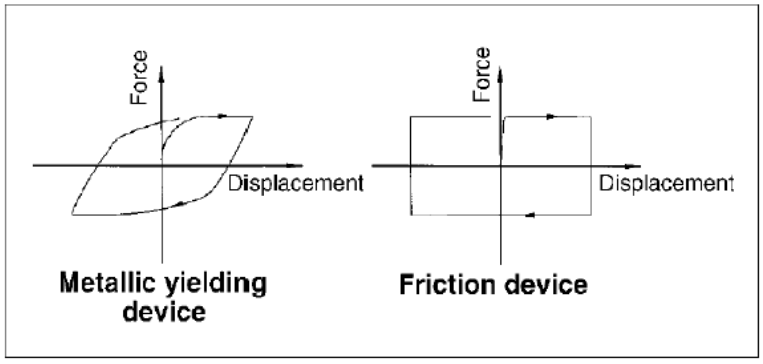

Figure 2.10 Idealized force-displacement loops of displacement-dependent energy dissipation devices (from FEMA 273)

As it is clear from the name, velocity-dependent devices response depends on the velocity of excitation; they are also known as rate-dependent devices and include solid and fluid visco-elastic devices, and fluid viscous devices, that respectively consist in dampers operating by deformation of visco-elastic fluids and dampers operating by forcing a fluid through an orifice. In Figure 2.11typical behaviour of these devices are depicted.

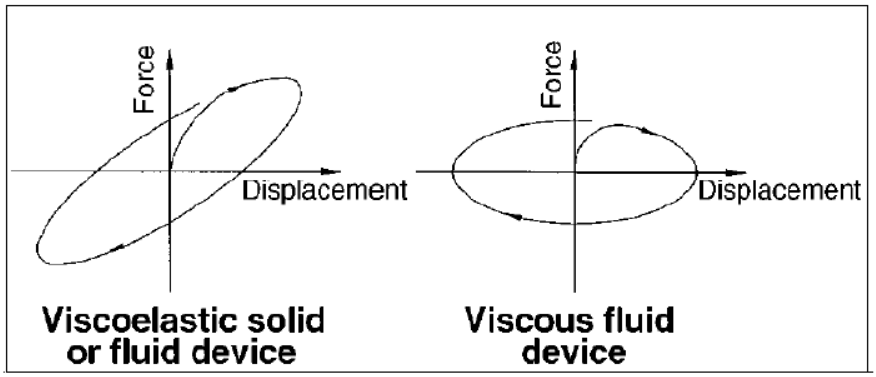

Figure 2.11 Idealized force-displacement loops of velocity-dependent energy dissipation devices (from FEMA 273)

The third classification (other) includes all devices that cannot be classified as either displacement or velocity-dependent. Examples of "other" devices include shape-memory alloys (superelastic effect), friction-spring assemblies with recentering capability, and fluid restoring force-damping devices. Figure 2.10 presents force-displacement relations for these devices, which dissipate energy while providing recentering capability, and resist motion with a nearly constant force.

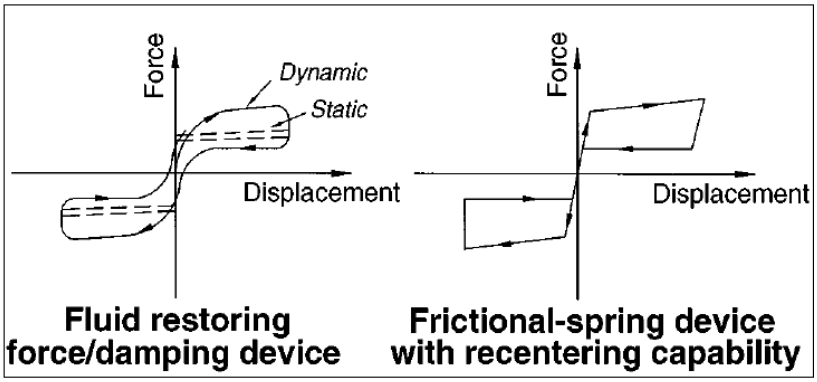

Figure 2.12 Idealized force-displacement loops of energy dissipation devices with recentering capability (from FEMA 273)

Metallic-yielding, friction and visco-elastic energy dissipation devices typically introduce both stiffness and damping; viscous dampers generally only increase the damping in a building frame.

Table 2.1 shows a schematic plan of different energy dissipation devices that will be illustrated in the following paragraphs.

	Viscous Fluid Damper	Viscoelastic Solid Damper	Metallic Damper	Friction Damper
Basic Construction			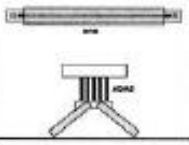	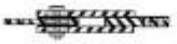
Idealized Hysteretic Behavior	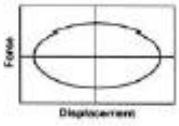	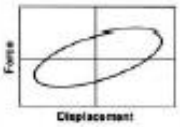	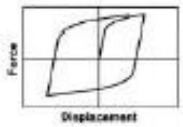	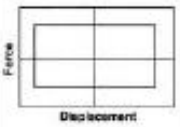
Idealized Physical Model	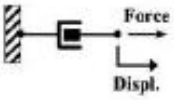	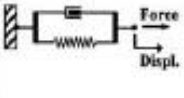	Idealized Model Not Available	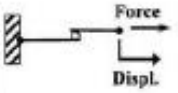
Advantages	- Activated at low displacements - Minimal restoring force - For linear damper, modeling of damper is simplified. - Properties largely frequency and temperature-independent - Proven record of performance in military applications	- Activated at low displacements - Provides restoring force - Linear behavior, therefore simplified modeling of damper	- Stable hysteretic behavior - Long-term reliability - Insensitivity to ambient temperature - Materials and behavior familiar to practicing engineers	- Large energy dissipation per cycle - Insensitivity to ambient temperature
Disadvantages	- Possible fluid seal leakage (reliability concern)	- Limited deformation capacity - Properties are frequency and temperature-dependent - Possible debonding and tearing of VE material (reliability concern)	- Device damaged after earthquake; may require replacement - Nonlinear behavior; may require nonlinear analysis	- Sliding interface conditions may change with time (reliability concern) - Strongly nonlinear behavior; may excite higher modes and require nonlinear analysis - Permanent displacements if no restoring force mechanism provided

Table 2.1 Plan of several energy dissipation devices (from Symans et al., 2008)

2.3.2.1 Rate-independent devices - metallic yielding dampers

One of the effective methods available for the dissipation of energy input in a structure due to seismic action is through inelastic deformation of metals under cyclic loads. Many metallic yielding devices use mild steel plates because of its relatively high stiffness in the elastic field and high energy dissipation potential in the post-yielding field.

Moreover steel plates used are generally of few inches so that to promote metal yielding. These devices ensure a high energy dissipation thanks to stable hysteretic loops that have been

observed during many experimental campaigns, whose results are reported in the state-of-art. Furthermore they provide long term reliability and they are insensitive to environmental temperature. Because of their excursion in the plastic field under the action of a strong earthquake, after their operating they present permanent deformations thus requiring their substitution. This is a disadvantage, but the other side of the coin is that they are cheap and their replacement is generally easy.

Among metallic yielding dampers, according to stresses acting in them and generating their yielding, it is possible to distinguish flexural devices, such as ADAS or TADAS, and shear devices, that include shear link energy dissipation device, that will be widely illustrated in following paragraph.

ADAS, that stands for Added Damping And Stiffness, provides both initial elastic stiffness as well as hysteretic energy dissipation. The ADAS element is a mechanical device made of steel X-shape plates connected at the top and at the bottom to rigid elements so that the rotation is not allowed. The particular shape of steel plates ensures a uniform yielding in the element. The ADAS device is generally inserted between girders brace members (Figure 2.13). It can be installed at specific locations of either new or existing buildings.

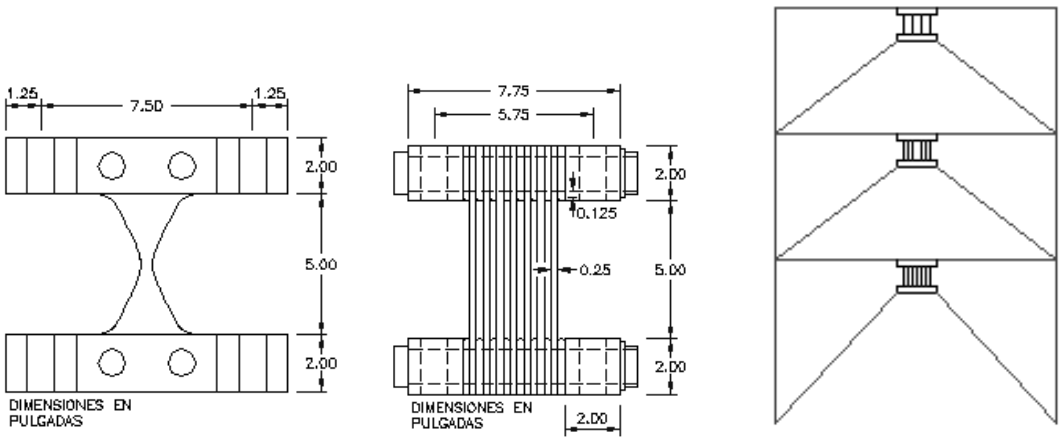

Figure 2.13 ADAS device

As the building oscillates, the inter-storey drift causes the top of the plate to move horizontally relative to the bottom and the energy can be dissipated through the yielding of plates.

Alternatively to the X-shape plates, it is possible to employ triangular plates: this is the case of TADAS (Triangular Added Damping And Stiffness). The advantage of using this shape is that when the free end of the triangular plate is subjected to a concentrated load, it will yield

uniformly over its height, and the plastic deformation will be distributed uniformly over the height of the plate.

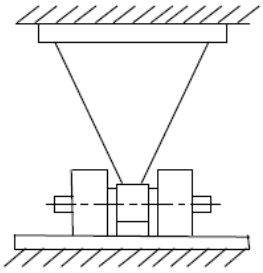

Figure 2.14 TADAS system (Tsai 1993)

A variation of the devices described above but operating on the same metallic yielding principle is the tension/compression yielding brace, also called unbonded brace or buckling restrained brace (BRB), which has found applications in Japan and USA. As shown in Figure 2.15, an unbonded brace is a bracing member consisting of a core steel plate encased in a concrete-filled steel tube. A special coating is provided between the core plate and concrete in order to reduce friction and allow the steel brace elongation. The core steel plate provides stable energy dissipation by yielding under reversed axial loading, while the surrounding concrete-filled steel tube resists compression buckling.

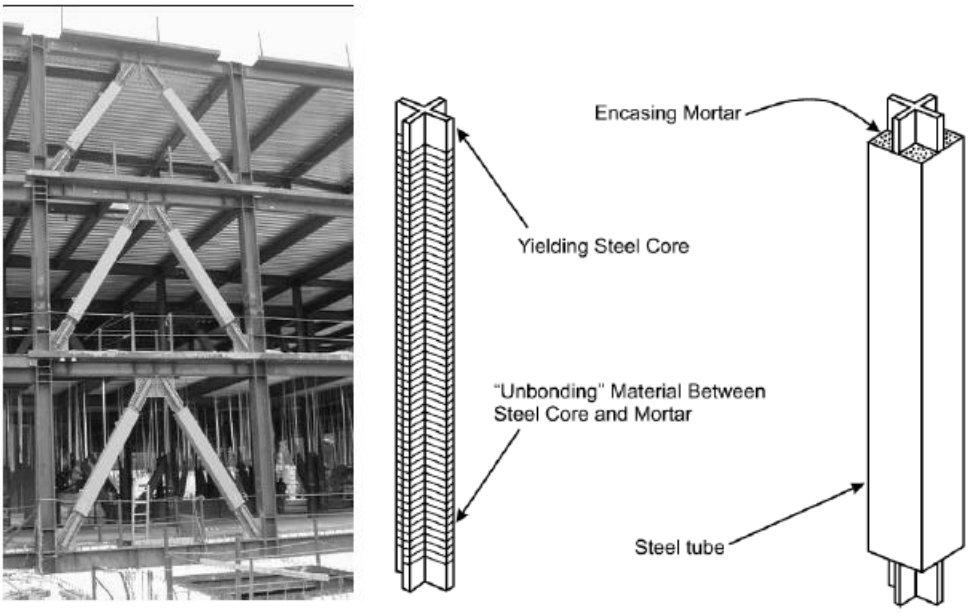

Figure 2.15 Unbonded brace

2.3.2.2 Rate-independent devices - friction dampers

Friction dampers utilize the mechanism of solid friction that develops between two solid bodies sliding relative to one another to provide the desired energy dissipation. Generally, friction devices generate rectangular hysteretic loops (see Figure 2.10), thus guaranteeing large energy dissipation; they are insensitive to environmental temperature's excursions. Among their disadvantages it is important to highlight that the interface condition could change with time; moreover the friction coefficient, during the displacement, is a function of velocity, axial force and contact surface's conditions. Consequently it is difficult to ensure a friction coefficient independent by time and by device's status. Although it has been observed that if the structure remains in the elastic field the friction coefficient variation with time does not influence significantly structural response (Bozzo and Barbat 1995). A further disadvantage is that if restoring forces are not provided, a structure equipped with friction dampers may present permanent displacements after a strong ground motion.

Experimental testing has shown that a reasonable model representing friction devices behaviour is given by the idealized Coulomb model of friction, according to which the friction force is given by the product between the axial force and the friction coefficient $P = \mu N sgn(\dot{u})$. Several types of friction dampers have been developed for the purpose of improving seismic response of structures. Among them there is the wire rope (see Figure 2.16): it is composed by cables made of different wires which are rolled together in a helicoidally shape. There are two bars at the top and at the bottom which allow the connection of the device to the structure.

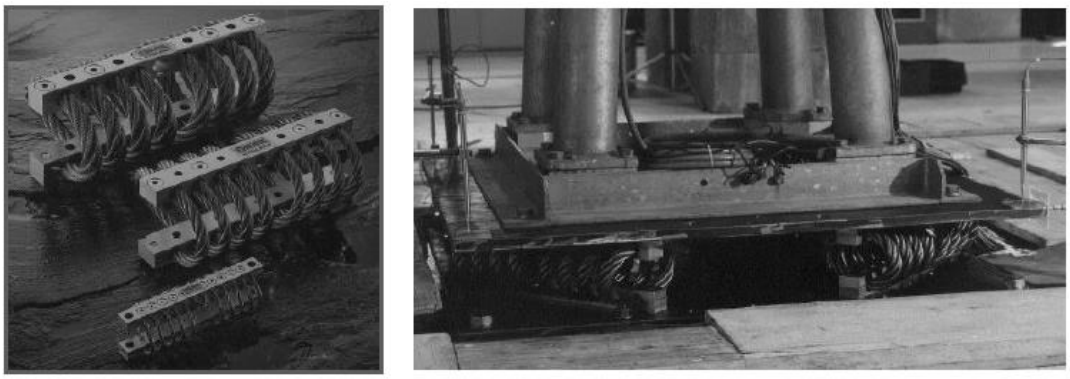

Figure 2.16 Wire rope device

The dimensions of the wire rope devices can widely vary according to the building tonnage. These devices are characterised by a significant energy dissipation capacity because when the element is deformed the ropes touch one with the other dissipating energy through friction mechanism.

Other examples of friction dampers are given by the Sumitomo system (Figure 2.17), that is generally located in brace elements, or by X-brace friction damper, that is located at the intersection point of a X-bracing member (Figure 2.18).

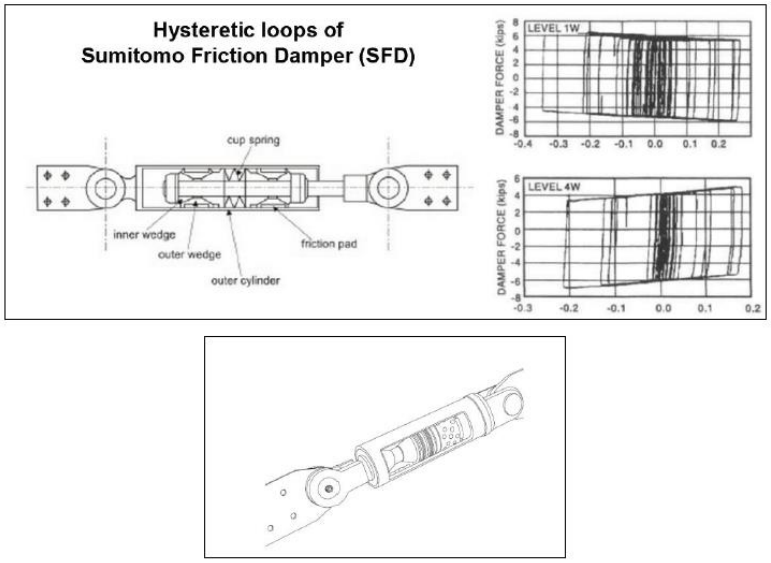

Figure 2.17 Sumitomo friction device

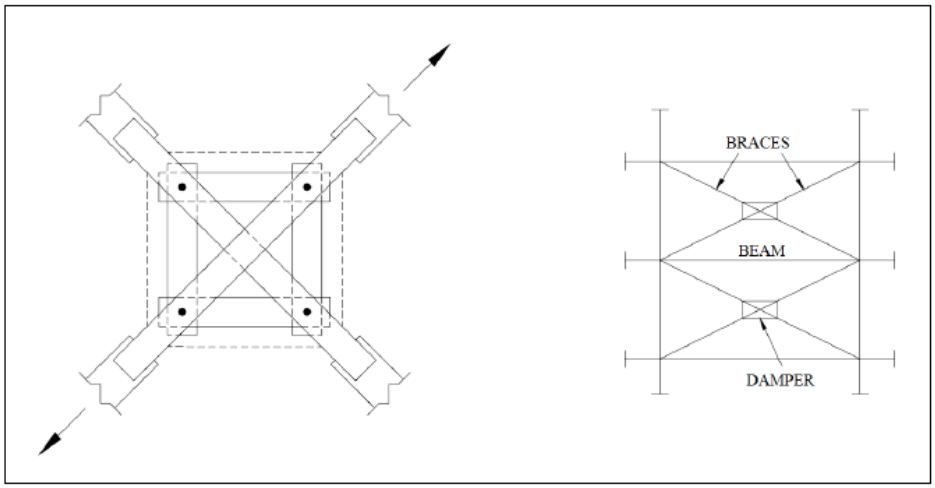

Figure 2.18 X-shape friction device

2.3.2.3 Rate-independent devices - lead extrusion device

The lead-extrusion damper is an energy absorbing device that converts mechanical energy to heat through the cyclic deformation of lead that is forced to pass in an orifice (Figure 2.19).

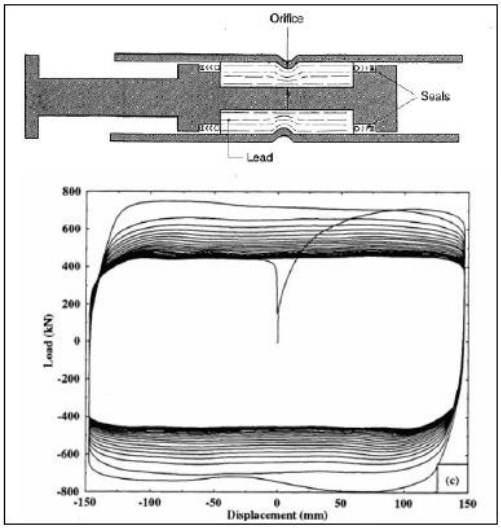

Figure 2.19 Lead extrusion device

As it is depicted in Figure 2.19 hysteretic loops generated in lead extrusion device are very stable.

2.3.2.4 Rate-dependent devices - visco-elastic dampers

Visco-elastic materials used in structural applications are usually copolymers or glassy substances that dissipate energy through shear deformation. A typical VE damper, which consists of VE layers bonded with steel plates, is shown in Figure 2.20. When mounted in a structure, shear deformation and hence energy dissipation take place when structural vibration induces relative motion between the outer steel flanges and the centre plates. The visco-elastic material takes the name from the fact that it has both an elastic and a viscous component. So the typical elliptical cycle is inclined, as it is depicted in Figure 2-33. It is important to consider that the visco-elastic material's behaviour strongly depends on the temperature: at high temperature viscous element becomes fluid thus reducing damper's energy dissipation capacities.

VE dampers are among the first energy dissipation devices employed in order to control vibration induced by the wind action in high-rise buildings, such as it was the case of World Trade Center of New York in 1969.

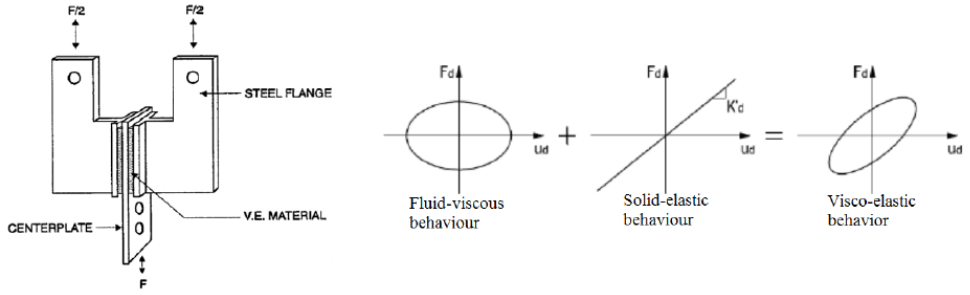

Figure 2.20 Visco-elastic damper

2.3.2.5 Rate-dependent devices - viscous fluid dampers

The most popular viscous fluid (VF) dampers consists of a hollow cylinder filled with a relatively low viscous fluid, such as silicone or similar type of oil (Figure 2.21). As the damper's piston rod and piston head are moved, fluid is forced to flow through orifices in the piston head. The resulting differential in pressure across the piston head produces large forces that resist the relative motion of the damper. The fluid flows and friction is developed between fluid particles and piston head. The friction forces dissipate energy on the base of the fluid orificing concept. Their operating is activated at low displacement.

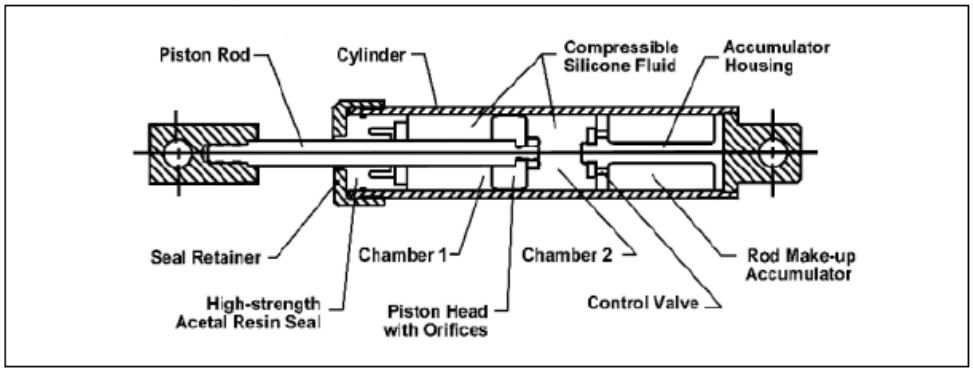

Figure 2.21 Viscous fluid damper

Viscous devices are rate-dependent and they also depend on the temperature. During seismic events the oil starts to move and its temperature increases, thus causing a decrease of its viscosity and capability of dissipating energy. Although time duration of an earthquake is very short and so the temperature increase is not significant.

Figure 2.22 Viscous fluid devices applied on real structure through braces

The viscous fluid devices developed recently include Oiles Viscous Wall Damper (Figure 2.23), advanced by Sumitomo Construction Company.

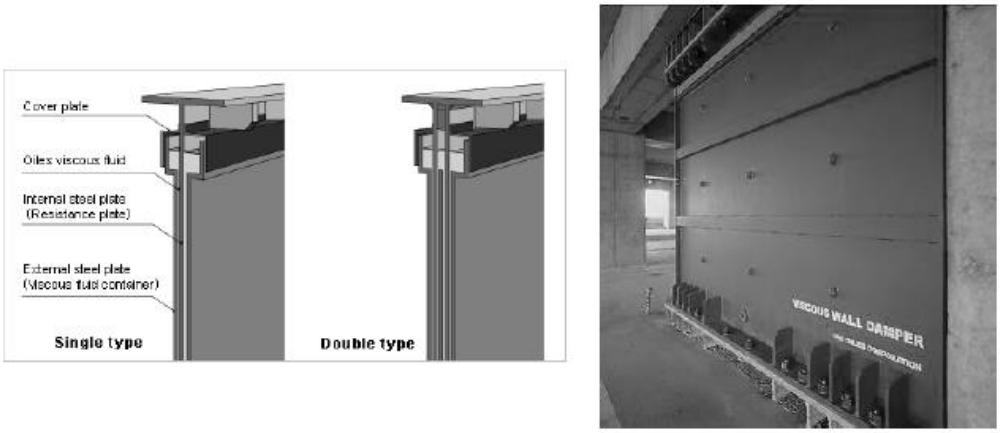

Figure 2.23 Oiles Viscous Wall Damper

It is a vibration attenuator using the shear resistance force of a highly viscous fluid. It consists of outer steel container filled with a viscous fluid and an internal shearing plate. The relative storey displacement induced by an earthquake or a strong wind produces movement of the shearing plate fixed to the upper beam relative to the viscous fluid container fixed to the lower beam. The resistance created by the movement of the shear plate in the viscous fluid effectively absorbs the vibration energy.

2.3.3 Tuned mass damper (TMD)

The tuned mass damper (TMD) consists in a single degree of freedom system added generally on the top of the structure and characterized by mass m and stiffness k tuned so that its natural frequency is equal to the fundamental frequency of the building. In this way, when the frequency of the exciting force is equal to the structural fundamental frequency, thus generating resonance effect, also the added mass, characterized by the same frequency, will oscillate in counterphase with respect to the predominant mode of vibration. Consequently it is allowed to eliminate the peak of dynamic amplification function. So if the natural frequency of the TMD is chosen to be equal to the frequency of the exciting force the main system does not oscillate because the TMD vibrates in such a way that its inertial force is at all instants of time equal and opposite to the exciting force.

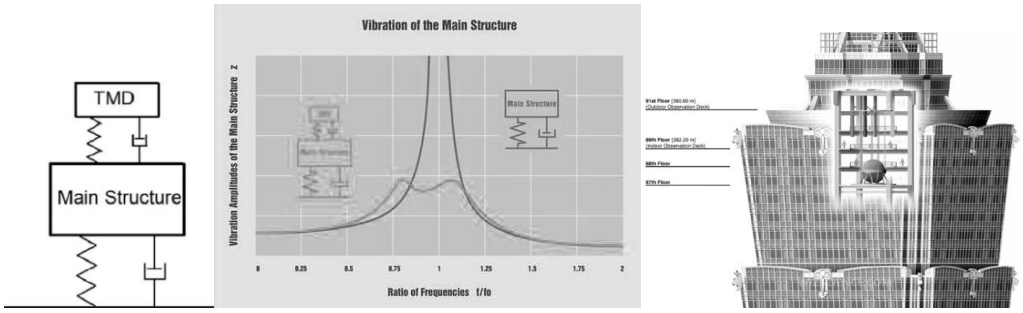

Figure 2.24 Tuned Mass Damper and Tapei 101 building

Early applications of TMDs have been directed toward mitigation of wind-induced excitations. Recently, numerical and experimental studies have been carried out to examine the effectiveness of TMDs in reducing seismic response of structures. It is noted that a passive TMD can only be tuned to a single structural frequency.

While the first-mode response of a MDOF structure with TMD can be substantially reduced, the higher mode response may in fact increase as the number of stories increases. Moreover it could happen that under the action of a strong ground motion the structure could behave plastically thus lengthening its fundamental period of vibration. For earthquake-type excitations, the response reduction is large for resonant ground motions and diminishes as the dominant frequency of the ground motion gets further away from the structure's natural frequency to

which the TMD is tuned. Another disadvantage is that the employment of the TMD requires big space in order to allow its movement.

On the other hand compared with other techniques, this vibration control offers two main advantages. One is that its impact on the structural design is minimal because it does not require a special design and the other is that it is easy to design and build. Moreover some other advantages are: a) its operation do not depend on any external power; b) it responds also to moderate levels of vibration, c) a single unit can be effective in reducing vibration induced by earthquake, wind or traffic, and d) it requires little maintenance.

2.4 Active control systems

The philosophy of active control systems is to reduce the structural response by applying forces on the structure which oppose to dynamic forces generated by the external excitation. They require significant source of external energy power and an "intelligent" acquisition and actuation electronic hardware: this feature makes them really expensive. An active structural control system has the basic configuration as shown schematically in Figure 2.25.

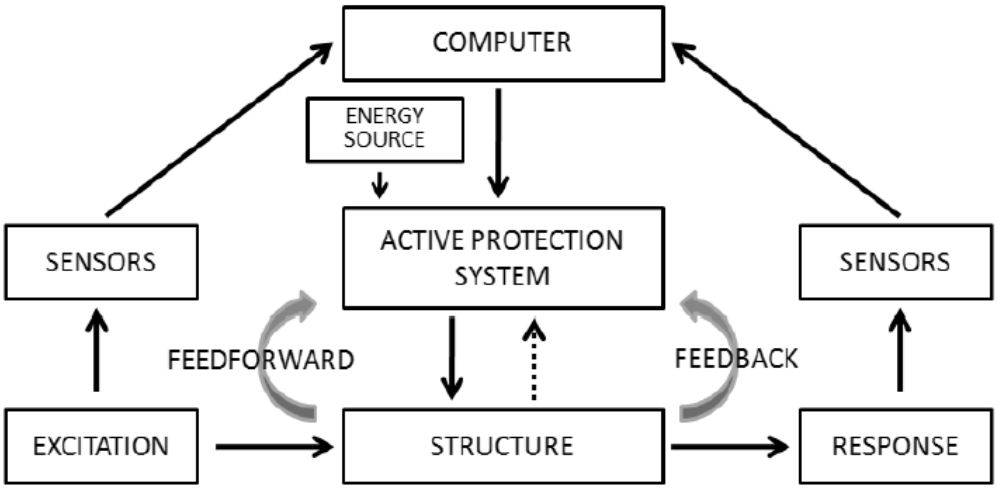

Figure 2.25 Active protection system working principle

It consists of:

1. sensors located about the structure to measure either external excitations, or structural response variables, or both;

2. devices to process the measured information and to compute necessary control forces needed, based on a given control algorithm; and
3. . actuators, usually powered by external sources, to produce the required forces.

When only the structural response variables are measured, the control configuration is referred to as feedback control since the structural response is continually monitored and this information is used to make continual corrections to the applied control forces.

A feedforward control results when the control forces are regulated only by the measured excitation, which can be achieved, for earthquake inputs, by measuring accelerations at the structural base. In the case where the information on both the response quantities and excitation are utilized for control design, the term feedback–feedforward control is used (Soong et al., 2002). The effect of feedback control is again to modify the structural properties. In comparison with passive control, however, an important difference is that the form of Γ_x is now governed by the control law chosen for a given application, which can change as a function of the excitation. Other advantages associated with active control systems can be cited:

1. enhanced effectiveness in response control; the degree of effectiveness is, by and large, only limited by the capacity of the control systems;
2. relative insensitivity to site conditions and ground motion;
3. applicability to multi-hazard mitigation situations; an active system can be used, for example, for motion control against both strong wind and earthquakes;
4. selectivity of control objectives; one may emphasize, for example, human comfort over other aspects of structural motion during noncritical times, whereas increased structural safety may be the objective during severe dynamic loading (Soong et al., 2002).

On the other hand active protection system is really expansive, as well as its maintenance. Moreover its operating would be interrupted during an earthquake if a black-out occurred.

2.5 Semi-active control systems

A semi-active control system consists in passive control system devices with variable characteristics made possible through the use of external energy power and "intelligent" acquisition and actuation electronic hardware. With difference to active control systems it requires a small amount of energy power. Its operating scheme is depicted in Figure 2.26.

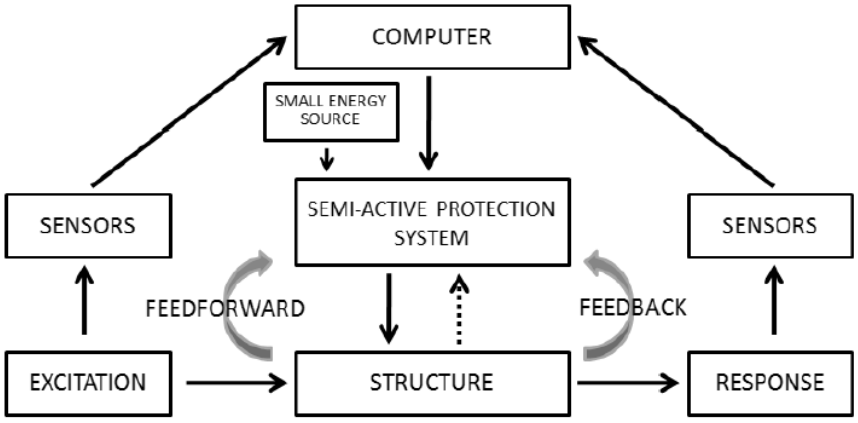

Figure 2.26 Semi-active control system working principle

Semi-active protection systems are often viewed as controllable passive devices.

Control strategies based on semi-active devices combine the best features of both passive and active control systems (Soong et al., 2002). The close attention received in this area in recent years can be attributed to the fact that semi-active control devices offer the adaptability of active control devices without requiring the associated large power sources. In fact, many can operate on battery power, which is critical during seismic events when the main power source to the structure may fail.

Extensive studies have indicated that appropriately implemented semi-active systems perform significantly better than passive devices and have the potential to achieve the majority of the performance of fully active systems, thus allowing for the possibility of effective response reduction during a wide array of dynamic loading conditions. One means of achieving a semi-active damping device is to use a controllable, electromechanical, variable-orifice valve to alter the resistance to flow of a conventional hydraulic fluid damper (Figure 2.27).

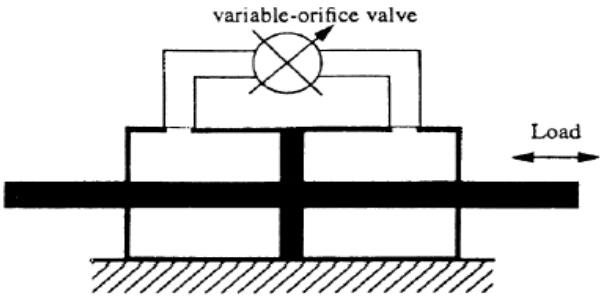

Figure 2.27 Semi-active viscous damper

2.6 Hybrid control systems

A hybrid control system consists in the combination of active and passive systems. Since a portion of the control objective is accomplished by the passive system, less active control effort, implying less power resource, is required. A side benefit of hybrid control systems, as well as semi-active ones, is that in the case of a power failure, the passive components of the control still offer some degree of protection, unlike a fully active control system. Among the hybrid control systems that have sparked interest there is the Hybrid Mass Damper (HMD). It is one the most common control device employed in full-scale civil engineering applications.

A HMD is a combination of a passive TMD and an active control actuator. The ability of this device to reduce structural responses relies mainly on the natural motion of the TMD. The forces from the control actuator are employed to increase the efficiency of the TMD and to increase its robustness to changes in the dynamic characteristics of the structure. The energy and forces required to operate a typical HMD are far less than those associated with a fully active control system of comparable performance.

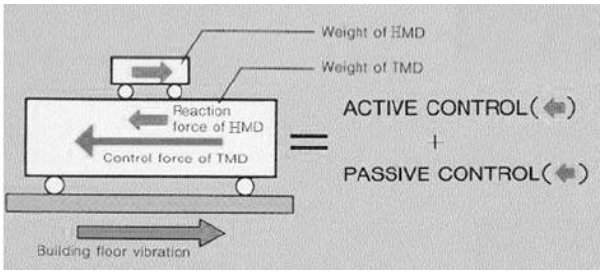

Figure 2.28 Hybrid mass damper

2.7 Bozzo Shear Link device

The Shear Link (SL) device (Figure 2.29) is an energy dissipation device suitable for the seismic protection, developed at the University of Girona (Cahís et al. 1997, Cahís et al. 1998, Bozzo et al. 1998).

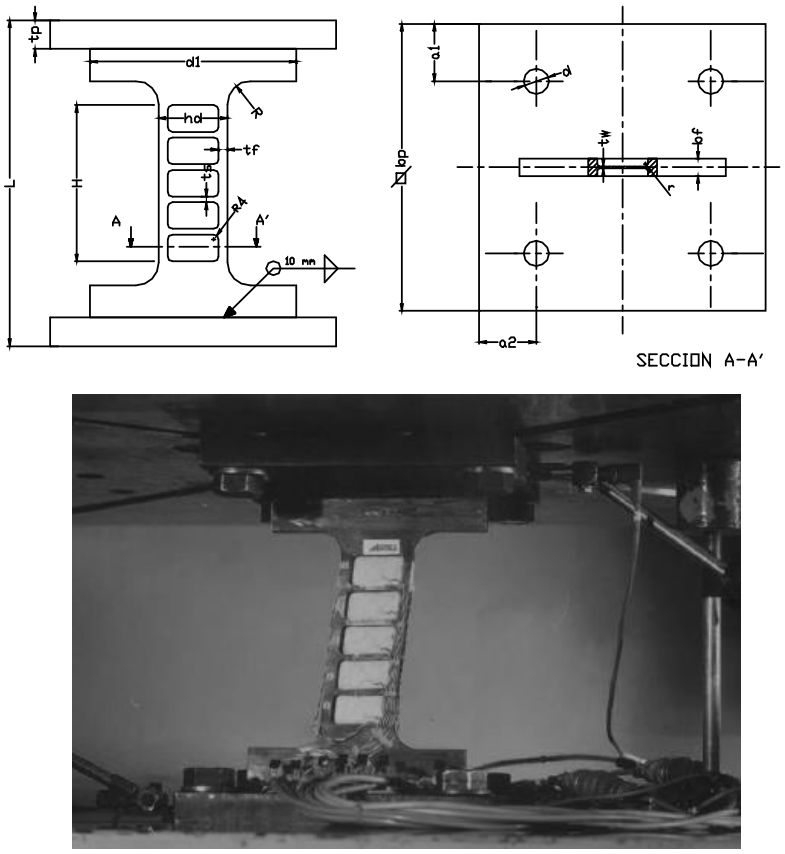

Figure 2.29 Shear link energy dissipation device

The proposed dissipator is very simple since it essentially consists in a metallic plate. The system is not based on standard shapes or specially welded ones. The main shape is obtained from a rectangular hot laminated element in structural steel, which is reduced, in some parts of it, by a milling machine. In this way, without any welded part, it is possible to obtain some "windows" of thinner thickness along the web of the device. Under shear stresses action on the web the two steel plates in the dissipator plane, placed at the top and the bottom of it, are subjected to a parallel displacement that generates strain in the device.

When in correspondence of the milled areas yielding is reached, plastic deformation in "windows" produces energy dissipation. Hysteretic curves achieved are quite stable and are characterized by a low strength reduction. The milling manufacturing process, proposed by Cahis et al. (1998), allows very thin dissipative areas, avoiding welding procedure and all the possible problems connected to it, like the brittle behaviour originated from residual stresses. Moreover, thanks to small transversal dimensions of the milled areas, uniform energy dissipation is ensured for very low values of shear stresses, since the device requires low shear forces to yield. Consequently, it has the advantage of starting to dissipate energy at very small deformations with the potential of reducing inter-storey drifts for buildings, thus providing an important benefit for non–structural elements.

For this reason the devices are usually characterized by some horizontal and vertical stiffeners between the milled areas. Thus the design of these dissipators has to consider the web buckling check, performed with the support of relations from the state-of-art.

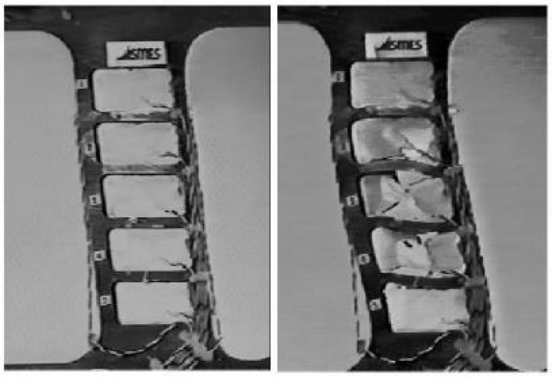

Figure 2.30 Shear and flexible working modes

So the device continues to dissipate energy also after the failure of the milled areas, even if its stiffness is quite reduced and so the hysteretic curves are larger and lower than the one characterizing the “shear mode” (Figure 2.31). Generally the energy dissipation provided by the “flexible mode” is not taken into account in the seismic design of the devices, ensuring an additional safety factor which is quite important considering all the uncertainties related to the definition of the seismic action. This second dissipation mode is very important to avoid a sudden loss of protection.

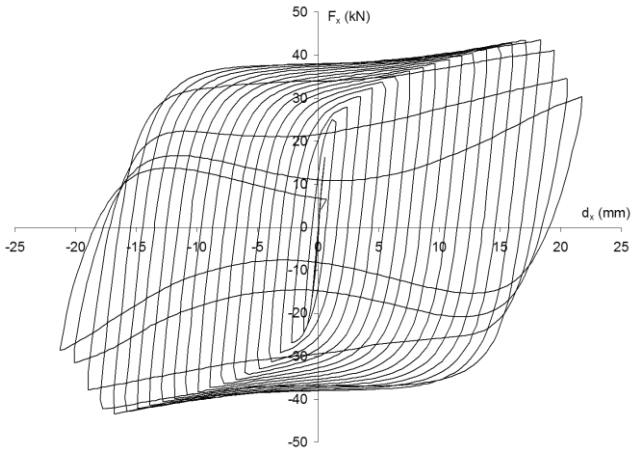

Figure 2.31 Shear link typical hysteretic curves

The connection between the structure and shear link devices is a very important feature of the design of these elements since if it is too weak and fails stresses transfer from the structure to the devices is not ensured thus making possible the structural collapse. Shear link's properties make it suitable to be used in non-standard dual systems to protect the structural and non-structural elements.

It may be used as a link between the flexible frame and a conventional steel braced system (Figure 2.32), or it may be used as link between flexible frames and masonry walls. This last configuration allows the use of wall as structural system, and at the same time prevents its damage under earthquake.

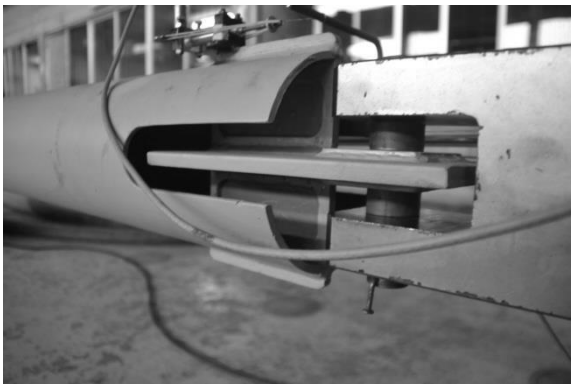

Figure 2.32 Shear link energy dissipation devices allocated in tubular braces

Shear link elements are quite small and manageable, for this reason it is possible to vary quite easily the type of connection to the structure. When the device is bolted to the structure generally it is characterized by an I-shape so that the flanges can provide a surface for the bolts.

Otherwise, if the connection is realized through welded steel plates it is not necessary to assign this type of shape.

In order to define a shear link energy dissipation device it is necessary to establish several dimensions, a part of the choice of the material, that are: the total height, the dissipative height, the width, the thicknesses, the position and dimension of the stiffeners. The variability of all these characteristics allows to obtain dissipators of quite different yielding forces, according to the different shear stresses expected in several points of the structure or at different stories. Another important feature of these devices is that the material used to manufacture them is quite cheap. Moreover it is easy to inspect and eventually replace them.

The first type of Shear Link dissipator was developed by Durgesh C. Rai (Department of Civil and Environmental Engineering, University of Michigan) and Benjamin J. Wallace (Department of Civil Engineering and Environmental Science, University of Oklahoma). Although the working principle is the same of shear links described before, it is different both in the form and the material. It consists in an I-shaped aluminum beam (Figure 2.33), characterized by some stiffeners in the web, sandwiched between the top of diagonal braces and a beam from the floor above (Figure 2.34). The lateral load on the frame is allowed to be transferred to the shear link through a load-transferring system consisting of a shear collector beam and chevron braces so as to cause shear yielding of aluminum plates.

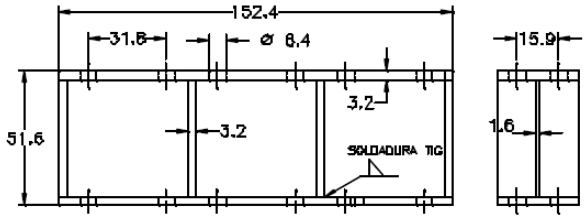

Figure 2.33 Aluminium shear link device

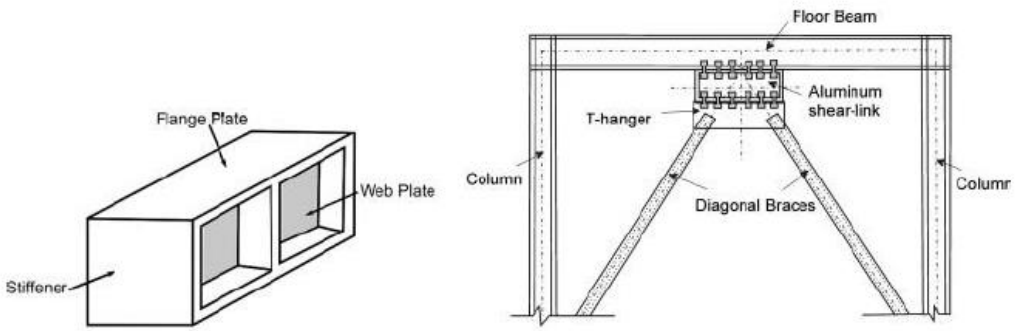

Figure 2.34 Aluminium shear link device connection

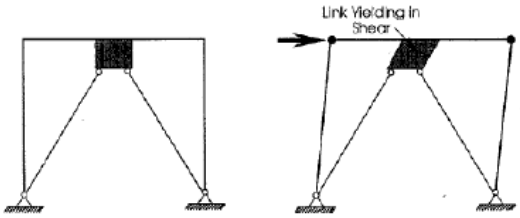

Figure 2.35 Typical collapse mechanism of shear link devices

Aluminum was chosen because of its low yield strength, enabling the use of thicker webs, thus reducing the problem of web buckling. Moreover it is characterized by a quite ductile behaviour: large inelastic deformations (about 10% strain) are reached without tearing or buckling of the member. This web shear yielding maximizes the amount of material participating in plastic deformation and gives much more uniform strain than in flexural yielding elements, resulting in a large amount of energy dissipation before the material fractures. Also, the significant strain hardening present in aluminium alloys leads to resist more lateral loads after the first yielding in a shear-link, causing additional deformations to be absorbed by links in other storeys of a multi-storeyed structure.

Thus it reduces concentration of inelastic deformation in a particular storey, which could lead to an undesirable “soft-storey” failure mechanism [Rai & Wallace 1998]. Figure 2.36 shows a typical aluminium shear-link which was subjected to a cyclic shear loading of strains up to 20% and its shear stress-shear strain hysteretic behaviour. In the dashed circles it is possible to observe, after each load reversal, some loss of loading stiffness due to bolt slippage at the connection between the specimen and the loading fixture.

Many researches and experiments have been done about the application of aluminum plates as strengthening elements of non-ductile reinforced concrete frames, enhancing their deficient lateral strength, lateral stiffness and energy-dissipation potential.

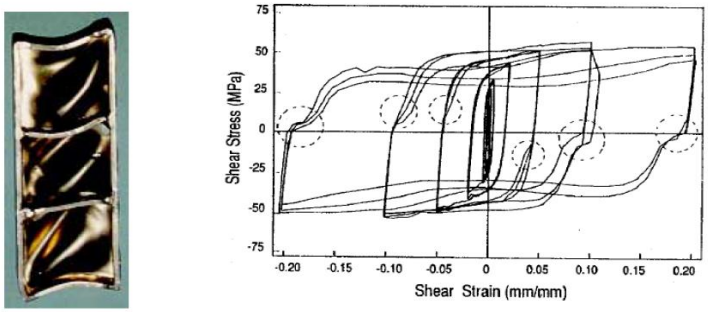

Figure 2.36 Yielded aluminium shear link and its shear stress - shear strain hysteretic behaviour

An inconvenience in adopting aluminium shear links lies in the fact that the use of dissimilar materials (aluminium shear link in contact with steel girders and steel bolts) can cause galvanic corrosion in the presence of an electrolyte, such as moisture, in the faying surface. As a result aluminium parts may act as an anode and become eroded in time. The attack can be thwarted by isolating the two materials from each other, thus preventing the formation of the "corrosion battery" and/or minimizing its effectiveness. The application of an aluminium shear link as part of a steel construction requires skilled personnel because of the difficulty in welding steel and aluminium plates.

Moreover the heat in input in welded areas removes the eventual effect of the thermal treatment that may be provided to the aluminium alloy to improve its mechanical proprieties, resulting in a distribution of strength varying along the cross section of the profile, with the minimum at the weld equal to the elastic limit of the annealed material (Rai & Wallace 1998). In order to remedy it is possible to anneal the whole specimen and to hold it at a high temperature for a certain amount of time before allowing it to cool gradually. This should relieve it from residual stresses. Another disadvantage is that friction grip bolted joints are difficult to realize with smoother aluminium surfaces, which have a low friction coefficient (order of 0,10-0,15).

Another important feature relative to steel shear link is that it can be viewed not only as an energy dissipation device, but also as a new element, to be considered part of the structure, in the field of steel seismo-resistent constructions. Very often bracing members are used as resistant elements to seismic action, but there are some limits related to their application that can be overcome by using energy dissipators such as the shear links. For example consider a simple steel frame with diagonal braces designed in order to absorb a certain horizontal force F.

Considering the compression fragility of the diagonals, sensible to the buckling failure, it will be necessary to oversize the braces, designing them in order to resist to a force αF. Thus it may be necessary to upgrade the existing foundation at the bracing locations, with the obvious consequent increase of the intervention’s cost. If at the bottom of each diagonal a shear link, designed so that it yields in correspondence of the force F, is provided, several benefits will be achieved:

- it is no more necessary to oversize diagonals since the horizontal force is absorbed by shear links;
- shear links hysteretic behaviour provides energy dissipation;

- in case of a strong seismic action the replacement of the deformed shear links is quite easier and cheaper than the eventual replacement of the bracings, since they are easily integrated with steel-framed buildings by bolting or welding connections.

In conclusion, it is possible to state that differently from other types of energy dissipators, which don't allow reductions of the seismic force but just work providing additional damping to the structure, steel shear links can be considered plastic joints where concentrate the non linear behaviour, thus reducing the seismic action, exactly reflecting the concept of the seismo-resistant design.

3 EXPERIMENTAL INVESTIGATION ON BOZZO SHEAR LINK

In this chapter it will be analysed the experimental behaviour of Bozzo shear link, based on the steel deformation due to shear force.

In case of structures equipped with passive energy dissipation devices, structural design codes generally require the fulfilment of experimental tests on devices and basic materials, in order to assess their damping, strength and stiffness properties. Since dissipated energy provided by yielding devices is represented by the area enclosed in hysteretic loops associated to nonlinear behaviour, it is important to verify parameters defining the hysteresis shape, that are the yielding force F_y, its corresponding displacement d_y and the post-yielding stiffness k_2. Moreover it is important to test the basic material constituting the device. Thus a tensile testing on the material is required. On the other hand energy dissipation devices are tested as well in order to correlate force-displacement properties to values used in the mathematical model employed for the structural design. Moreover testing devices allows to demonstrate the robustness of the individual element to extreme seismic excitation.

3.1 Description of Bozzo Shear Link

The proposed Shear Link dissipator is based on the eccentric braces structural system since the overall shape is a well stiffened wide flange section. However, the system is not based on standard shapes or specially welded ones. Instead the device is milled from a plane standard shape. This fabrication process proposed by Cahis (1998) allows very thin dissipative areas

without welding. In the other hand, as in eccentric braces, dissipation of energy is uniform in the whole section, and it is very stable provided web buckling is avoided.

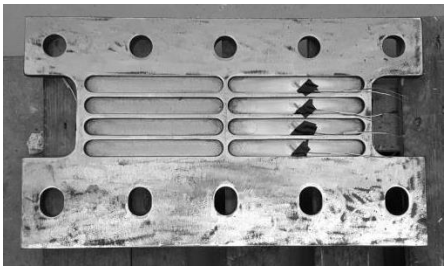

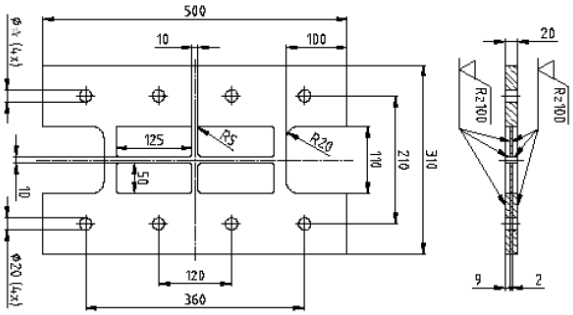

Figure 3.1 Shear Link specimen

This devices is inserted in a structure between chevron braces and an upper beam through a bolted connection that allows an easy substitution of a damaged device after a strong earthquake. As it is shown in Figure 3.1, the connection between the upper beam and the device is realized through slotted holes because the aim is that no axial force is transmitted, but just shear and bending moment. The length of these holes is deigned to be greater than the deflection of the upper beam induced by gravity loads.

The devices are named as SLB X-Y to indicate the geometry property:

- X is the width of the web of dissipator (cm)
- Y is the thickness of the windows (mm)

So in this case there are:

SLB 30_3

SLB 40_3

SLB 40_5

SLB 50_3

SLB 50_5

All have in common two vertical stiffeners (10 mm width) at both lateral ends, the width of central stiffener is 6 mm, the web thickens is 19 mm.

All the dimensions are shown in the following figure:

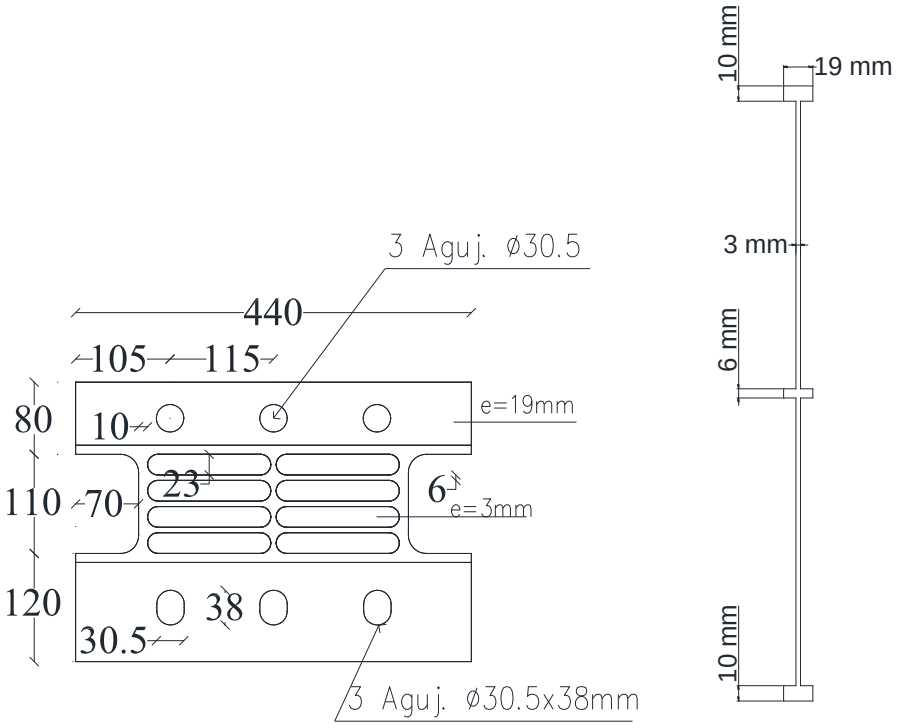

Figure 3.2 Geometry of SLB 30_3

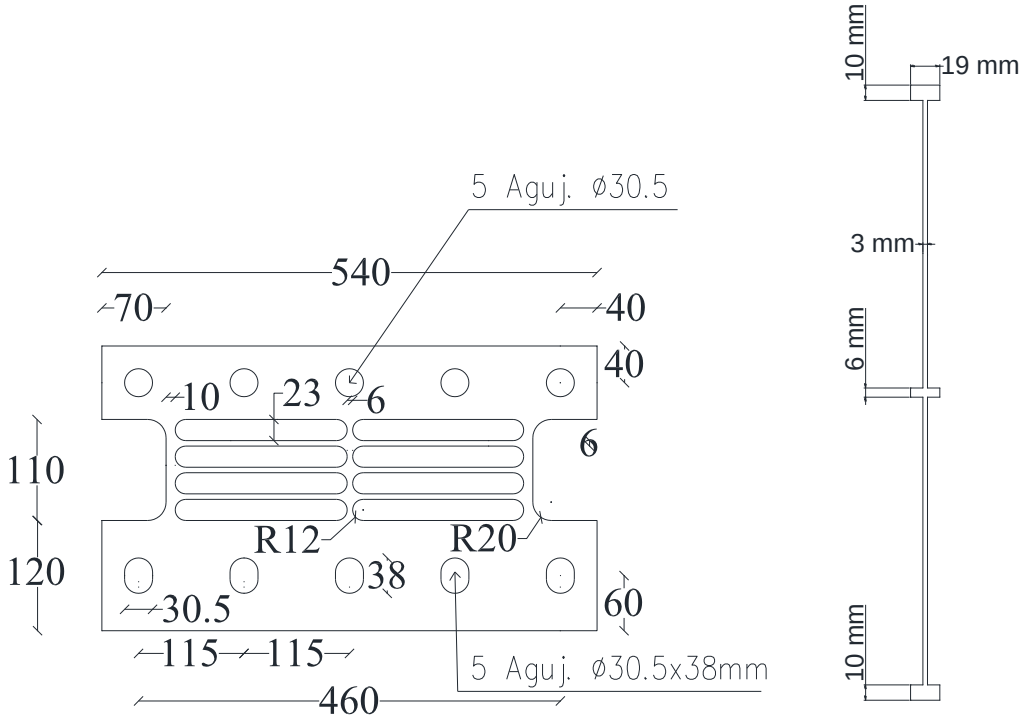

Figure 3.3 Geometry of SLB40_3

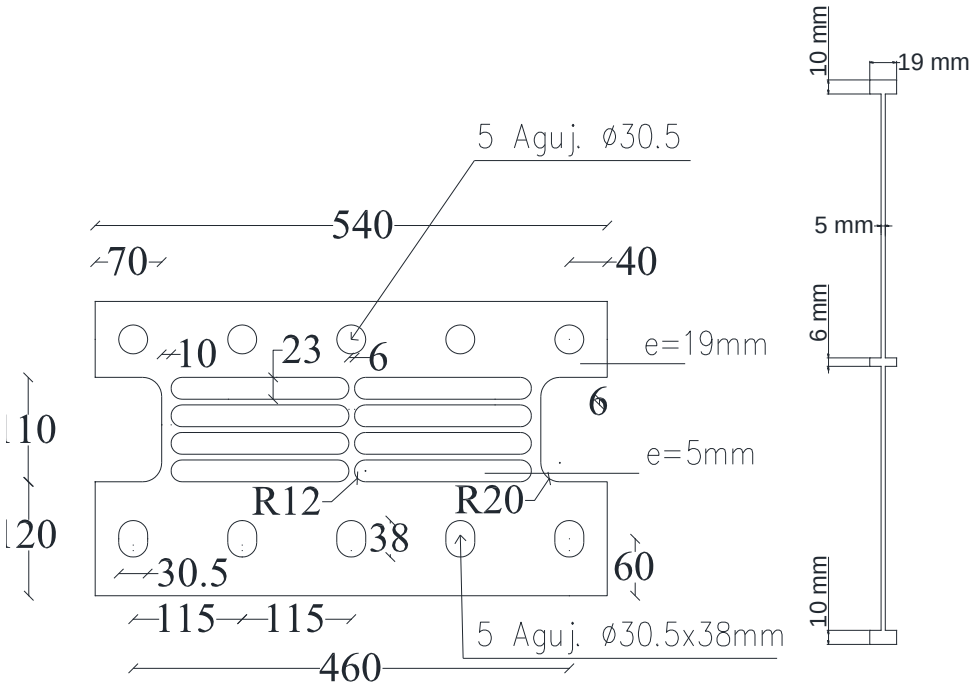

Figure 3.4 Geometry of SLB 40_5

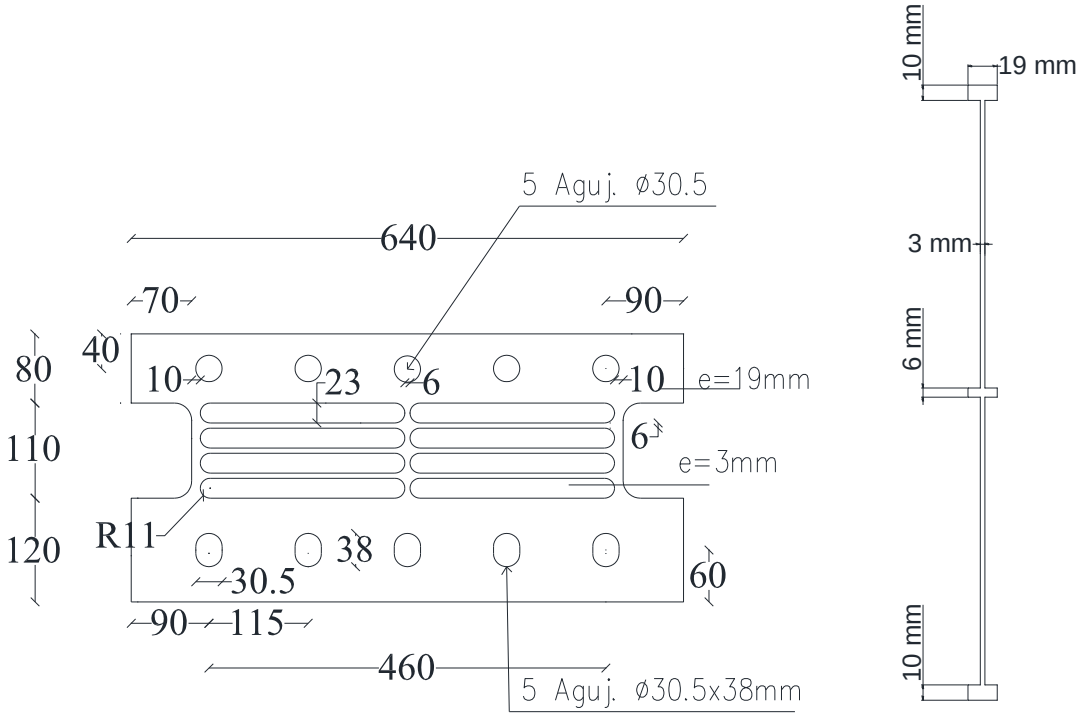

Figure 3.5 Geometry of SLB 50_3

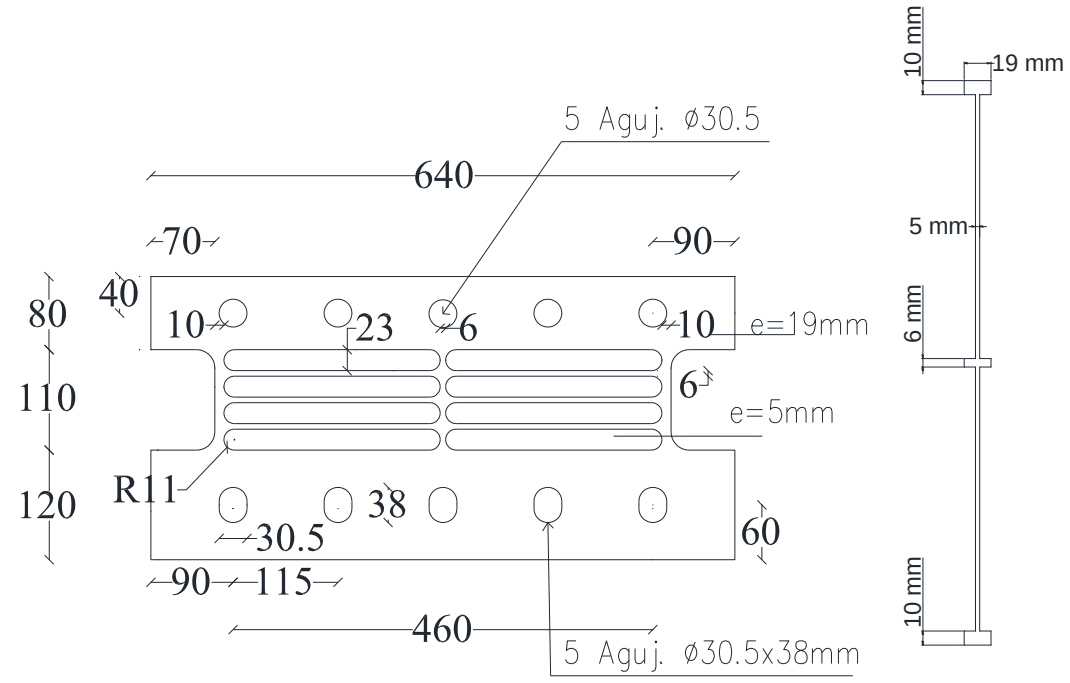

Figure 3.6 Geometry of SLB 50_5

For each device there are realized two specimens, which have been tested.

3.2 Material

The material used for Bozzo Shear Link is Steel ASTM A36. In the Table 3.1 there are its mechanical properties.

Mechanical Properties	Metric
Tensile Strength, Ultimate	400 - 550 MPa
Tensile Strength, Yield	250 MPa
Elongation at Break (in 200 mm)	20.0 %
Elongation at Break (in 50 mm)	23.0 %
Modulus of Elasticity	200 GPa
Bulk Modulus (typical for steel)	140 GPa
Poissons Ratio	0.260
Shear Modulus	79.3 GPa

Table 3.1 Mechanical properties of ASTM A36

The tensile test on the material is performed at the laboratory of the University “Federico II” of Naples.

Figure 3.7 Tensile universal testing machine MTS810

The tensile test was lead at a velocity of 0.05mm/sec; results are reported in the Figure 3.9. In the Figure 3.10 the sample before and after testing is shown.

CHARACTERISTICS	Test specimen
	Structural steel plate
Cross section WxT [mm]	40x19
Calibrated length G [mm]	50
Cross section Area [mm^2]	760
Yielding force [kN]	259,52
Maximum force [kN]	340,34
Yielding strenght [MPa]	341,47
Maximum strenght [Mpa]	447,82

Table 3.2 tension test: characteristics and results

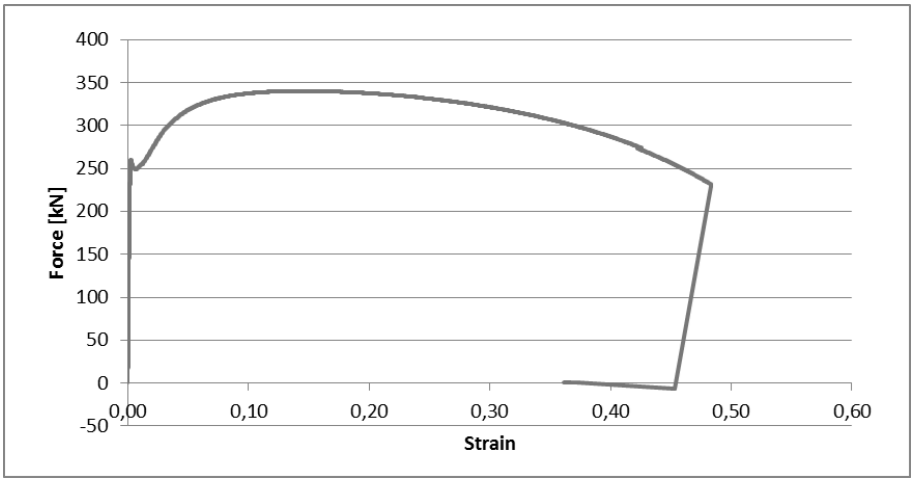

Figure 3.8 Tension test: force-displacement curve

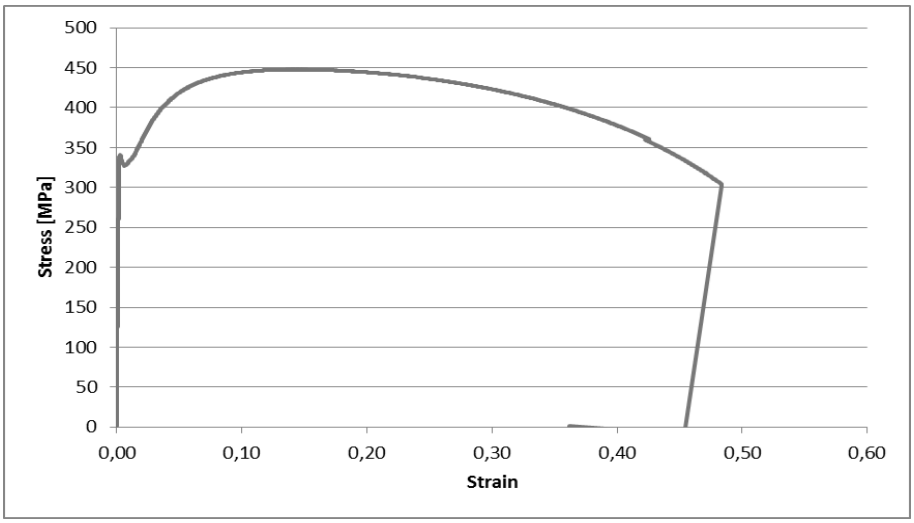

Figure 3.9 Tension test: strength-displacement curve

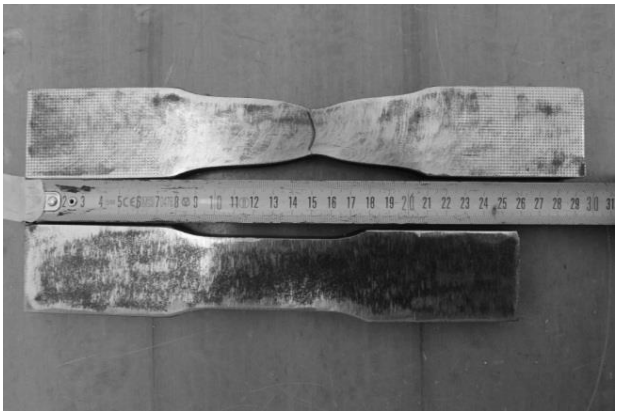

Figure 3.10 Standard steel sample before and after testing

From the Figure 3.9 it is possible to note that at the beginning the relation stress-strain is linear, it is the elastic range. When the stress reaches the value of yielding stress, $\sigma_y = 341\ MPa$, the behaviour is not elastic and plastic deformations occur. The stress increases with the increase of the deformation, when it reaches the maximum value, $\sigma_{Max} = 447\ MPa$, in the middle cross section of specimen the necking phenomenon starts, it causes the tension failure.

3.3 Description of set up

The experimental campaign of Bozzo Shear Link has been lead at the laboratory of Dist (Dipartimento di Strutture per l'Ingegneria e l'Architettura), University of Naples Federico II.

The machine, which is used to perform the tests, is the ITALSIGMA universal machine, Figure 3.11.

Figure 3.11 ITALSIGA Universal machine

The Italsigma machine allows testing specimens, with height between 0.5 and 4.0 meters, both in compression and tension; cyclic tests are also allowed. The machine is characterized by a rigid steel basement (1,0x4,0 m^2), with a T-shaped runners in order to assembling the test equipment and the specimens restrains. The machine has a steel frame characterized by four columns placed on the corner of a rectangular area fixed on the basement and connected by a horizontal mobile frame. Such horizontal frame runs along the vertical steel columns and it is provided by an actuator for both displacement control tests (maximum displacement ± 75 mm) and force control tests (maximum compressive load, 3000kN, maximum tensile load 2400 kN).

The hydraulic actuator is controlled from electrohydraulic servo valves connected to electrical control panel. It's possible to control the tests with a personal computer.

The set-up has been designed in order to apply the shear force directly at the specimen, in this way it is possible to perform the cyclic tests and the monotonic test. The reference code are Italian code NTC2008, Circolare n˚617 02/02/2009 and Eurocode EC3.

It is composed by metallic element, the materials are:

- Hardened and tempered steel: $f_y = 700\ MPa; f_t = 900\ MPa$
- Steel S355: $f_y = 355\ MPa; f_t = 510\ MPa$
- Steel AS (I.Nuzzo, 2016)

The static pattern of the set-up can be represented as in the Figure 3.12.

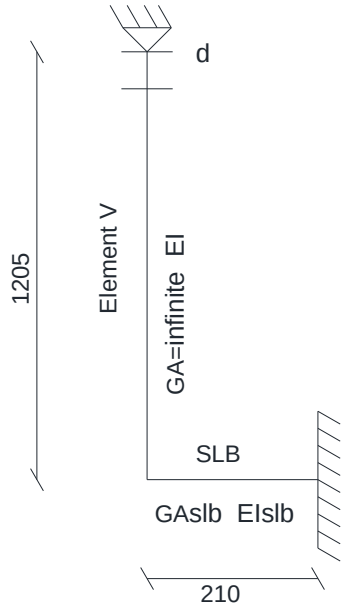

Figure 3.12 Static pattern of set up

The vertical element is high 1,205 m, in particular from cylindrical hinge to centre of bolting of the device. The horizontal element is the testing device. This static pattern is subjected to vertical imposed displacement at the top.

In order to design the set-up, two limit conditions are considered: vertical element V has flexural stiffness infinite or null. These conditions represent the two conditions of tests performed: the first condition is that the bolts, in correspondence of slotted holes, are perfectly tightened, said fixed-fixed, the second one is that the bolts are not tight said no fixed-fixed. Because the presence of slotted holes in the device, vertical sliding is allowed.

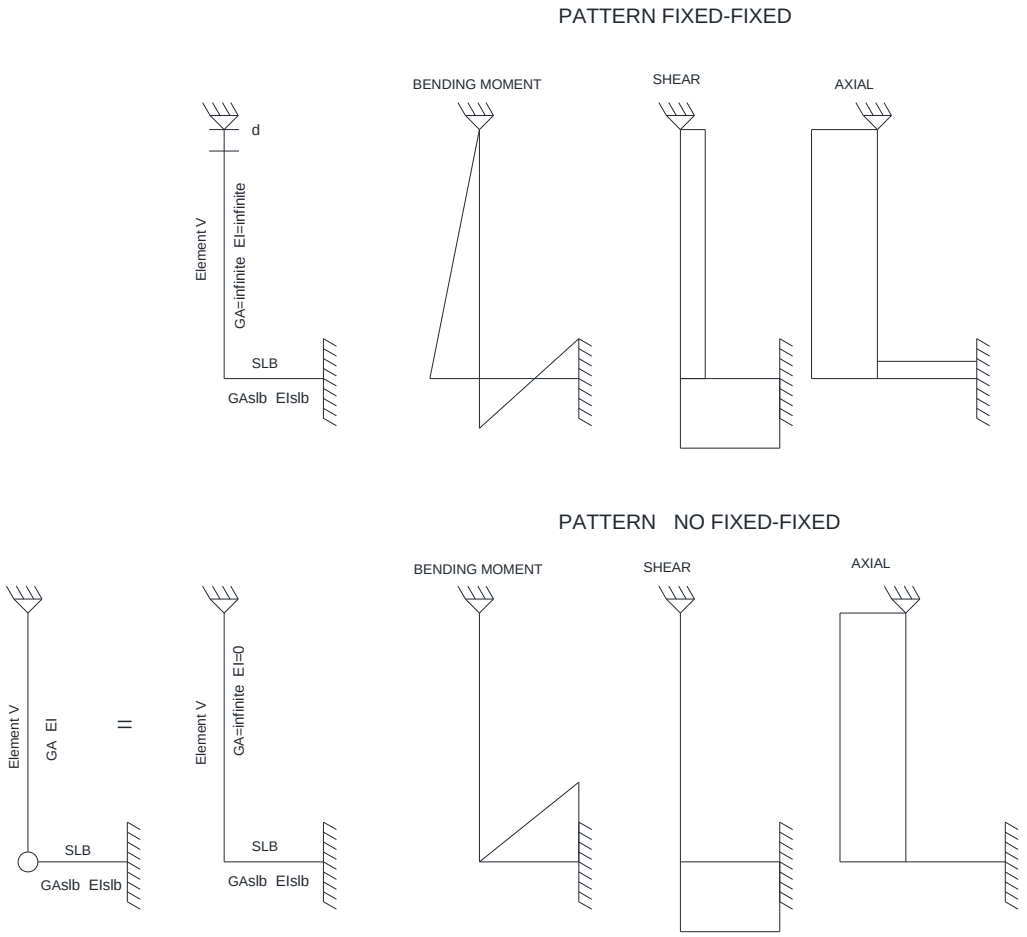

Figure 3.13 Pattern of set-up

The Figure 3.13 illustrates the solicitations due to the different patterns. In the first case, because of the tightened bolts, the connection between the vertical element and the horizontal element is continuous. The specimen is fixed-fixed, so the bending moment diagram is linear. For the continuity of the connection, the bending moment is transmitted along the vertical element. In the vertical element the bending moment is linear and annuls at the top of the setup because it is realized a cylindrical hinge. Moreover the shear is constant in the vertical element. The axial is constant in both elements. All these solicitations are transmitted to the machine, which has not a great resistance with respect to the shear force.

The second case represents the fixed-nofixed condition, it is characterized by the connection, between the vertical element and horizontal element, no continuous, in fact it is schematic as a hinge. Consequently the specimen can be represented as a cantilever, so the bending moment

diagram is null in the connection. Along the vertical element the bending moment is null and the shear force is null too.

In order to reduce the value of the shear transmitted to the machine in the fixed-fixed condition, it has been chosen an high height of vertical element V, as shown in the equation (3.1).

$$V = M \times height \tag{3.1}$$

It is constituted by an element HEM300 (element B), so it has infinite shear stiffness, in order to avoid rotation.

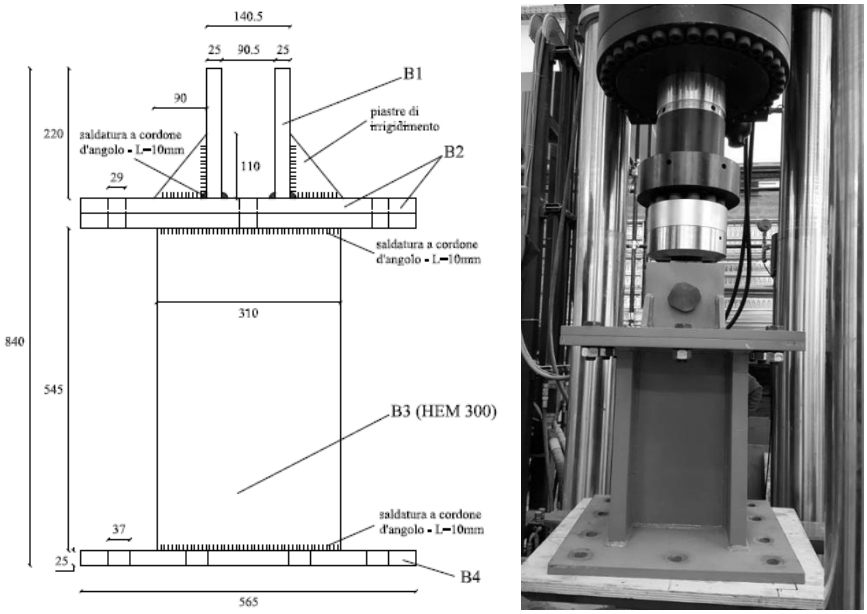

Figure 3.14 Pattern and image of element B

The element B is connected to the elements C, they constitute the vertical element shown previously. Between the elements C the shear link specimen is inserted. As it is evident from Figure 3.15, elements C are characterized by slotted holes that allow the connection to the upper part of the shear link that is placed in a rotated position, as depicted in Figure 3.15.

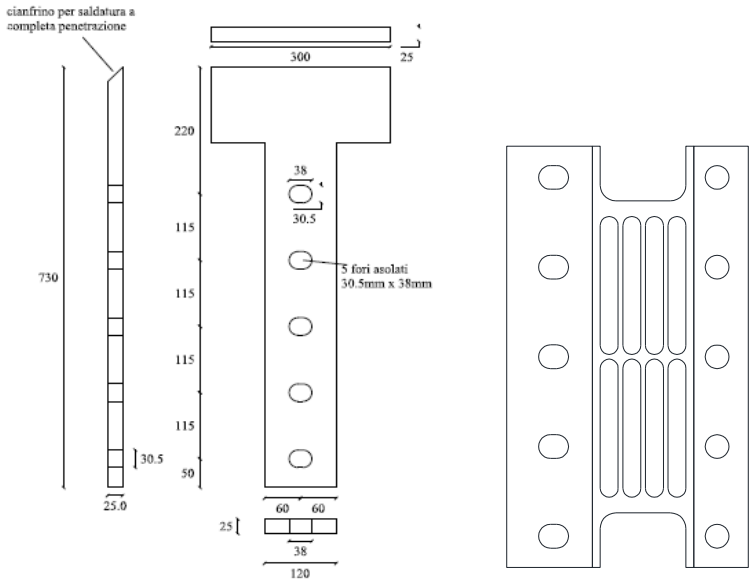

Figure 3.15 Element C of set-up and Bozzo's shear link specimen

There are also two equal elements characterized by C shape, due to three welded plates, which allow perfect vertical displacement. They are bolted to the base.

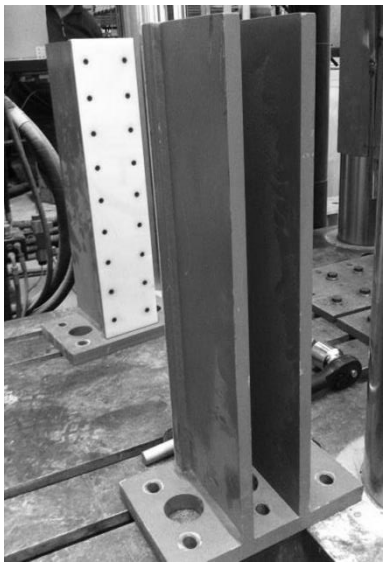

Figure 3.16 Elements with C-shape

On the other side of the Bozzo shear link there are two plates bolted to the specimen, elements D. Then, differently to the left side of the set-up, they are welded to an orthogonal plate that, in its turn, is bolted to the machine. These elements reproduce the fixed restrain.

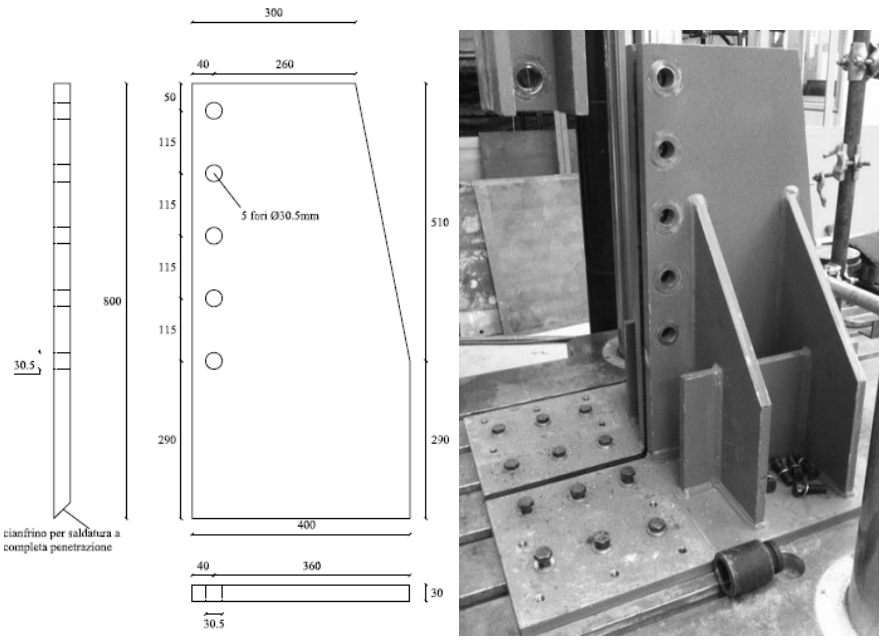

Figure 3.17 Element D

Figure 3.18 Element D and complete set up

3.4 Measuring equipment used for the tests

For the experimental test, load cell, strain gauges and LVDT are used.

The load cell is located at the top of the set up, it provides the value of the force in the actuator. Its properties are shown in the following table:

Device	*Measurement*	*Company*	*Model*	*Range*	*u.m.*	*Max voltage [V]*	*Sensitivity [mV/V]*	*Sensitivity*	*u.m.*
Load cell	Force of the actuator	PCB	TC8.212.R4	1000	kN	15	2	0,13	kN

Table 3.3 Properties of load cell

Figure 3.19 Detail load cell

The LVDT are used because to measure relative displacements in the device. In addition to this, since the set-up is not perfectly rigid, there could be relative displacements and relative rotations due to flexibility of restraints. By using LVDTs it is possible to correct the results of the experimental test.

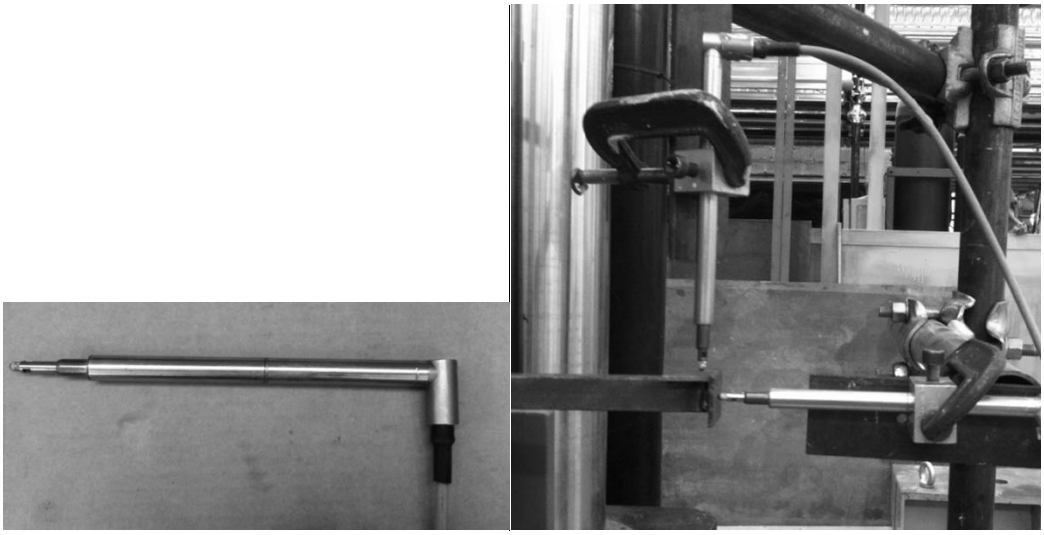

Figure 3.20 LVDT: vertical and horizontal

The following figure represents a simple pattern of horizontal and vertical LVDT:

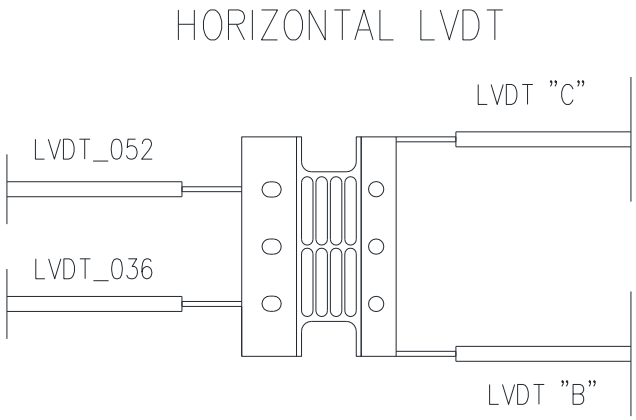

Figure 3.21 Horizontal LVDT

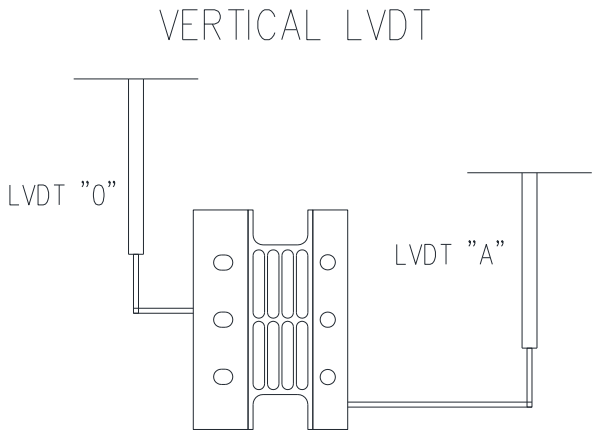

Figure 3.22 Vertical LVDT

The properties are described in the following table:

LVDT	Direction	Range [mm]	*Max voltage*	*Sensitivity*	*Sensitivity*
0	vertical	±50	2,5 V	80 mV/V	3,2 mm
A	vertical	±10			
B	horizontal	±10			
C	horizontal	±10			
36	horizontal	±10			
52	horizontal	±10			

Table 3.4 Properties of LVDT

The vertical LVDT are located at the left and right side of the specimen in order to read its relative displacements. The horizontal LVDT are located in order to read relative rotations.

Furthermore the devices are fitted with strain gauges, two are at 90˚ to measure the axial deformations (5 and 6), and others four are at 45˚ to measure shear deformations (1, 2, 3, and 4). They are located as in Figure 3.23.

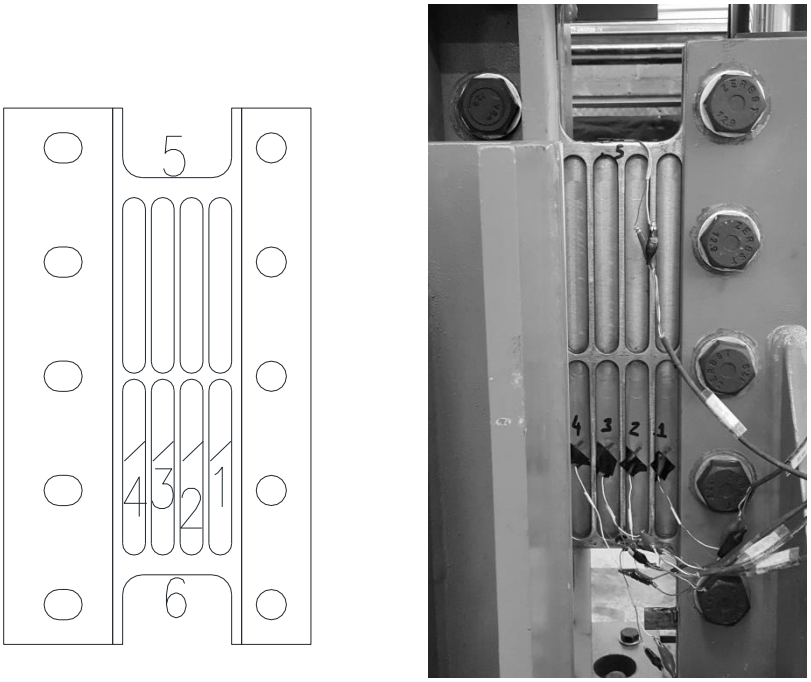

Figure 3.23 Pattern of strain gauges

3.5 Boundary conditions and loading cycles

Two kind of boundary condition are performed: fixed-fixed and fixed-nofixed.

The right side of device is bolted to the element D with very high values of tightening torque. This is necessary to reproduce the condition of fixed support. The left side is bolted in the same manner for the condition “fixed-fixed”, so there aren’t sliding between the specimen and the set up.

In the condition “fixed-nofixed”, the left side is bolted without tightening torque, in this way the sliding is allowed.

The two boundary condition can be represented as shown in the Figure 3.24.

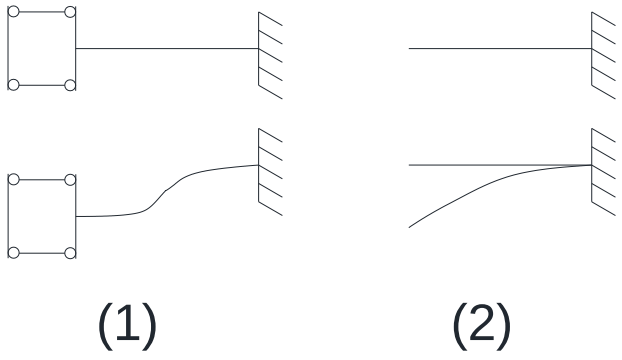

Figure 3.24 Fixed-Fixed (1) and Fixed-NoFixed (2)

All tests are static-tests because the load is applied very slowly.

The load history of cyclic test is shown in the following figure:

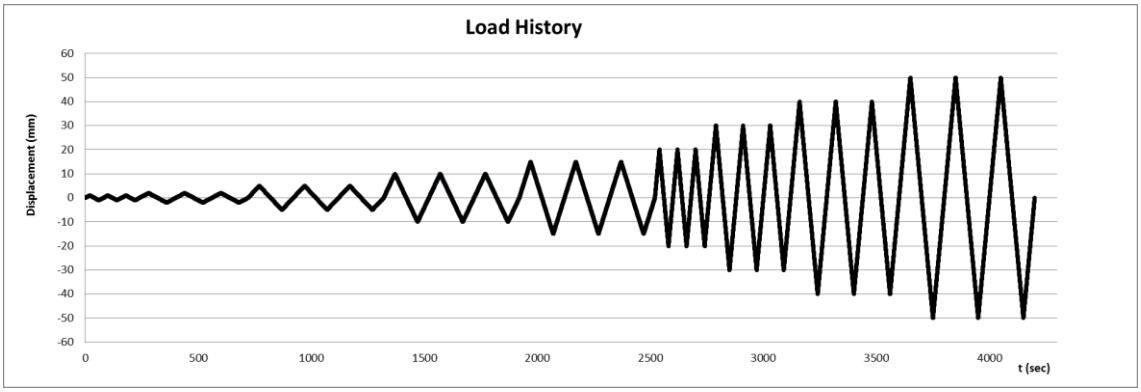

Figure 3.25 Load history for cyclic test

			duration	duration	duration	progressive	progressive
n° cycles	amplitude (mm)	velocity (mm/s)	(s)	(s)	(min)	(s)	(min)
3	1	0,05	80	240	4	240	4
3	2	0,05	160	480	8	720	12
3	5	0,1	200	600	10	1320	22
3	10	0,2	200	600	10	1920	32
3	15	0,3	200	600	10	2520	42
3	20	1	80	240	4	2760	46
3	30	1	120	360	6	3120	52
3	40	1	160	480	8	3600	60
3	50	1	200	600	10	4200	70

Table 3.5 Description of load history

For the monotonic test the load is applied with velocity of 0,05 mm/s, as shows in the following graph:

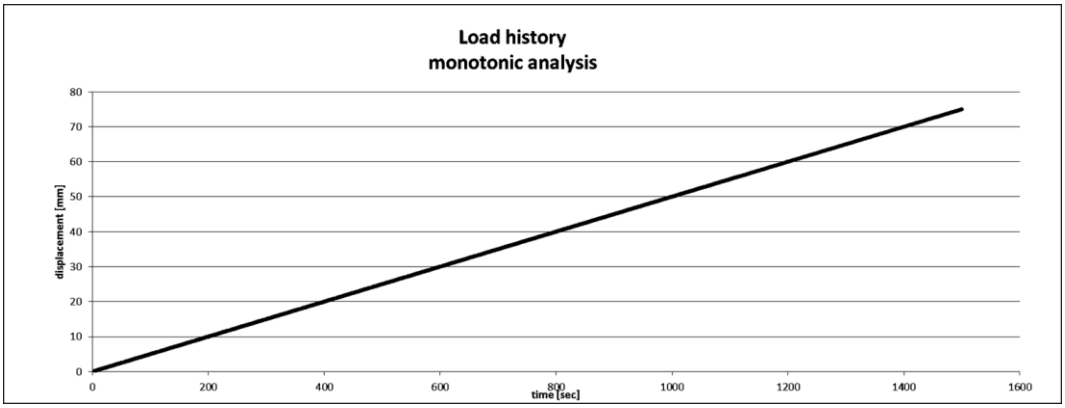

Figure 3.26 Load history for monotonic test

The following table describes the load condition and the tightening configuration performed:

Sample		Test	Tightening configuration
30_3	1	Cyclic	FF
30_3	2	Cyclic	FNF
40_3	1	Cyclic	FF
40_3	2	Monotonic	FF
40_5	1	Cyclic	FNF
40_5	2	Monotonic	FNF
50_3	1	Cyclic	FF
50_3	2	Cyclic	FNF
50_5	1	Monotonic	FNF
50_5	2	Cyclic	FNF

Table 3.6 Load condition and tightening configuration

3.6 Analysis of experimental behaviour of Bozzo Shear Link

In the following subparagraphs the experimental results are analysed in order to characterize the real behaviour of Bozzo Shear Link. It is also explained the mathematical procedure used to correct the experimental responses in order to obtain exact results.

Investigating the hysteretic behaviour it is possible to make considerations not only on the design parameters as yielding force, elastic stiffness, maximum force, dissipated energy but also on the plastic behaviour.

An accurate study of experimental behaviour permits to define an appropriate plasticity model which is used to calibrate the numerical model.

3.6.1 Displacements and rotations of SLB device

The LVDT positioning allows to read the displacements and the rotations of the devices.

It has been observed that during the first test, the right side is not perfectly fixed, but low displacements occurred. For this reason, the following tests were equipped with vertical LVDT A and horizontal LVDT B and C, located at right side, so the horizontal and vertical displacements at right are detected. In this way it is possible to obtain the relative displacement and relative rotation of the device, which are given by the difference between the displacement/rotation at left side and right side of the dissipator.

It assumes that the horizontal displacement, in x direction, is named u and the vertical displacement, in y direction, is named v. The rotation around the x axis is named ϕ. The convention of positive sign is shown in the following figure:

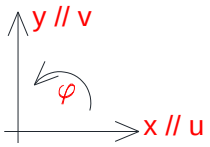

Figure 3.27 Convention of positive sign

The values of displacement and rotation, which are analysed, refer to the central point at the left and right side of the device, which are named M_L and M_R. However the displacements detected refer to points which are not located directly on the device. Because of this the displacement of points M_L and M_R are computed considering the effect of eccentricity of the LVDT.

The Figure 3.28 shows the position of LVDT and the measurement points.

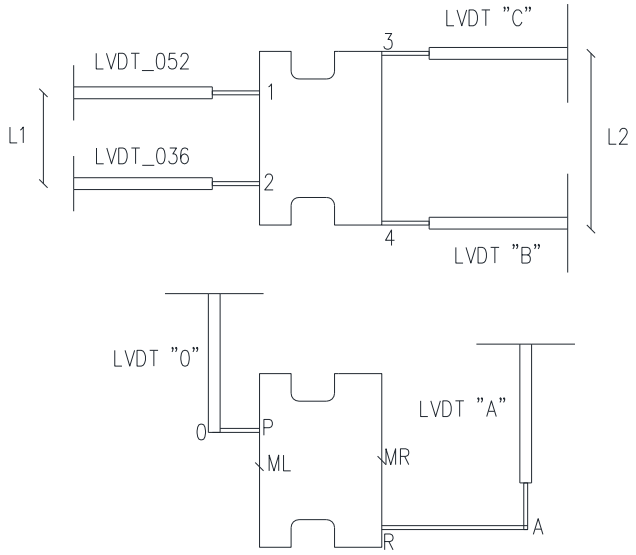

Figure 3.28 Pattern of LVDT and measurement points

Below it is illustrated the mathematical steps needed to evaluated the displacement V_{M_L} , V_{M_R} , ϕ_L and ϕ_R (the last are rotation at left and rotation at right side).

The displacement of point 0 and of its projection, point P, are obtained:

$$V_0 = -V_{LVDT0}$$
$$V_p = V_0 + \phi_L \, \overline{OP} \qquad \textbf{(3.2)}$$

Where ϕ_L is given by:

$$\phi_L = \frac{V_2 - V_1}{L_1} \qquad \textbf{(3.3)}$$

The vertical displacement of M_L is obtained:

$$V_{M_L} = V_p - (\overline{P\ M_L})\ (1 - \cos\phi_L) \qquad \textbf{(3.4)}$$

In order to evaluateV_{M_R}, there are considered:

$$V_A = -V_{LVDTA}$$
$$V_R = V_A + \phi_R \, \overline{AR} \qquad \textbf{(3.5)}$$

The vertical displacement of M_R is obtained:

$$V_{M_R} = V_R - (\overline{R\ M_R})\ (1 - \cos\phi_R) \quad \textbf{(3.6)}$$

Where ϕ_R is given by:

$$\phi_R = \frac{V_3 - V_4}{L_2} \quad \textbf{(3.7)}$$

In the end, the relative displacement and relative rotation are calculated as:

$$\mathrm{V_{relative}} = \mathrm{V_{M_L}} - \mathrm{V_{M_R}} \quad \textbf{(3.8)}$$
$$\mathrm{\phi_{relative}} = \mathrm{\phi_R} - \mathrm{\phi_L}$$

Taking in account these considerations, the experimental results are corrected, so relative vertical displacement and relative rotation are evaluated.

The experimental results for each device are presented and commented in the following subparagraph.

3.6.1.1 SLB 30_3

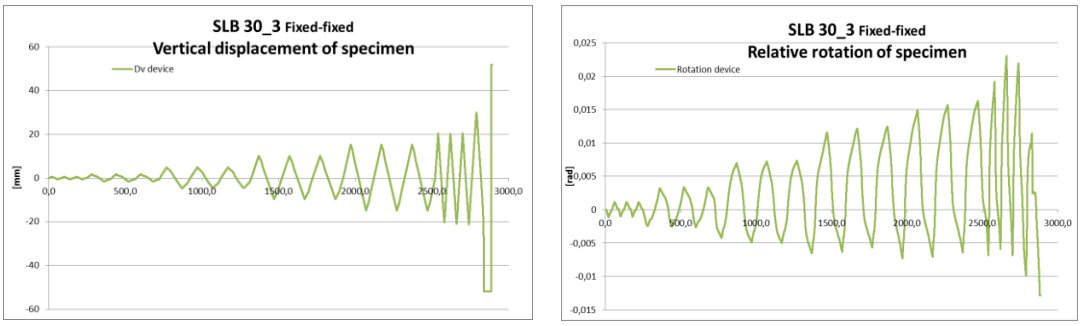

Graph 3-1 vertical displacement and rotation SLB 30_3_Fixed-fixed

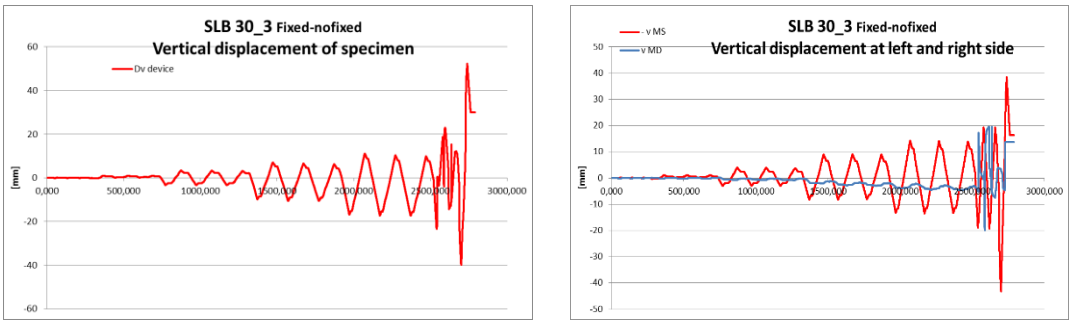

Graph 3-2 vertical displacement SLB 30_3_Fixed-nofixed

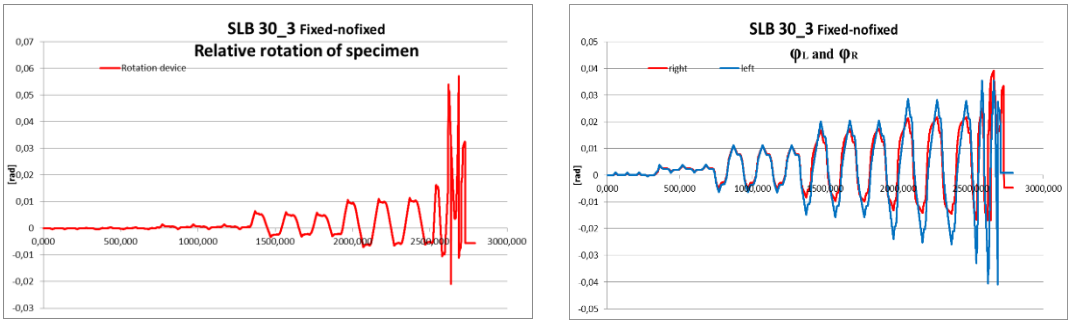

Graph 3-3 Rotation SLB 30_3 fixed-nofixed

The first device which has been performed, is the SLB 30_3_FF, for this test LVDT at the right side have not been located, the values of displacement and rotation are not corrected.

The second specimen of SLB 30_3 is in the fixed-nofixed configuration, for this test there were the LVDT at right side too in order to correct the results.

Focusing the attention on the relative rotation, it is possible to observe that at the values of rotation oscillate between positive and negative values, around the zero, so it can be defined elastic rotation.

The rotation can be defined rigid because the ϕ_L and the ϕ_R are more or less equal.

The vertical displacement follows the trend of applied force. At right the displacements are not zero, it means that the right side in not perfectly fixed.

3.6.1.2 SLB 40_3

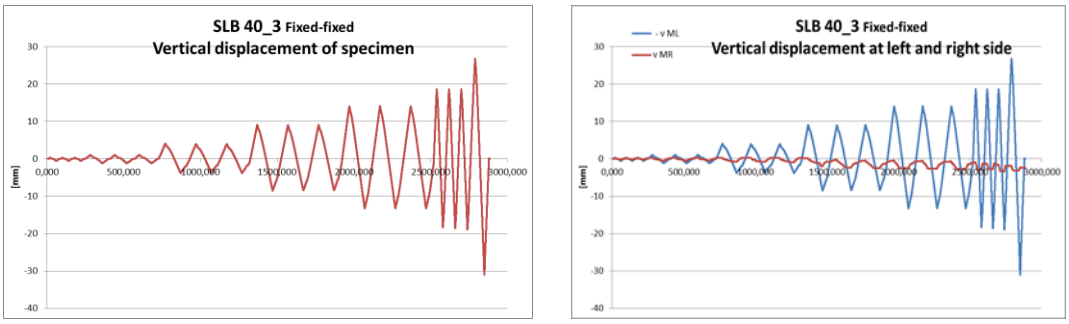

Graph 3-4 vertical displacement SLB 40_3_Fixed-fixed

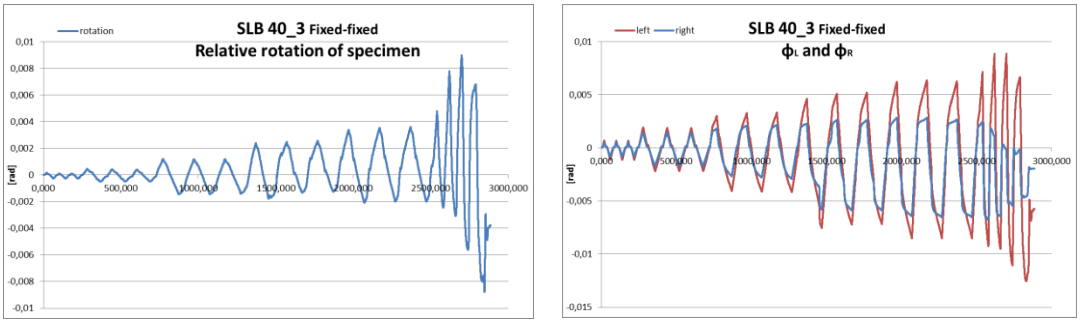

Graph 3-5 Rotation SLB 40_3 fixed-fixed

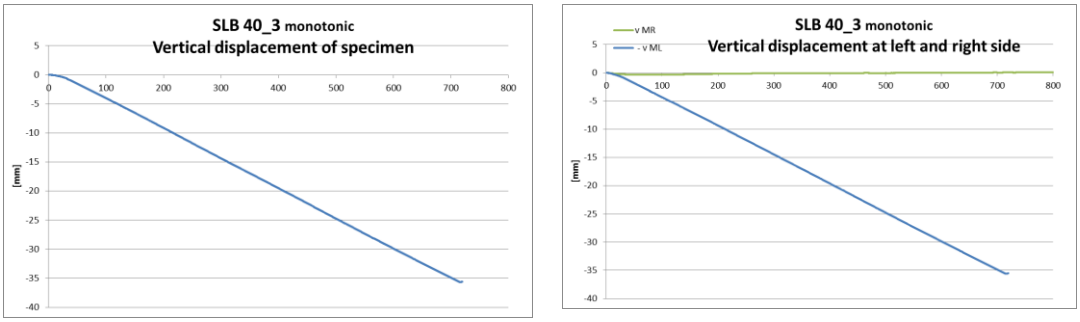

Graph 3-6 vertical displacement SLB 40_3_Fixed-fixed monotonic test

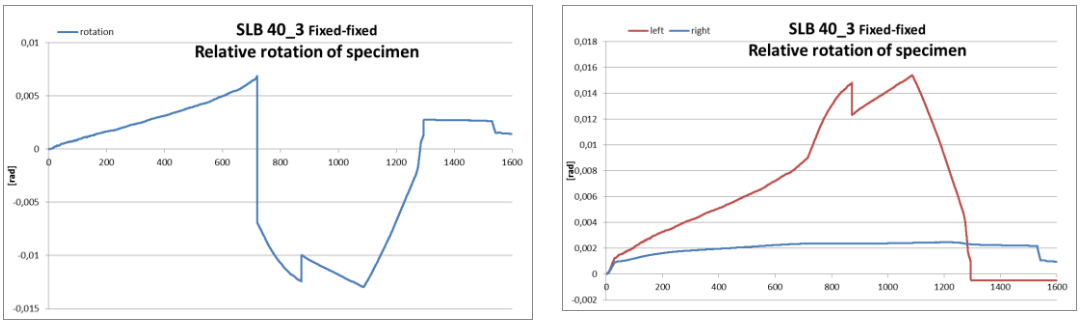

Graph 3-7 Rotation SLB 40_3 fixed-fixed monotonic test

The first specimen has been performed under cyclic load, it is possible to note that for low values of force the rotations at right and at left are equal, so the specimen rotates rigidly. But when the force increases the ϕ_L is greater than the ϕ_R, so the rotation becomes relative rotation. However during the test the rotation remains elastic.

The second specimen has been performed under monotonic load, the vertical displacement increases with time, it coincides with displacement at left, because the displacement at right side is closed to zero.

3.6.1.3 SLB 40_5

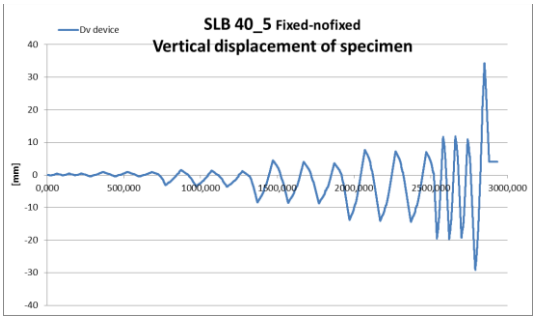

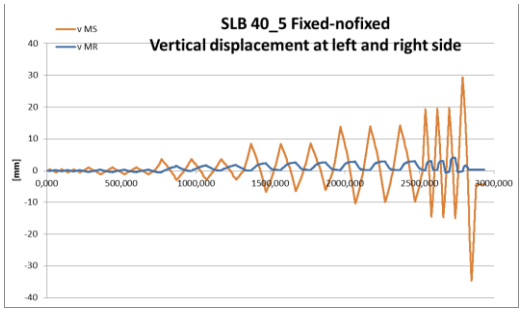

Graph 3-8 vertical displacement SLB 40_5_Fixed-nofixed

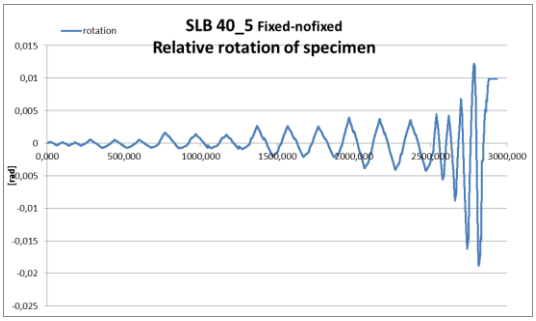

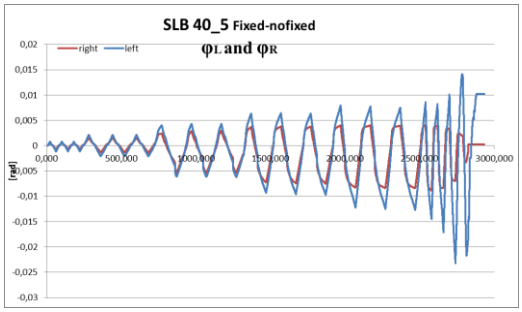

Graph 3-9 Rotation SLB 40_5 fixed-nofixed

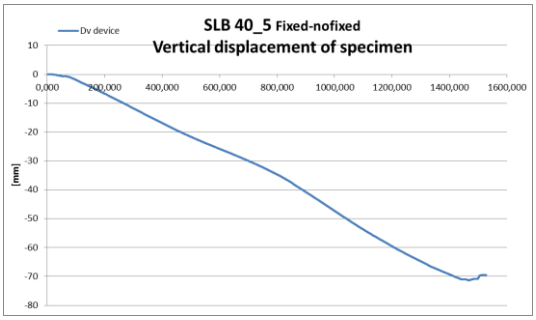

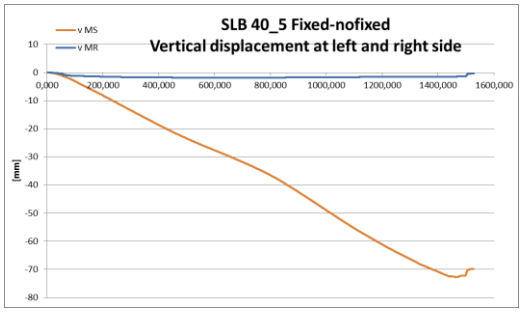

Graph 3-10 vertical displacement SLB 40_5_Fixed-nofixed monotonic test

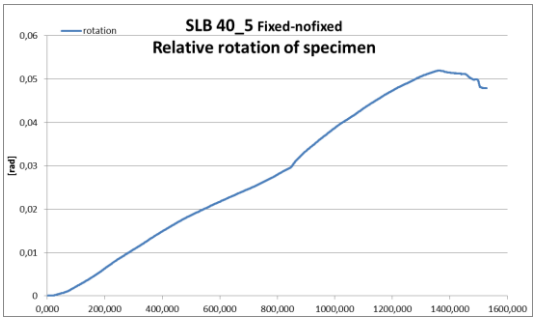

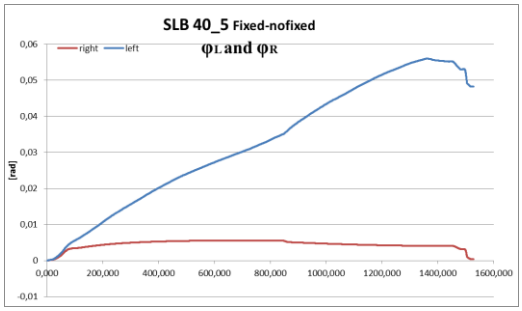

Graph 3-11 Rotation SLB 40_5 fixed-nofixed monotonic test

The SLB 40_5 has been tested under cyclic load and under monotonic load. The considerations about the displacement and rotation for the SLB 40_3 are valid for the SLB40_5.

3.6.1.4 SLB 50_3

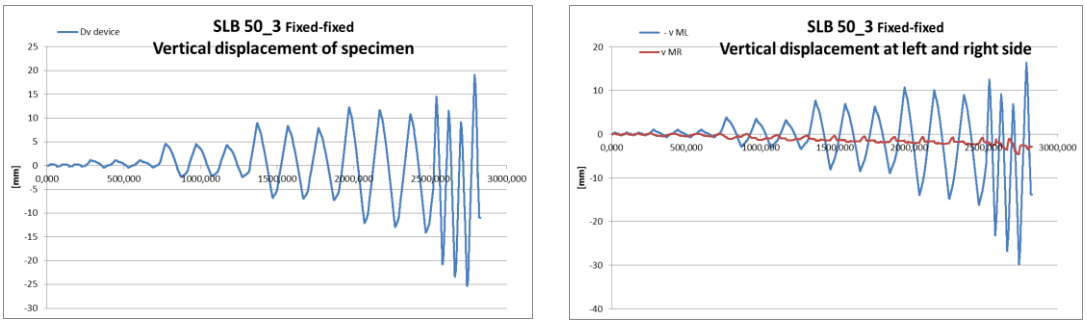

Graph 3-12 vertical displacement SLB 50_3 Fixed-fixed

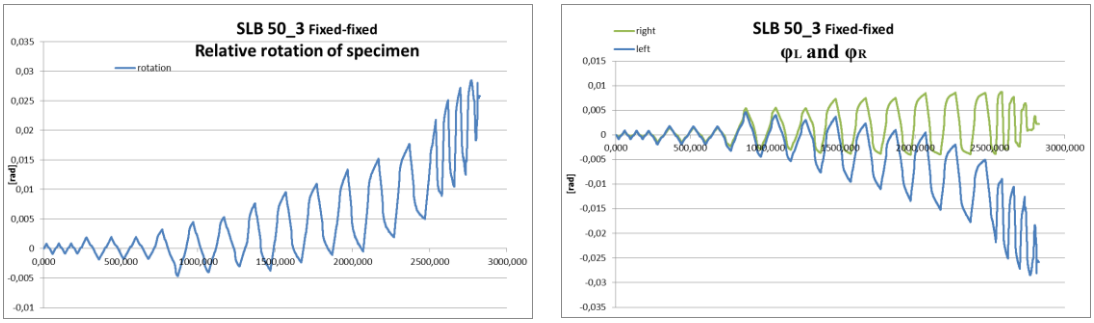

Graph 3-13 Rotation SLB 50_3 fixed-fixed

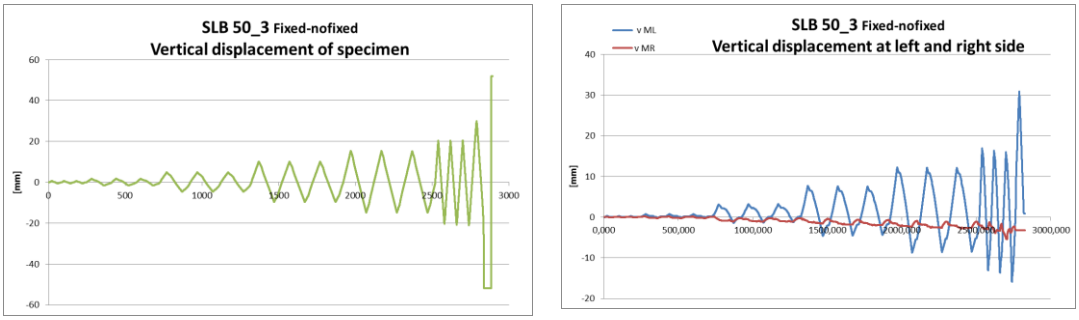

Graph 3-14 vertical displacement SLB 50_3 Fixed-nofixed

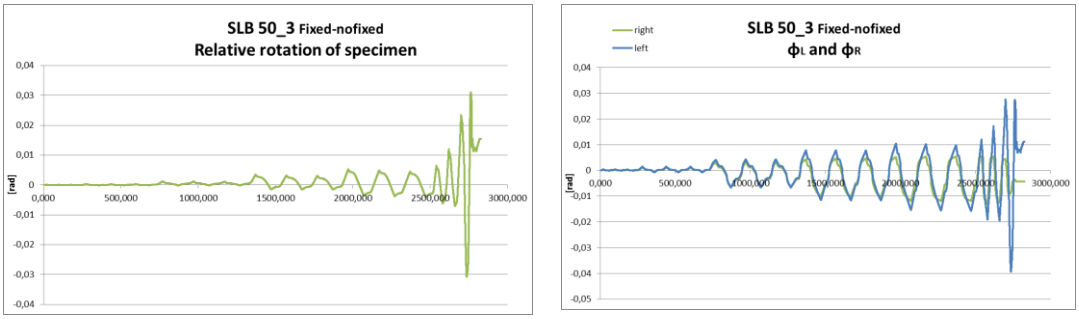

Graph 3-15 Rotation SLB 50_3 fixed-fixed

The two specimens of SLB50_3 are performed under cyclic load, but the first in fixed-fixed condition, the second one in fixed-nofixed condition.

For both specimen, the value of relative displacement follows the trend of cyclic load.

In the fixed-fixed condition, as shown in the **Errore. L'origine riferimento non è stata trovata.**, the relative rotation at the beginning is elastic, it oscillates around the zero axis. When the value of force increases, the $\phi_R$increases too but remains elastic, indeed the ϕ_L becomes plastic. At the right side of the **Errore. L'origine riferimento non è stata trovata.**, the trend of rotation is not around the zero because plastic deformation occurs.

Differently for the second specimen, which is fixed-nofixed condition, for which the rotation remains in the elastic range. During the test the rotation is rigid, in fact $\phi_L$and ϕ_R are equal.

3.6.1.5 SLB 50_5

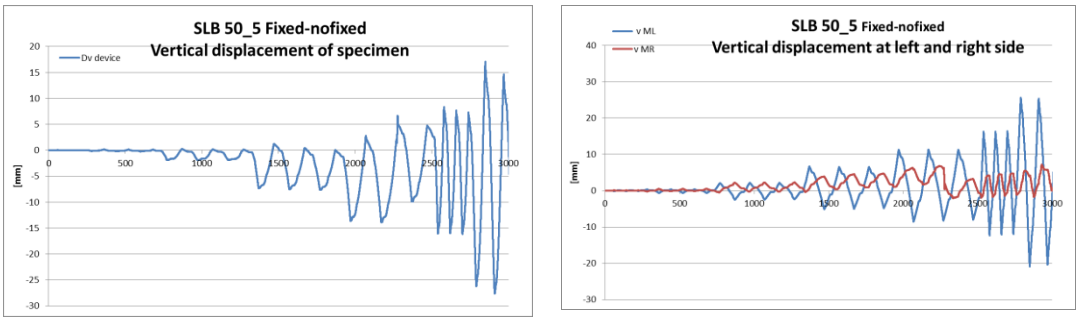

Graph 3-16 vertical displacement SLB 50_5_Fixed-nofixed

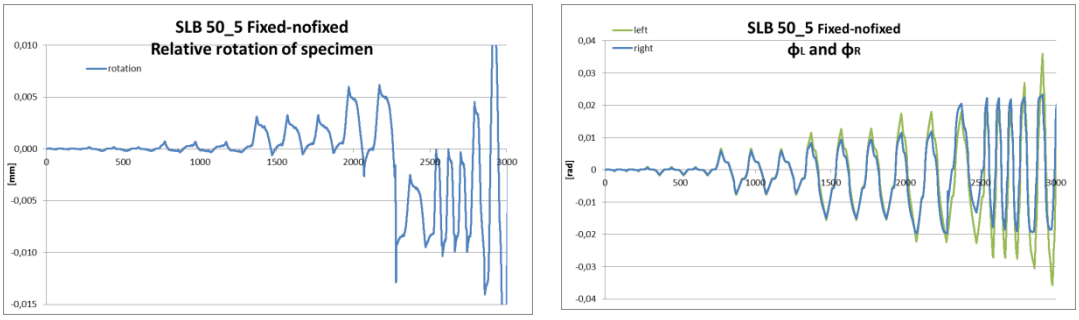

Graph 3-17 Rotation SLB 50_5 fixed-nofixed

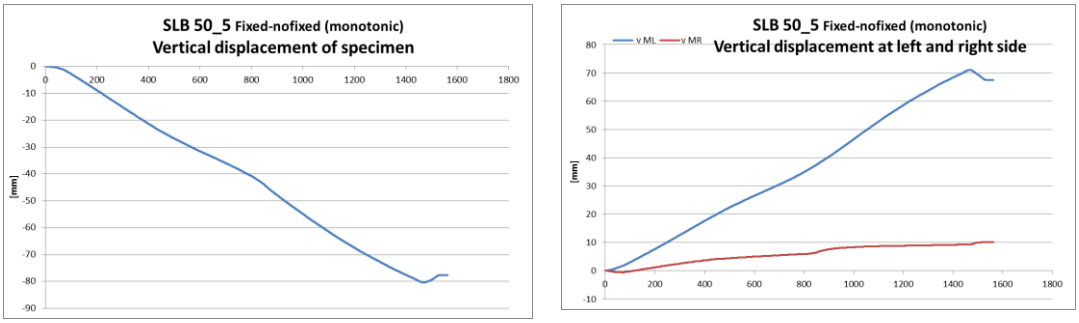

Graph 3-18 vertical displacement SLB 50_5_Fixed-nofixed monotonic test

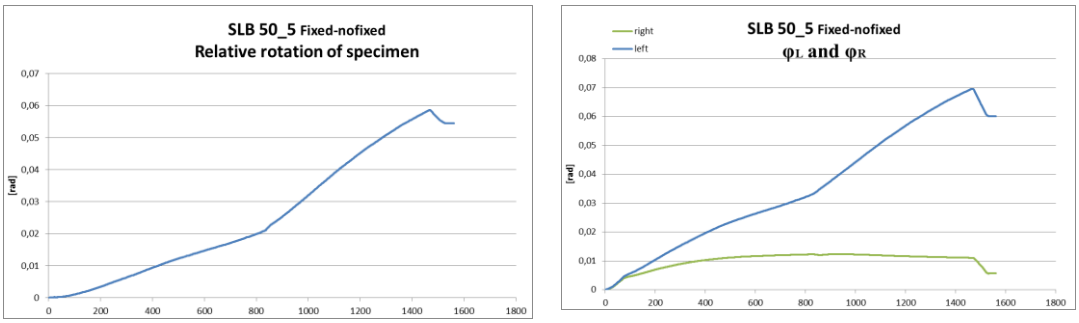

Graph 3-19 Rotation SLB 40_5 fixed-nofixed monotonic test

The SLB 50_5 is performed under cyclic load and monotonic load. The considerations made for the SLB 40_5 are valid for SLB 50_5 too.

3.6.2 Considerations about deformation

The Bozzo Shear Link devices start to dissipate energy for low value of shear force, which correspond plastic deformation in the milled area, called “window”, and in the stiffeners.

The parameter, which quantifies the shear deformation, is the average angular deformation γ_{av}, its expression is given by (3.9):

$$\gamma_{av} = \frac{d}{H'} \tag{3.9}$$

Where d is the relative displacement between the extremes of device, H’ is the total height of windows, obtained as:

$$H' = H - n\,t \tag{3.10}$$

H is the height of web, equal for all devices (110 mm) n is the number of horizontal stiffeners and t is their thickness.

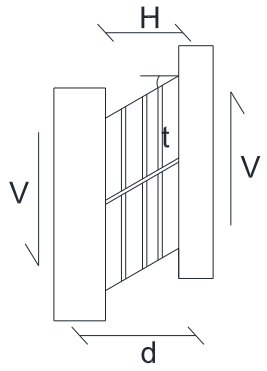

Figure 3.29 Shear deformation of device

The shear deformation of the milled area can be evaluated from the deformation ϵ detected by the strain gauges 1, 2, 3 and 4, located with inclination of 45˚, as shown in Figure 3.23. In fact the shear deformation is calculated as (3.11):

$$\gamma' = 2\epsilon \qquad \textbf{(3.11)}$$

The following graphs show the evolution of γ_{av} and γ' during the test, for each specimen.

It is possible to note that at the beginning, which correspond low values of force, the γ' detected by the four strain gauges, are very closed to the γ_{av}, so the deformation is defined as simple shear deformation. But when the force increases, the deformation increases too and the values of γ' are different from γ_{av}. It means that there are also flexure deformations.

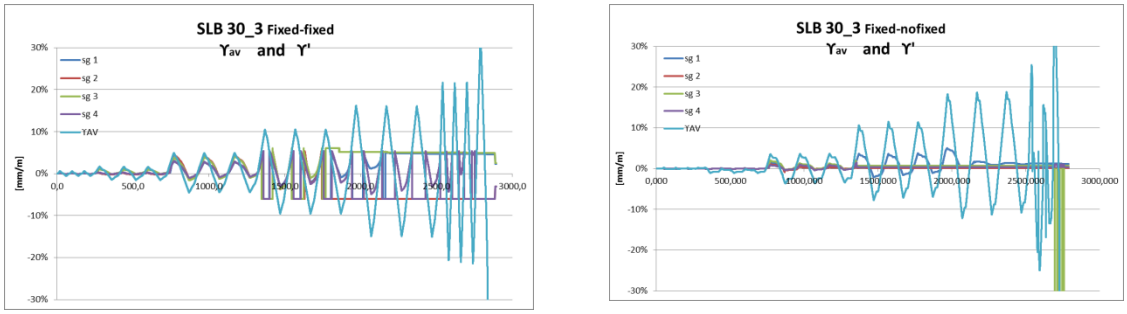

Graph 3-20 SL30_3:γ_{AV} *and* γ'

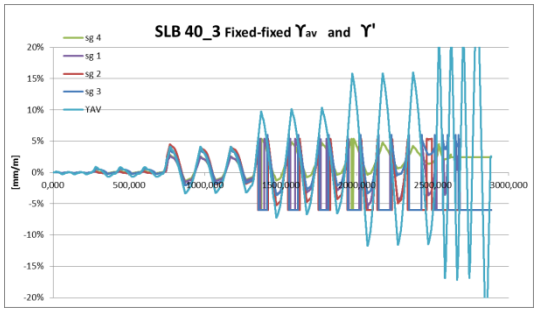

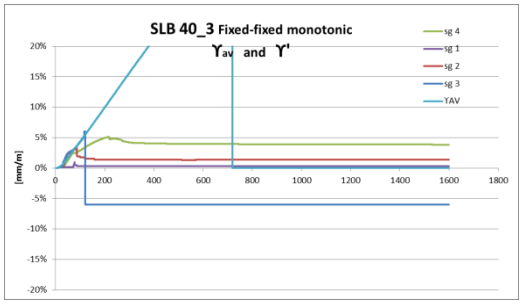

Graph 3-21 SL40_3:γ_{AV} *and* γ'

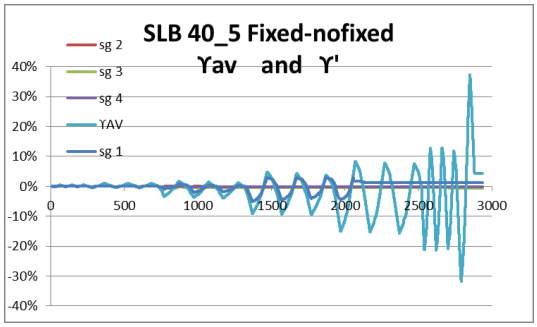

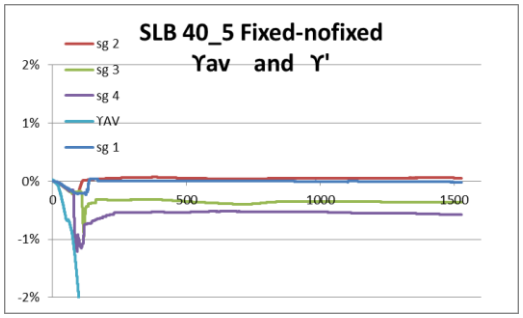

Graph 3-22 SL40_5: γ_{AV} *and* γ'

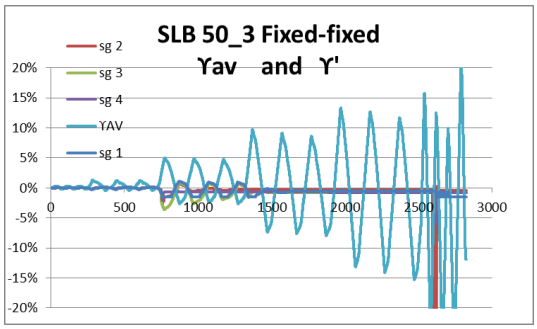

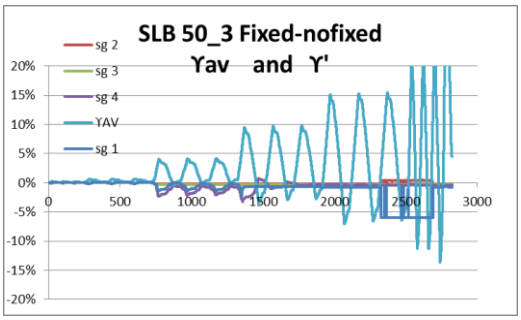

Graph 3-23 SL50_3:γ_{AV} *and* γ'

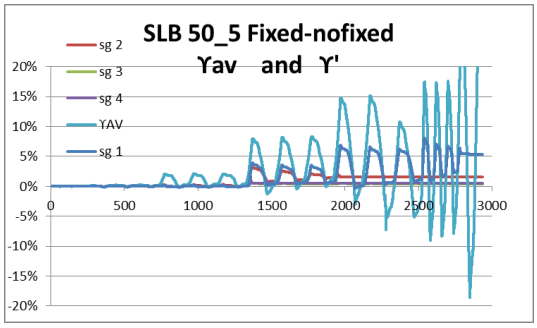

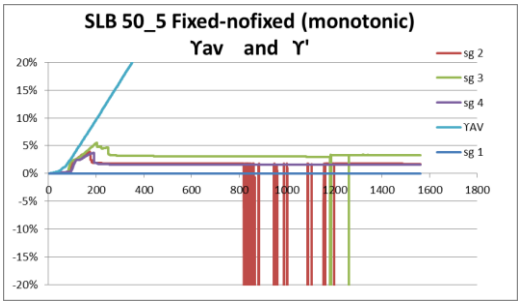

Graph 3-24 SL50_5:γ_{AV} *and* γ'

From the measurement of the SLB40_5, it comes out that the average shear deformation is twice the shear deformation of milled area, as shown in Figure 3.30:

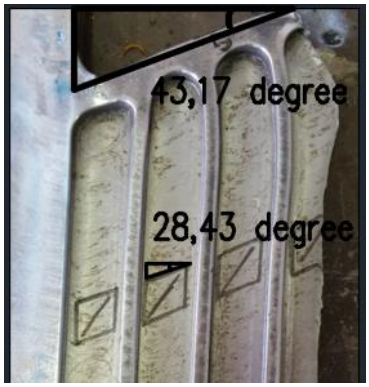

Figure 3.30 $\gamma_{av} and\ \gamma'$ measured in the laboratory

The strain gauges 5 and 6 record the axial deformations of stiffeners. They are located as in Figure 3.23 (strain gauge 5 is at the top and strain gauge 6 is at the bottom). The presence of these justifies that the device deformation is not only in the shear, but in bending too.

The Figure 3.31 represents the pattern of stiffeners in deformed condition, it is possible to note that in the FF condition the both strain gauges detect the same sign of deformation, in fact they are located symmetrically in relation to the inflection point of bending moment, so they detect the stretched fibres or compressed fibres at the same time. Conversely in the second condition, in which the strain gauges don't read the same sign of deformation: when once detects compressed fibres the other detects stretched fibres.

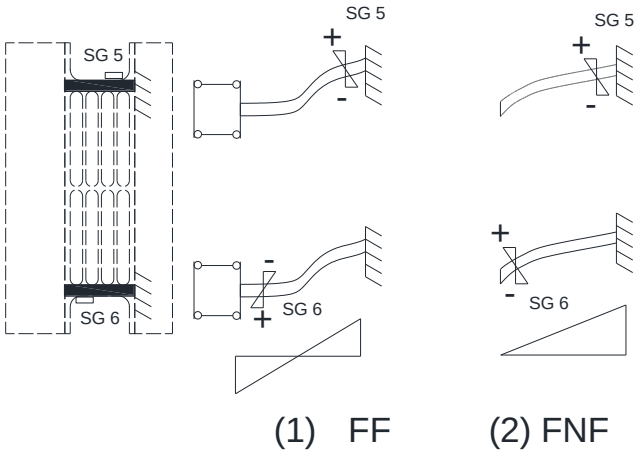

Figure 3.31 Bending moment for two different boundary conditions

It is evident from the following graphs.

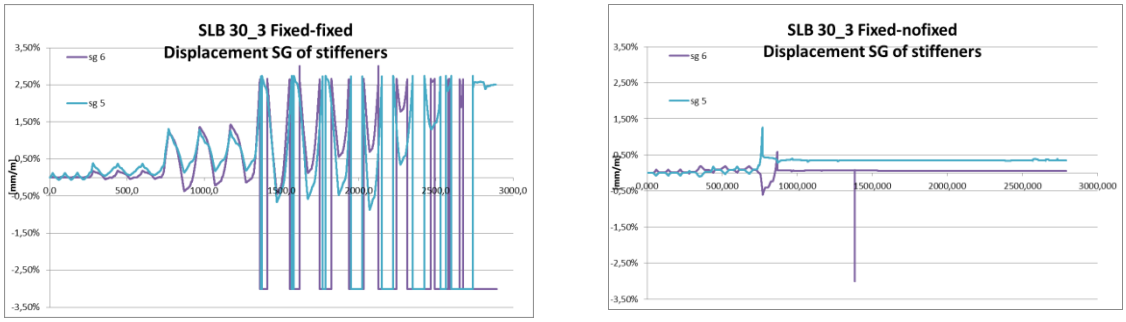

Graph 3-25 SL30_3:axial deformation

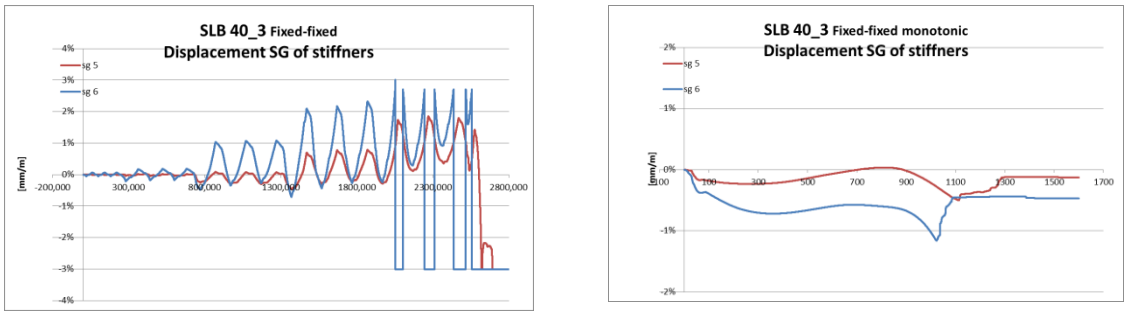

Graph 3-26 SL40_3:axial deformation

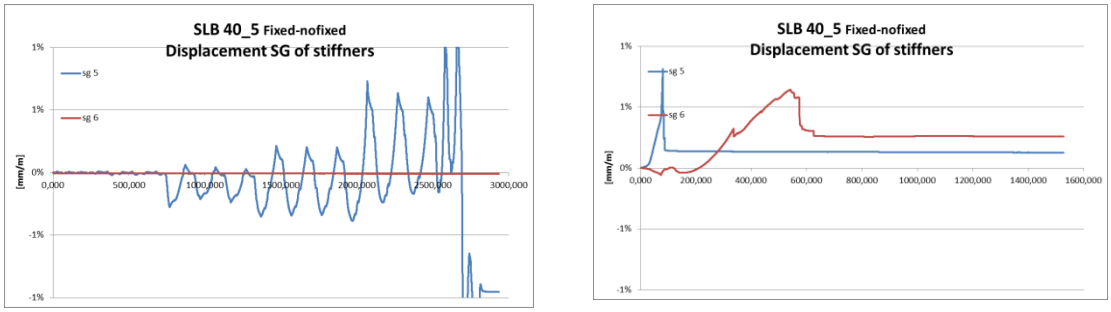

Graph 3-27 SL40_5:axial deformation

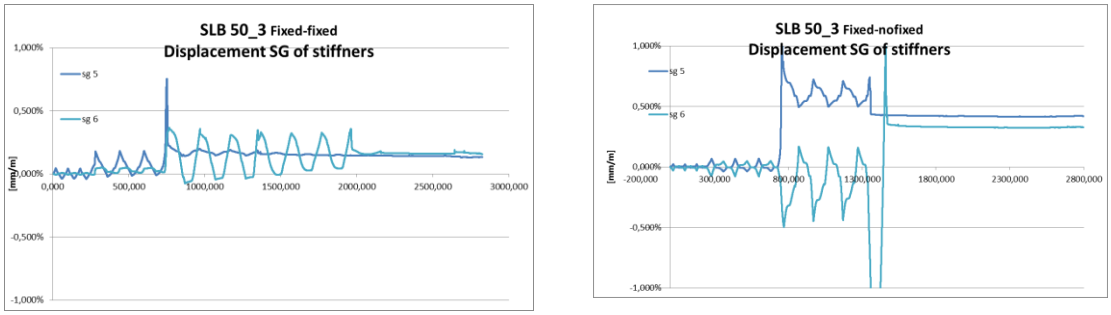

Graph 3-28SL50_3:axial deformation

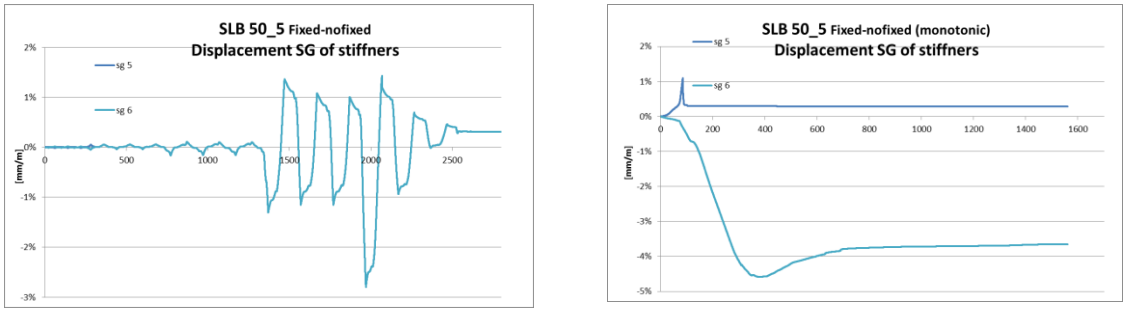

Graph 3-29 SL50_5:axial deformation

From the graphs it is possible to note that for the fixed-fixed condition the strain gauges 5 and 6 detect the same sign, instead, for the fixed-nofixed condition the trend of the curves are opposite, as described in the Figure 3.31.

3.6.3 Yielding Force and maximum force of SLB device

The value of Yielding force, and its correspondent displacement, of the Bozzo Shear Link, are established by the loss of linearity of relation force-displacement.

The maximum force, and its correspondent displacement, is determined by the loss of resistance.

The SLB 40_3 and SLB 40_5 are also tested under monotonic load, in this case the yielding force and the maximum force are easy determined.

The SLB30_3, SLB50_3, SLB 50_5 are tested only under cyclic load, for them it refers to the hysteretic curve.

For the first cycles of hysteretic curve, the force reaches low value, so they are not appropriate for determination of Yielding force because there is not a visible loss of linearity.

The Figure 3.32 shows the first cycles, to which is added the linear regression, used in order to evaluate Yielding force and yielding displacement. Furthermore from these two values the initial stiffness, which is the elastic stiffness, is computed.

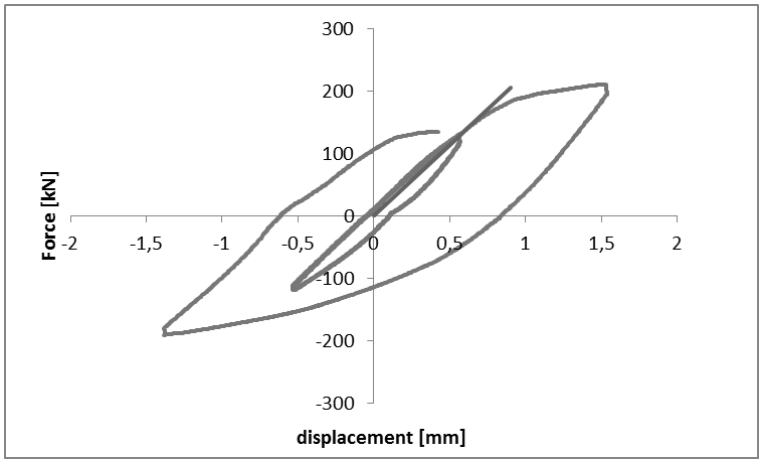

Figure 3.32 Hysteretic cycle and linear regression

The maximum force, which comes out from the hysteretic curve, refers to the maximum value of force before the device failure.

The table below gives the analysed dates, they are:

F_y: yielding force

d_y: yielding displacement

k_{el}: initial stiffness

F_{Max}: maximum force

d_{Max}: maximum displacement corresponding to the maximum force

	Fy	dy	kel	Fmax	dmax
	[kN]	[mm]	[kN/mm]	[kN]	[mm]
SL30_3_FF	137,2	0,6	228,7	434,3	20,3
SL30_3_FNF	208,5	3,2	66,1	396,2	18,6
SL40_3_FF	240,4	0,7	358,3	517,0	20,0
SL40_3_FF(m)	242,5	1,5	163,0	563,0	43,6
SL40_5_FNF	203,0	0,7	407,6	740,0	19,0
SL40_5_FNF(m)	364,4	0,8	432,5	803,6	37,3
SL50_3_FF	325,3	0,7	464,7	637,0	20,7
SL50_3_FNF	228,0	0,5	456,0	655,0	19,0
SL50_5_FNF	160,0	0,3	533,3	1000,0	25,0
SL50_5_FNF(m)	334,0	0,6	556,7	1011,3	42,7

It is noted that changing the boundary condition, i.e. from fixed-fixed to fixed-nofixed, there is no a change of the Yielding force and Maximum force. For the SLB30_3 the values of elastic stiffness in fixed-fixed condition is greater than the fixed-nofixed condition about 70%, for SLB 50_3 about 2%, they are very closed.

For the SLB 40_5 the elastic stiffness is not equal when the force is in compression and is in tension, so the elastic stiffness is evaluated as the secant stiffness.

It is important to note that for the specimens SLB 40_3,SLB 40_5 and SLB 50_5, which are tested under cyclic and monotonic load, the maximum force has more or less the same value, but it is reached for different value of displacement. In particular in the case of cyclic load the maximum force is reached for smaller values of displacement, around 20 mm, indeed under monotonic load the maximum force is reached around 40mm, as shown in the following graphs.

It is due to the cyclic hardening for which the maximum value occurs before than the monotonic load. It justify the chosen of plasticity model of Chaboche's model.

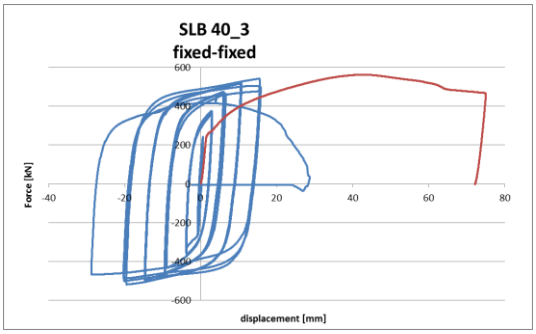

Graph 3-30 SLB40_3: monotonic curve and cyclic curve

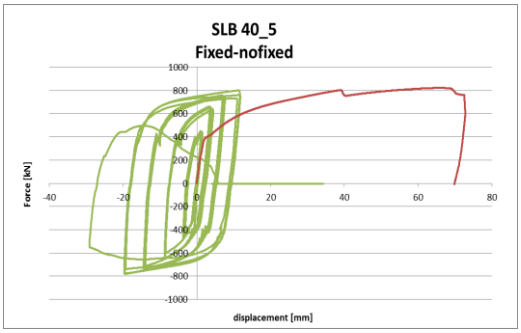

Graph 3-31 SLB40_5: monotonic curve and cyclic curve

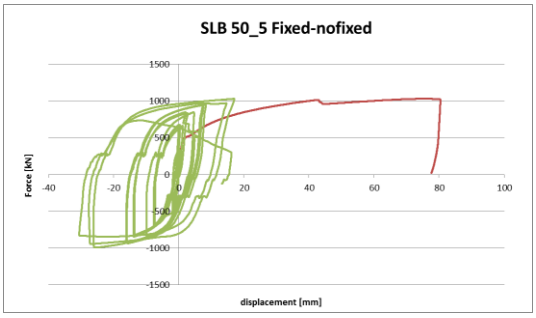

Graph 3-32 SLB50_5: monotonic curve and cyclic curve

In the monotonic curve of SLB 40_5 and SLB 50_5 there is a “step”, it is in correspondence of the crack formation at the stiffeners, but after this point the specimen is able to carry load. However this point is considered as the failure point.

3.6.4 Hysteretic behaviour and dissipated energy

Perfect elastic materials possess an ideal linear stress-strain characteristic, a cyclic stress generates a strain in these materials which is cyclically variable and in phase with the stress. Inelasticity is always present although very fine measurements are required to detect it. In stress-strain coordinates, the geometrical locus of operational point becomes a closed loop, known as *hysterezis loop*. Since materials absorb elastic energy under cyclic stress, the unloading curve is always situated underneath the loading curve, the hysteresis loop configuration depending on the inelasticity type. The area of the surface enclosed within the hysteresis loop always equals the amount of energy dissipated in the material upon one loading-unloading cycle. This loop evolves with the number of stress cycles and may offer useful information upon the material state. Hysteresis variation is clearly highlighted upon modification of test parameters.

The Figure 3.33 represents a simple pattern of experimental test: the right side is fixed and at left side the actuator applies the cyclic force.

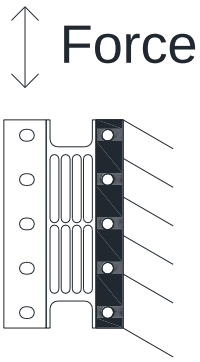

Figure 3.33 Simple pattern of experimental test

The values of force are obtained from the cell load. The displacement is the relative displacement of the device

If the displacement, identified by the LVDT 0, is taken in account, the hysteretic curve is not corrected, if the relative displacement is considered, the corresponding hysteretic curve is corrected.

All the results are provided below.

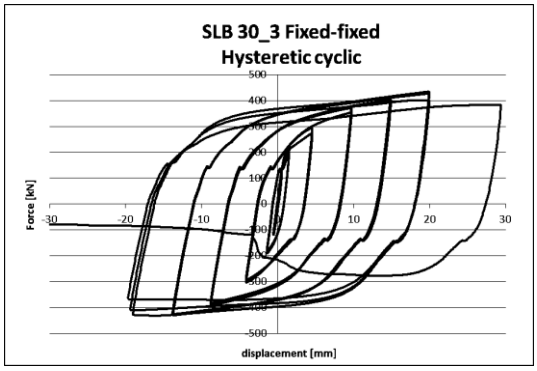

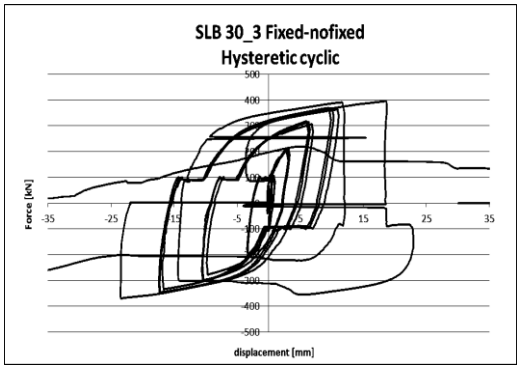

Graph 3-33 SL30_3: hysteretic curve for FF and FNF conditions

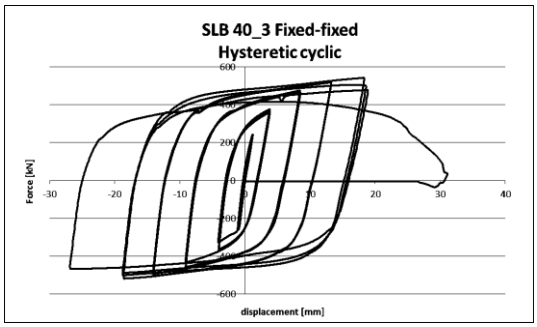

Graph 3-34 SL40_3:Hysteretic curve FF condition

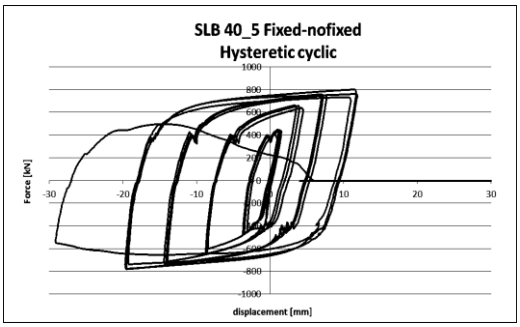

Graph 3-35 SL40_5:Hysteretic curve FNF condition

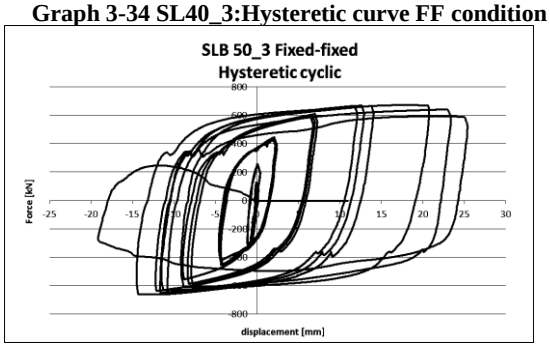

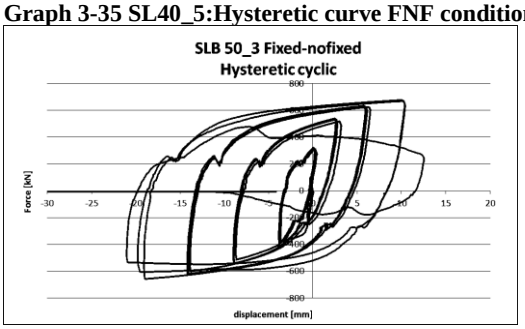

Graph 3-36 SL50_3: hysteretic curve for FF and FNF conditions

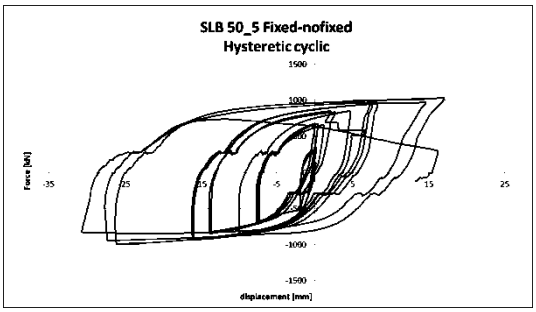

Graph 3-37 SL50_5: hysteretic curve for FNF condition

Under cyclic load, linear dependence only holds for the initial stage. After a number of cycles, after the first plastic deformation, the nonlinearity of stress-strain curve appears.

From the graphs it is possible to appreciate big and stable loop for the fixed-fixed condition before the failure. In the fixed-nofixed condition the loop appears no symmetric with respect to the force axis.

For the SLB40_5, SLB 50_3 and SLB 50_5 there is an accumulation of strain on the one hand.

For the SLB 30_3 it is possible to note that the two boundary conditions reach the same value of maximum force, more or less for at the same value of displacement, but the areas enclosed by the curves are different, in particular that of fixed-fixed condition is greater than the fixed-nofixed condition.

If the shape of the curve is analysed, in the condition fixed-nofixed, some slips occur, due to the sliding of bolts in the slotted holes at left side. It is less evident in the fixed-fixed condition.

An important aspect to be observed is that the cyclic behaviour of dissipators is not correctly described by kinematic hardening model, because in each specimen an expansion of plastic domain occurs. It means that there is an isotropic hardening effect too.

This is confirmed by the fact that if the plasticity has been described by kinematic model, the envelope of cyclic loop should coincide with the curve obtained from the monotonic test. It is possible to note, from the Figure 3.34, that the envelope curve and the monotonic curve are not equal, in particular the envelope is greater. There is a cyclic hardening

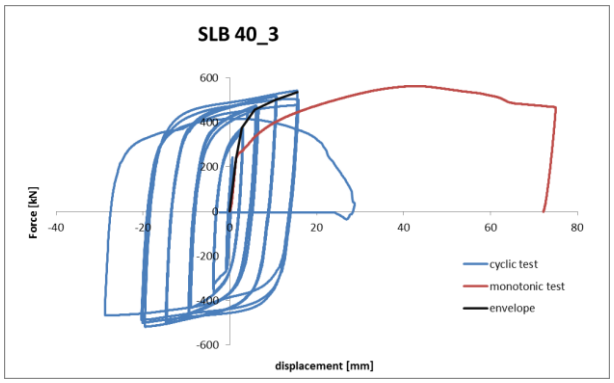

Figure 3.34 Cyclic test, monotonic test and envelope

When the both hardening rule are used we talk about mixed hardening. The cyclic plasticity of Bozzo Shear Link can be described by a suitable superposition of kinematic and isotropic hardening rules. This theme has deepened in the following chapter.

The total inner area of loop represents the dissipated energy of Bozzo Shear Link device.

For each device the total energy before the failure, has been calculated, as the sum of dissipated energy E_d and elastic strain energy E_s, shown in the Figure 3.34:

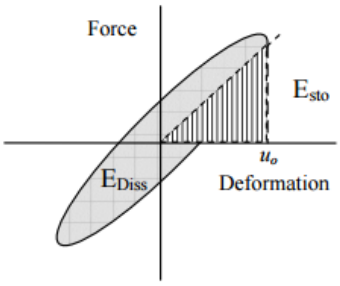

Figure 3.35 Dissipated energy and elastic strain energy

The equivalent damping ratio is also computed with the equation (3.12):

$$\zeta_{\text{eq}} = \frac{Ed}{4\pi E_s} \qquad \textbf{(3.12)}$$

The total dissipated energy and the equivalent damping ratio refer to the loop before that the failure occurs. For all devices, except for the SLB 50_5, the loop is characterized by the maximum displacement about 15 mm.

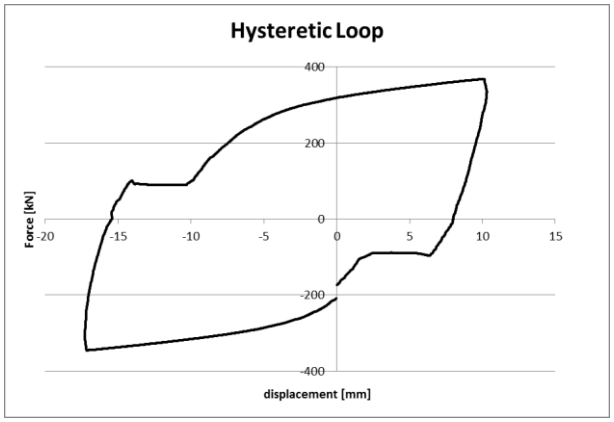

Figure 3.36 Hysteretic loop for which the total dissipated energy is computed

The elaborated results are summarized in the Table 3.7:

	Ed	Es	Etot	ζ_{eq}
	[KJ]	[KJ]	[KJ]	[-]
SLB 30_3_FF	16,28	3,00	19,28	43,20%
SLB 30_3_FNF	11,15	2,23	13,39	39,74%
SLB 40_3_FF	19,64	3,23	22,87	48,36%
SLB 40_5_FNF	22,84	4,01	26,85	45,37%
SLB 50_3_FF	24,43	3,84	28,28	50,62%
SLB 50_3_FNF	17,13	3,09	20,21	44,20%
SLB 50_5_FNF	61,32	10,91	72,23	44,8%

Table 3.7 Elaborated results

It is possible to note that changing the boundary condition, in particular from fixed-nofixed condition to fixed-fixed condition, equivalent damping ratio increases about 10%.

3.6.5 Qualitative description and analysis of failure

The followings figure show the specimen before and after the test:

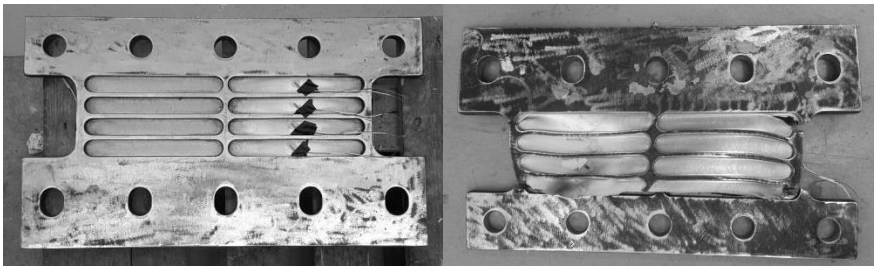

Figure 3.37 Specimen before (left) and after (right) the test

The two load condition, monotonic and cyclic load, give two kind of failure process, which are described qualitatively in this subparagraph.

At the beginning of the cyclic test, the low axial deformation at the stiffeners and shear deformation at the windows are recorded. This is in agree with the deformed shape of the device: it is impossible to see some deformations. When the value of the shear force increases, the cracking occurs at the stiffeners, in particular it is located in the corner between the web and wing, where tensions are concentrated. Subsequently the crack spreads rapidly in the windows, as shown in Figure 3.38. Only then a little buckling at the windows occurs.

Figure 3.38 Evolution of failure for the cyclic test

The failure process for the monotonic test develops differently, as it is possible to observe from the Figure 3.39. When the force value increases , the local buckling at the thinner part of shear link, i.e. the windows, is reaches, as shown in the followings figures. This because it is the case of large deflection. The plate doesn't collapse immediately but shows resistance.

For high value of displacement, the cracking at the stiffeners starts and it propagates through the windows. This point corresponds to the loss of resistance. Anyway the SLB40_5 and SLB50_5 at the crack formation, not collapse instantly but show a margin of resistance.

However, the SLB50_5, in both tests, shows the same behaviour of cyclic test.

Figure 3.39 Evolution of failure for monotonic test

This is the behaviour of the actual Bozzo Shear Link device, for which the degradation stats from the lateral stiffeners. A new model of device will be developed, characterized by lateral stiffener larger than the actual lateral stiffeners, this allows that the degradation affects before the milled areas and after the lateral stiffeners.

4 NUMERICAL MODELLING OF BOZZO SHEAR LINK

In this chapter the accurate description of numerical models of the f Bozzo Shear Link, which are performed at the laboratory, are described.

It is possible to define the numerical model thanks to the experimental results. In fact the numerical parameters are calibrated on the considerations of real behaviour of devices.

One of them is the plasticity model which characterizes the nonlinear behaviour of SLB, there are shown the different model of plasticity and hardening, focusing the attention on the chosen model, which is Chaboche's model.

The numerical modelling is done by the software Ansys Workbench, that with a friendly interface permits to perform accurate numerical analysis.

In the end the numerical results are shown and discussed. The data are summarized in tabular form, showing for each device the design parameters.

4.1 Model of plasticity and hardening

The theory of linear elasticity is useful for modelling materials which undergo small deformations and which return to their original configuration upon removal of load. Almost all real materials will undergo some permanent deformation, which remains after removal of load. With metals, significant permanent deformations will usually occur when the stress reaches some critical value, called the yield stress, a material property. Elastic deformations are termed reversible; the energy expended in deformation is stored as elastic strain energy and is completely recovered upon load removal. Permanent deformations involve the dissipation of energy; such processes are termed irreversible, in the sense that the original state can be achieved only by the expenditure of more energy.

In the one-dimensional (uniaxial test) case, a specimen will deform up to yield and then generally hardening, Figure 4.1.

In the perfectly plastic case, once the stress reaches the yield point (A), plastic deformation ensues, so long as the stress is maintained at Y. If the stress is reduced, elastic unloading occurs. In the hardening case, once yield occurs, the stress needs to be continually increased in order to drive the plastic deformation.

If the stress is held constant, for example at B, no further plastic deformation will occur; at the same time, no elastic unloading will occur. Note that this condition cannot occur in the perfectly-plastic case, where there is one of plastic deformation or elastic unloading.

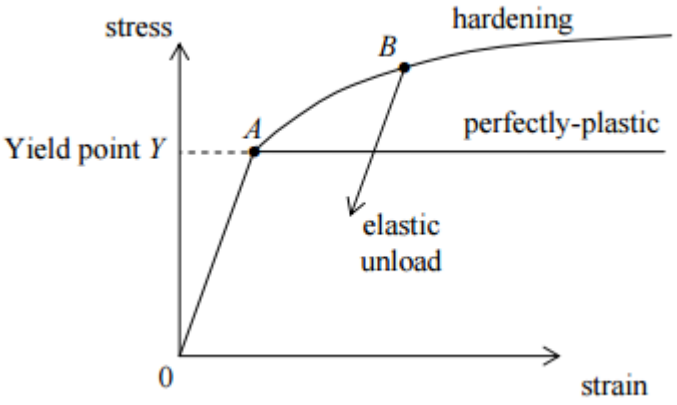

Figure 4.1 uniaxial stress-strain curve (for a typical metal)

The constitutive models for elastic-plastic behaviour start with a decomposition of the total strain into elastic and plastic parts and separate constitutive models are used for each. The essential characteristics of the plastic constitutive models are:

- The yield criterion that defines the material state at the transition from elastic to elastic-plastic behaviour.
- The flow rule that determines the increment in plastic strain from the increment in load.
- The hardening rule that gives the evolution in the yield criterion during plastic deformation.

From Figure 4.1, a monotonic loading to σ' gives a total strain ε'. The total strain is additively decomposed into elastic and plastic parts:

$$\varepsilon' = \varepsilon^{el} + \varepsilon^{pl} \quad \textbf{(4.1)}$$

The stress is proportional to the elastic strain $\varepsilon^{pl:}$

$$\sigma = D\varepsilon^{el} \quad \textbf{(4.2)}$$

and the evolution of plastic strain ε^{pl} is a result of the plasticity model.

For a general model of plasticity that includes arbitrary load paths, the flow theory of plasticity decomposes the incremental strain tensor into elastic and plastic strain increments:

$$d\varepsilon = d\varepsilon^{el} + d\varepsilon^{pl} \quad \textbf{(4.3)}$$

The increment in stress is then proportional to the increment in elastic strain, and the plastic constitutive model gives the incremental plastic strain as a function of the material state and load increment.

The yield criterion is a scalar function of the stress and internal variables and is given by the general function:

$$f(\sigma, \xi) = 0 \quad \textbf{(4.4)}$$

Where ξ represents a set of history dependent scalar and tensor internal variables.

The equation (4.4) is a general function representing the specific form of the yield criterion for each of the plasticity models. The function is a surface in stress space and an example, plotted in principal stress space, as shown in this figure:

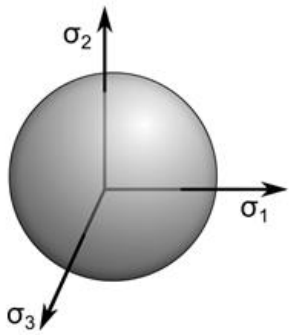

Figure 4.2 Yield surface in principal stress space

Stress states inside the yield surface are given by $f(\sigma,\xi) < 0$ and result in elastic deformation. The material yields when the stress state reaches the yield surface and further loading causes plastic deformation. Stresses outside the yield surface do not exist and the plastic strain and shape of the yield surface evolve to maintain stresses either inside or on the yield surface.

The evolution of plastic strain is determined by the *flow rule*:

$$d\varepsilon^{pl} = d\lambda \frac{\partial Q}{\partial \sigma} \tag{4.5}$$

where $d\lambda$ is the magnitude of the plastic strain increment and Q is the plastic potential. When the plastic potential is the yield surface from equation (4.4), the plastic strain increment is normal to the yield surface and the model has an associated flow rule, as shown in this figure:

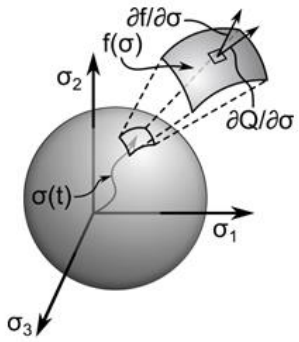

Figure 4.3 Plastic strain flow rule

These flow rules are typically used to model metals and give a plastic strain increment that is proportional to the stress increment. If the plastic potential is not proportional to the yield surface, the model has a non-associated flow rule, typically used to model soils and granular materials that plastically deform due to internal frictional sliding. For non-associated flow rules, the plastic strain increment is not in the same direction as the stress increment.

For a plastic potential that is similar to the yield surface, the plastic strain direction is not significantly different from the yield surface normal, and the degree of asymmetry in the material stiffness is small. In this case, a symmetric analysis can be used, and a symmetric material stiffness tensor will be formed without significantly affecting the convergence of the solution.

The yield criterion for many materials depends on the history of loading and evolution of plastic strain. The change in the yield criterion due to loading is called *hardening* and is defined by the hardening rule. Hardening behaviour results in an increase in yield stress upon further loading from a state on the yield surface so that for a plastically deforming material, an increase in stress is accompanied by an increase in plastic strain.

Two common types of hardening rules are isotropic and kinematic hardening.

The *isotropic hardening* is where the yield surface remains the same shape but expands with increasing stress. For isotropic hardening, the yield surface given by equation (4.4) has the form:

$$F(\sigma) - \sigma_y(\xi) = 0 \tag{4.6}$$

where $F(\sigma)$ is a scalar function of stress and $\sigma_y(\xi)$ is the yield stress.

Plastic loading from $\sigma(t_1)$ to $\sigma(t_2)$ increases the yield stress and results in uniform increase in the size of the yield surface, as shown in this figure:

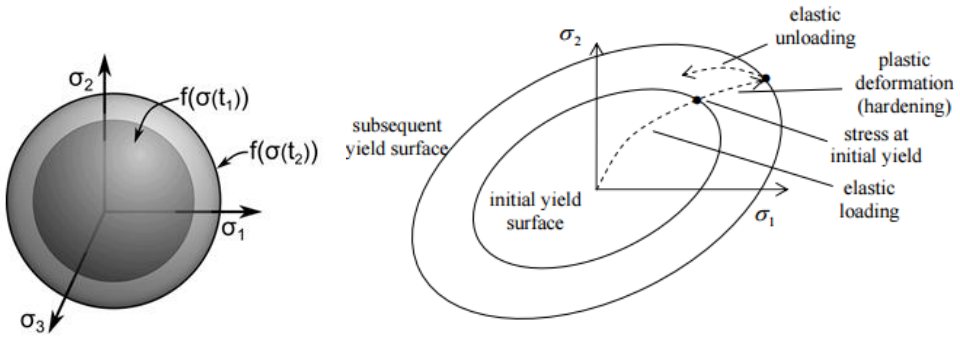

Figure 4.4 Isotropic hardening of the Yield surface

This type of hardening can model the behaviour of materials under monotonic loading and elastic unloading, but often does not give good results for structures that experience plastic deformation after a load reversal from a plastic state.

The *kinematic hardening* is where the yield surface remains the same shape and size but merely translates in stress space. For kinematic hardening, the yield surface has the form:

o

$$f(\sigma - \alpha, \xi) = 0 \tag{4.7}$$

where α is the back stress tensor or shiftstress; the yield surface is shifted relative to the stress-space axes by α

As shown in the following figure (Figure 4.5), the back stress tensor is the centre (or origin) of the yield surface, and plastic loading from $\sigma(t_1)$ to $\sigma(t_2)$ results in a change in the back stress and therefore a shift in the yield surface:

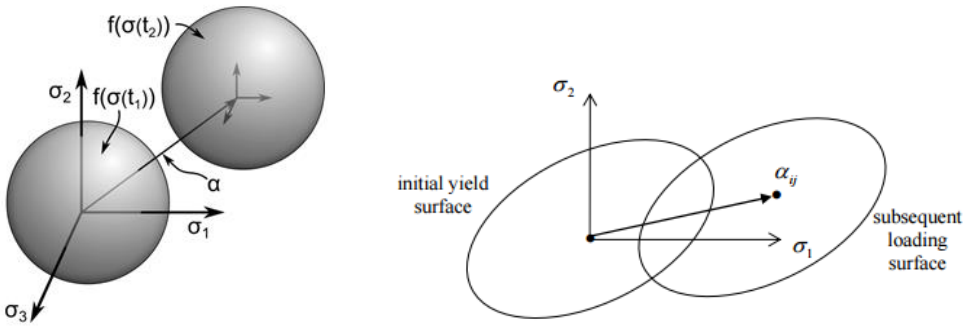

Figure 4.5 Kinematic hardening of the Yield surface

Kinematic hardening is observed in cyclic loading of metals. It can be used to model behaviour such as the Bauschinger effect, where the compressive yield strength reduces in response to tensile yielding. It can also be used to model plastic ratcheting, which is the build-up of plastic strain during cyclic loading.

Many materials exhibit both isotropic and kinematic hardening behaviour, and these hardening rules can be used together to give the combined hardening model. Other hardening behaviours include changes in the shape of the yield surface in which the hardening rule affects only a local region of the yield surface, and softening behaviour in which the yield stress decreases with plastic loading.

Hardening models assume a *von Mises yield criterion*.

4.1.1 Von Mises Yield Criterion

The von Mises yield criterion is commonly used in plasticity models for a wide range of materials. It is a good first approximation for metals, polymers, and saturated geological materials. The criterion is isotropic and independent of hydrostatic pressure, which can limit its applicability to microstructure materials and materials that exhibit plastic dilatation.

The von Mises yield criterion is:

$$f(\sigma, \sigma_y) = \sigma_e - \sigma_y = 0 \tag{4.8}$$

where σ_e is the von Mises effective stress, also known as *the von Mises equivalent stress*,

$$\sigma_e = \sqrt{\frac{2}{3}(\sigma : \sigma - \frac{1}{3} tr(\sigma)^2)} \tag{4.9}$$

and σ_y is the yield strength and corresponds to the yield in uniaxial stress loading.

In principal stress space, the yield surface is a cylinder with the axis along the hydrostatic line $\sigma_1 = \sigma_2 = \sigma_3$ and gives a yield criterion that is independent of the hydrostatic stress, as shown in the following figure:

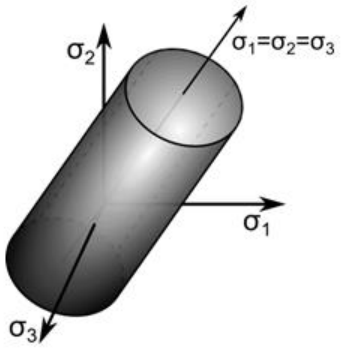

Figure 4.6 Yield surface for von Mises Yield Criterion

For an associated flow rule, the plastic potential is the yield criterion in equation (4.8) and the plastic strain increment is proportional to the deviatoric stress

$$d\varepsilon^{pl} = d\lambda(\sigma - \frac{1}{3}tr(\sigma)) \quad \textbf{(4.10)}$$

4.1.2 Isotropic hardening

During plastic deformation, isotropic hardening causes a uniform increase in the size of the yield surface and results in an increase in the yield stress. The yield criterion has the form:

$$F(\sigma) - \sigma(\xi) = 0 \quad \textbf{(4.11)}$$

where $F(\sigma)$ is a scalar function of stress and $\sigma_y(\xi)$ is the yield stress that evolves as a function of the set of material internal variables ξ. This type of hardening can model the behaviour of materials under monotonic loading and elastic unloading, but often does not give good results for structures that experience additional plastic deformation after a load reversal from a plastic state. Two general classes of isotropic hardening models are available: bilinear and multilinear. Each of the hardening models assumes a von Mises yield criterion and includes an associated flow rule.

Bilinear isotropic hardening is described by a bilinear effective stress versus effective strain curve. The initial slope of the curve is the elastic modulus of the material. Beyond the user-specified initial yield stress σ_0, plastic strain develops and stress-vs.-total-strain continues along a line with slope defined by the user-specified tangent modulus E_T. The tangent modulus cannot be less than zero or greater than the elastic modulus.

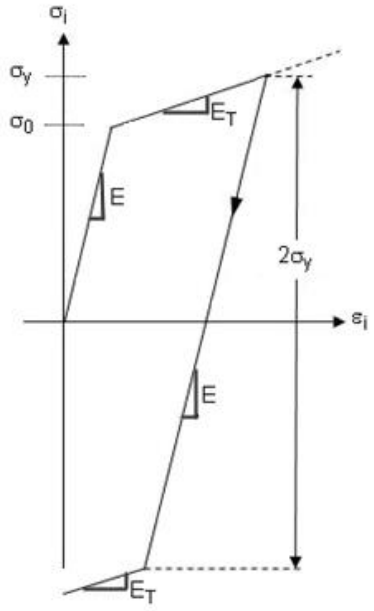

Figure 4.7 Stress vs. Total Strain for Bilinear Isotropic Hardening

The behaviour of *multilinear isotropic hardening* is similar to bilinear isotropic hardening except that a multilinear stress versus total or plastic strain curve is used instead of a bilinear curve.

The multilinear hardening behaviour is described by a piece-wise linear stress-total strain curve, starting at the origin and defined by sets of positive stress and strain values, as shown in this figure:

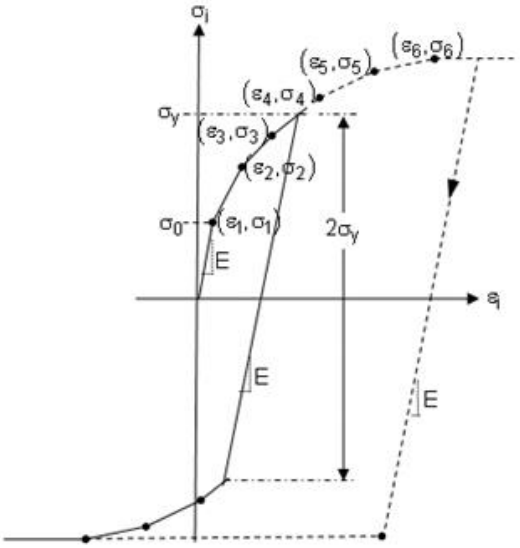

Figure 4.8 Stress vs. Total Strain for Multilinear Isotropic Hardening

The first stress-strain point corresponds to the yield stress. Subsequent points define the elastic plastic response of the material.

4.1.3 Kinematic hardening

During plastic deformation, kinematic hardening causes a shift in the yield surface in stress space. In uniaxial tension, plastic deformation causes the tensile yield stress to increase and the magnitude of the compressive yield stress to decrease. This type of hardening can model the behaviour of materials under either monotonic or cyclic loading and can be used to model phenomena such as the Bauschinger effect and plastic ratcheting.

The yield criterion has the form:

$$F(\bar{\sigma}) - \sigma_y = 0 \quad \textbf{(4.12)}$$

where $F(\bar{\sigma})$ is a scalar function of the relative stress $(\bar{\sigma})$ and σ_y is the yield stress. The relative stress is:

$$\bar{\sigma} = \sigma - \alpha \quad \textbf{(4.13)}$$

where the backstress α is the shift in the position of the yield surface in stress space and evolves during plastic deformation.

Three general classes of kinematic hardening models are available: bilinear, multilinear and nonlinear . Each of the hardening models assumes a von Mises yield criterion and includes an associated flow rule.

The backstress tensor for bilinear kinematic hardening evolves so that the effective stress versus effective strain curve is bilinear. The initial slope of the curve is the elastic modulus of the material and beyond the user specified initial yield stress σ_0, plastic strain develops and the back stress evolves so that stress versus total strain continues along a line with slope defined by the user specified tangent modulus E_T. For uniaxial tension followed by uniaxial compression, the magnitude of the compressive yield stress decreases as the tensile yield stress increases so that the magnitude of the elastic range is always $2\sigma_0$, as shown in this figure:

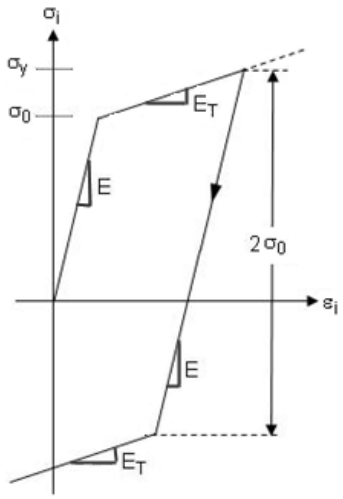

Figure 4.9 Stress vs. Total Strain for Bilinear Kinematic Hardening

The backstress is proportional to the shift strain ε^{sh}:

$$\alpha = 2G\varepsilon^{sh} \quad \textbf{(4.14)}$$

Where G is the elastic shear modulus and the shift strain is numerically integrated from the incremental shift strain which is proportional to the incremental plastic strain:

$$d\varepsilon^{pl} = \frac{C}{2G} d\varepsilon^{pl} \quad \textbf{(4.15)}$$

Where $C = \frac{2}{3}\frac{EE_T}{E-E_T}$ and E is Young's Modulus and E_T is the user-defined tangent modulus. The incremental plastic strain is defined by the associated flow rule for the von Mises with the stress given by the relative stress $\bar{\sigma}$.

The backstress tensor for multilinear kinematic hardening evolves so that the effective stress versus effective strain curve is multilinear with each of the linear segments defined by a set of user input stress-strain points, as shown in this figure:

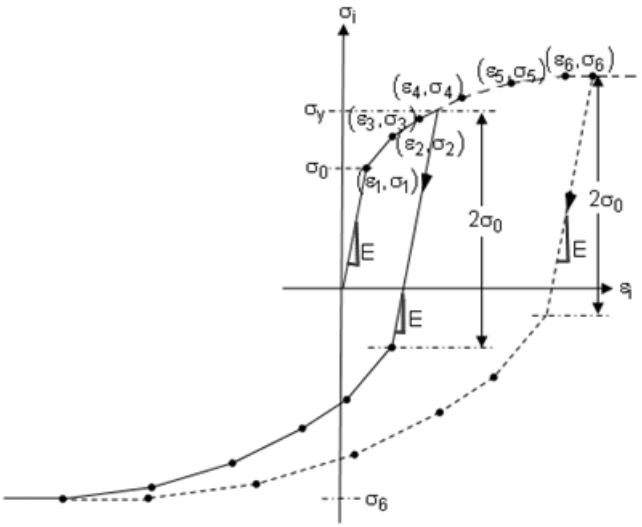

Figure 4.10 Stress vs. Total Strain for Multilinear Kinematic Hardening

The model formulation is the sublayer or overlay model of Besselling and Owen, Prakash and Zienkiewicz in which the material is assumed to be composed of a number of sublayers or subvolumes, all subjected to the same total strain. The number of subvolumes is the same as the number of input stress-strain points, and the overall behaviour is weighted for each subvolume where the weight is given by:

$$w_k = \frac{E - E_{TK}}{E - \frac{1-2\nu}{3} E_{TK}} - \sum_{i=1}^{k-1} w_i \quad \textbf{(4.16)}$$

Where E_{TK} is the tangent modulus for segment of the stress-strain curve. The behaviour of each subvolume is elastic-perfectly plastic, with the uniaxial yield stress for each subvolume given by:

$$\sigma_{yk} = \frac{1}{2(1+\nu)}\left(3E_{\epsilon_k} - (1-2\nu)\sigma_k\right) \quad \textbf{(4.17)}$$

Where $(\epsilon_k . \sigma_k)$ is the input stress-strain point for subvolume k.

The yield surface is the von Mises surface, and each subvolume yields at an equivalent stress equal to the subvolume uniaxial yield stress. The subvolumes undergo kinematic hardening with an associated flow rule and the plastic strain increment for each subvolume is the same as that for bilinear kinematic hardening. The total plastic strain is given by:

$$d\epsilon^{pl} = \sum_{i=1}^{N_{SV}} w_i \, d\epsilon_i^{pl} \quad \textbf{(4.18)}$$

Where N_{SV} is the number of subvolumes and $d\epsilon_i^{pl}$ is the subvolume plastic strain increment.

4.1.4 Cyclic plasticity models

Let's consider a monotonic loading, the yield surface only expands/contracts (isotropic hardening/softening). In cyclic loading, the yield surface changes in stress space (kinematic hardening/softening) and undergoes expansion/contraction (isotopic hardening/softening).There are also models which combine isotropic and kinematic hardening, this is appropriate for modelling of plastic-deformation-related damage in reactor steel due to cyclic loading. Within an individual cycle, the kinematic hardening is the dominant plastic deformation process, in which the material yield depends on the accumulated plastic strain associated with that particular cycle.

However, most of this intra-cycle hardening can be recovered during a stress reversal, leading to a dynamic recovery or memory effect (Bauschinger effect). However, over multiple fatigue cycles (inter-cycle behaviour), the material also hardens or softens due to remnant intra-cycle plastic deformation, which leads to the expansion/contraction of the yield surface.

This inter-cycle expansion/contraction of the yield surface is referred to as the "isotropic hardening component" in the cyclic plasticity model. The material hardening in reactor components can be modelled through well-established techniques, such as those proposed by Chaboche.

Chaboche kinematic hardening model was considered with Von Mises yield criteria. The Von Mises yield criteria can be expressed as:

$$f(\sigma - \alpha, k) = \sqrt{(s-a)\cdot(s-a)} - k = 0 \tag{4.19}$$

where **s** is deviatoric stress tensor, **a** is deviatoric backstress tensor and **k** is the size of yield surface which is constant in the kinematic hardening models. The plastic strain increments in the direction of the gradient of the yield surface were:

$$d\epsilon^p = d\lambda \frac{\partial f}{\partial \sigma} \tag{4.20}$$

Where $d\epsilon^p$ is plastic strain rate, $d\lambda$ is the plastic multiplier and f is the yield function.

Armstrong and Frederick added a nonlinear term to the hardening rule of Prager.

Prager introduced the simplest kinematic hardening model. Prager's model is expressed in the following equation:

$$d\alpha = \frac{2}{3} C\ d\epsilon^p \tag{4.21}$$

The additional term to the Prager model was proportional to the norm of plastic strain rate. The model of Armstrong is indicated in the following equation:

$$d\alpha = \frac{2}{3} C\ d\epsilon^p - \gamma \alpha dp \tag{4.22}$$

This model has a few constants and cannot predict the ratcheting accurately. Chaboche then proposed a new kinematic hardening rule with more constants in order to improve the results of Armstrong's model. The model was:

$$d\alpha_i = \frac{2}{3} C_i\ d\epsilon^p - \gamma_i \alpha_i dp \tag{4.23}$$

Where C_i and $\gamma_i$are material parameters and dp is the accumulated plastic strain rate which was defined as:

$$dp = \left(\frac{2}{3} d\epsilon^p : \frac{2}{3} d\epsilon^p\right)^{\frac{1}{2}} \tag{4.24}$$

Solving the Chaboche's model resulted in the following relations [2]:

$$\alpha_{ix} = \frac{2}{3}\frac{C_i}{\gamma_i} + \left(\alpha_{ix0} - \frac{2}{3}\frac{C_i}{\gamma_i}\right) \exp\left[-\gamma_i\left(\epsilon_x^p - \epsilon_{x0}^p\right)\right], \quad d\epsilon_x^p \geq 0 \tag{4.25}$$

$$\alpha_{ix} = \frac{2}{3}\frac{C_i}{\gamma_i} + \left(\alpha_{ix0} + \frac{2}{3}\frac{C_i}{\gamma_i}\right) \exp\left[\gamma_i\left(\epsilon_x^p - \epsilon_{x0}^p\right)\right], \quad d\epsilon_x^p < 0$$

This can also be expressed as:

$$\Delta\epsilon_x^p = -\frac{1}{\gamma} \ln\left(\frac{\alpha_{ixn} - \frac{2C_i}{3\gamma_i}}{\alpha_{ixp} - \frac{2C_i}{3\gamma_i}}\right) \qquad d\epsilon_x^p \geq 0 \tag{4.26}$$

$$\Delta\epsilon_x^p = \frac{1}{\gamma} \ln\left(\frac{\alpha_{ixn} + \frac{2C_i}{3\gamma_i}}{\alpha_{ixp} + \frac{2C_i}{3\gamma_i}}\right) \qquad d\epsilon_x^p < 0$$

Where α_{ip} and α_{in} are the maximum and minimum values of backstress components during tensile and compressive loading respectively. By dividing a loading cycle to positive and

negative phases with both at plastic region and include the plastic strain, $d\epsilon_x^p > 0$ for positive phase and $d\epsilon_x^p < 0$ for negative phase, the following relations can be reached:

$$\alpha_{xp} = \sum \alpha_{ixp} = \frac{2}{3}(\sigma_x - \sigma_0) \qquad d\epsilon_x^p \geq 0$$
$$\alpha_{xp} = \sum \alpha_{ixp} = \frac{2}{3}(\sigma_x + \sigma_0) \qquad d\epsilon_x^p < 0 \tag{4.27}$$

Combining the equations (4.25)and (4.27) will lead to:

$$\alpha_{xp} = \sum [\frac{2}{3}\frac{C_i}{\gamma_i} + \left(\alpha_{ixn} - \frac{2}{3}\frac{C_i}{\gamma_i}\right)\exp\left[-\gamma_i(\Delta\epsilon_x^p)\right]], \quad d\epsilon_x^p \geq 0$$
$$\alpha_{xp} = \sum [-\frac{2}{3}\frac{C_i}{\gamma_i} + \left(\alpha_{ixn} + \frac{2}{3}\frac{C_i}{\gamma_i}\right)\exp\left[\gamma_i(\Delta\epsilon_x^p)\right]], \quad d\epsilon_x^p < 0 \tag{4.28}$$

The last equations can be used to calibrate the material constants C_i and γ_i of the decomposed hardening rule. A set of equations can be attained by using know states of (α_{ixn} , α_{ixp} , $\Delta\epsilon_x^p$).

Chaboche's model is implemented in many computer software, which allow to define the material constants using "material curve-fitting". Curve fitting requires experimental test data. To use curve fitting with plasticity, the only experimental data supported is uniaxial test data.

4.2 FEM Model

In this paragraph it's proposed a prediction model of behaviour of the devices in order to compare them with the experimental results.

The analysed devices are the SLB 30_3, SLB 40_3, SLB 40_5, SLB 50_3 and SLB 50_5.

In order to perform it there are used two software: "*AutoCAD 3D*" and "*Ansys Workbench*". The firs is used to define the geometry, the second to realize the mesh of numerical model and numerical analysis, in particular, monotonic test and cyclic test.

The adopted plasticity model, to perform nonlinear analysis, is *Chaboche model* which combines the isotropic and kinematic hardening. The material parameters are C1=14000 and $\gamma_1 = 40$, equal for the all devices. These two parameters are obtained proceeding by trial and error.

The plasticity model is based on the von Mises yield criterion.

4.2.1 Ansys Workbench

Ansys Mechanical software is comprehensive FEA analysis (finite element) tool for structural analysis, including linear, nonlinear and dynamic studies. The engineering simulation product provides a complete set of elements behaviour material models and equation solvers for a wide range of mechanical design problems. In addition, ANSYS Mechanical offers thermal analysis and coupled-physics capabilities involving acoustic, piezoelectric, thermal-structural and thermos-electric analysis.

Existing native CAD geometry can be used directly with ANSYS structural analysis software with no translation, no IGES and no intermediate geometry formats. ANSYS has provided native bidirectional integration with the most popular CAD systems for more than a decade. Integration directly into the CAD menu bar makes it very simple to launch world-class simulation directly from a CAD system. Since the ANSYS geometry import mechanism is common to all CAD systems, the user has the flexibility to work within a single common simulation environment while using multiple CAD packages.

ANSYS provides a wide range of highly robust automated meshing tools, from tetrahedral meshes to pure hexahedral meshes, inflation layers and high-quality shell meshes. Mesh settings like surface or edge sizing, sphere of influence, defeating tolerances and more can be set by the user.

Once the geometry has been imported, ANSYS structural software tools automatically detect and perform setup for contacts or joints between parts of an assembly. The contact settings and options can be modified, and additional manual contact definitions can be added. Joints for

flexible/rigid dynamics are automatically detected. Each contact or joint is easily identified using the graphical tools provided in the environment.

Furthermore, it is vital to understand and accurately characterize material behaviour while designing or analysing an engineering application. ANSYS provides a vast library of mathematical material models that aid users in simulating various kinds of material behaviour, such as elasticity, visco-elasticity, plasticity, viscoplasticity, cast iron plasticity, creep, hyperelasticity, gaskets and anisotropy. These constitutive models can be used to simulate various kinds of materials: metals, rubber, plastics, glass, foam, concrete, bio-tissues and special alloys. In addition, to aid in finding parameters for these materials models, ANSYS provides a set of curve-fitting tools.

Material Models	Other Models
Isotropic/orthotropic elasticity	Cast iron plasticity
Multilinear elasticity	Drucker–Prager
Hyperelasticity	Shape memory alloy
Anisotropic hyperelasticity	Swelling material model
Bergstrom–Boyce	Gasket material
Mullins effect	Concrete
Plasticity	Gurson damage
Viscoelasticity	USERMAT
Viscoplasticity	
Creep	

ANSYS structural analysis software offers a large library of out-of-the box equation solvers. The library contains the sparse direct solver, preconditioned conjugate gradient (PCG) iterative solver, Jacobi conjugate gradient (JCG) solution and more. In addition, the distributed versions of PCG, JCG, and sparse solvers are available for use in large-scale computing via parallel processing. By combining our parallel algorithms with the power of GPUs, you can further reduce the solution time required for large models.

ANSYS FEA software provides a comprehensive set of post-processing tools to display results on models as contours or vector plots to provide summaries of the results (like min/max values and locations). Powerful and intuitive slicing techniques allow the user to get more detailed results over given parts of geometries. All results can be exported as text data or to a

spreadsheet for further calculations. Animations are provided for static cases as well as for nonlinear or transient histories. Any result or boundary condition can be used to create customized charts.

Customization capabilities through user elements, user materials and scripting using ANSYS Parametric Design Language (APDL) provide flexibility and extend the capability of applications for structural analysis solutions.

APDL is the foundation for accessing sophisticated features of the structural solver. In addition, engineers can use APDL to automate common tasks, build their own parametric models, perform design optimization, construct adaptive meshing, etc., as it offers many convenient features such as parameters, macros, branching, looping, and repeating and array parameters that can be used in day-to-day analyses.

4.3 Material

Tensile test on the material has been made in the laboratory of University "Federico II" of Naples , in order to determine the stress-strain $\sigma - \epsilon$ curve. The specimen is subjected to a controlled uniaxial tensile force increasing in time, generated by a tensile universal testing machine; displacements are evaluated measuring at each step the extension ΔL caused in the sample through the employment of extensometers or strain gauges. It is possible to obtain the stress-deformation σ-ε relation dividing respectively the applied force F by the initial specimen cross section area A_0 and the elongation ΔL by the initial specimen length L_0:

$$\sigma = \frac{F}{A_0} \qquad \epsilon = \frac{\Delta L}{L_0} = \frac{L_0 - L}{L_0} \tag{4.29}$$

The value of the rupture deformation depends on the initial length of the test specimen, thus it is standardized in different countries.

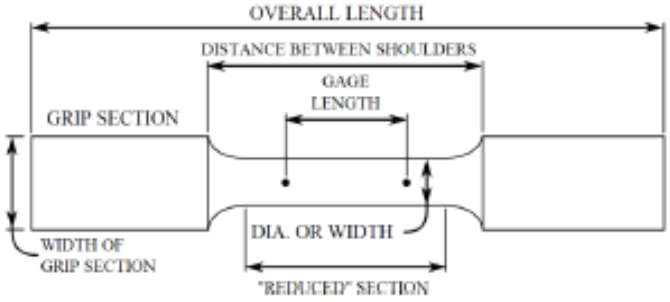

Figure 4.11 Tensile test specimen shape

Because of this particular shape the sample is also called "dog-bone specimen". Subjected to the increasing tensile force it undergoes continuing elongation until in the middle cross section the necking phenomenon is reached, thus causing the consequent tension failure.

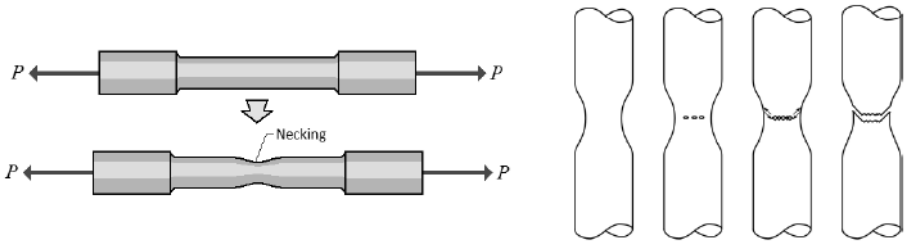

Figure 4.12 Necking phenomenon and tension rupture

Properties that are directly measured through a tensile test are ultimate tensile strength, maximum elongation and reduction in area. From these measurements the following properties can also be determined: Young's modulus, Poisson's ratio, yield strength, and strain-hardening characteristics.

The typical tension-deformation plot characterizing mild steel is depicted in Figure 4.13. It shows an initial elastic trend (1) continuing until yielding (2) is reached; during its excursion in the plastic branch the material keep undergoing deformation for a constant value of the force. In correspondence of a certain deformation level ϵ_h the hardening branch begins: the material can withstand further load for increasing values of deformation. Finally, after the ultimate tensile strength f_u is gained the material's strength starts decreasing until rupture, in correspondence of the deformation ϵ_t.

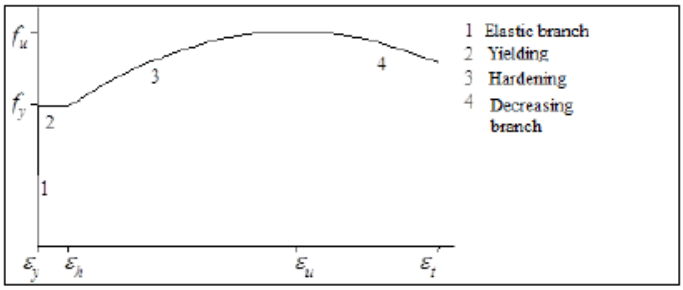

Figure 4.13 Mild steel tension-deformation plot

Uniaxial tensile testing is the most commonly used for obtaining the mechanical characteristics of isotropic materials.

In order to estimate mechanical characteristics of the structural steel composing the shear link energy dissipation devices, tensile test will be performed on specimen tests derived from the same plate that will be subjected to the milling process directed to realize the dissipators.

The result of specimen test is shown in the following table:

CHARACTERISTICS	Test specimen
	Structural steel plate
Cross section WxT [mm]	40x19
Calibrated length G [mm]	50
Cross section Area [mm^2]	760
Yielding force [kN]	259,52
Maximum force [kN]	340,34
Yielding strenght [MPa]	341,47
Maximum strenght [Mpa]	447,82

Table 4.1 tension test: characteristics and results

It is necessary remember the difference between conventional values and real (or natural) values, that is applicable to the values which derived from tensile test.

For the conventional tension-deformation curve, the variables are defined like in equations (4.29).The real values of tension and unitary deformation can be obtained from the expressions:

$$\sigma_r = \frac{F}{A} \qquad \textbf{(4.30)}$$

$$\epsilon = \int_{L_0}^{L} \frac{dL}{L} = ln(1+\epsilon) \tag{4.31}$$

Where A is the real section of steel under the load.

In order to obtain the real values of tension, from the conventional values, it's assumed that the volume of steel sample doesn't change during the plastic deformation, it means:

$$AL = A_0 L_0 \tag{4.32}$$

Imagine that the neck, which is a small zone with reduced cross area, assumes a parabolic profile, so the new area A_1 is smaller than the area A obtained supposing constant profile during the deformation.

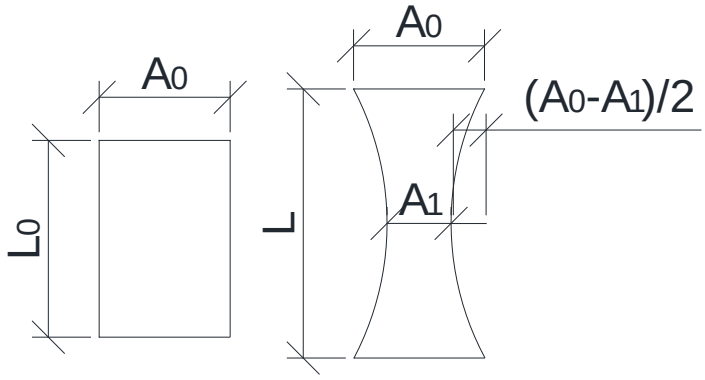

Figure 4.14 Undeformed and deformed configuration

From the equation (4.32), substituting the value of A_1, comes out:

$$\frac{A_0 L_o}{L} = A_0 - \frac{2}{3}\frac{(A_0 - A_1)}{2} \times 2$$

$$\frac{A_0 L_o}{L} = A_0 - \frac{2}{3}A_0 + \frac{2}{3}A_1 \tag{4.33}$$

$$\frac{A_0 L_o}{L} = \frac{A_0}{3} + \frac{2}{3} A_1$$

Multiplying for $\frac{3}{2}$ and highlighting A_1:

$$A_1 = \frac{3}{2} A_0 \frac{L_0}{L} \frac{A_0}{2} - \frac{A_0}{2} \quad \textbf{(4.34)}$$

Substituting the (4.34) in the equation (4.30), it comes out:

$$\sigma_r = \frac{F}{A_1} = \frac{2F}{\frac{3}{2} A_0 \frac{L_0}{L} \frac{A_0}{2} - \frac{A_0}{2}} = \frac{2F}{A_0 (3 \frac{L_0}{L} - 1)} \quad \textbf{(4.35)}$$

From the equation (4.29) derives:

$$\frac{L_0}{L} = \frac{1}{1 + \epsilon} \quad (4.36)$$

Because by Taylor series, if ϵ is a small number it can establish that:

$$\frac{1}{1 + \epsilon} = 1 - \epsilon \quad \textbf{(4.37)}$$

Focusing on the denominator of the equation (4.35), considering (4.36) and (4.37):

$$\left(3 \frac{L_0}{L} - 1\right) = \frac{3}{1 + \epsilon} - 1 = 3(1 - \epsilon) - 1 = 2 - 3\epsilon \quad (4.38)$$

In the end, the real tension can be assumed as:

$$\sigma_r = \frac{2F}{A_0(3\frac{L_0}{L} - 1)} = \frac{2\sigma}{(\frac{3}{1+\epsilon} - 1)} \cong \frac{\sigma}{(1 - 1{,}5\epsilon)} \quad \textbf{(4.39)}$$

The (4.39) it is called Bozzo's Formula.

The following graph shows the curve conventional tension-stress and real-tension-stress, implemented into the Ansys Workbench.

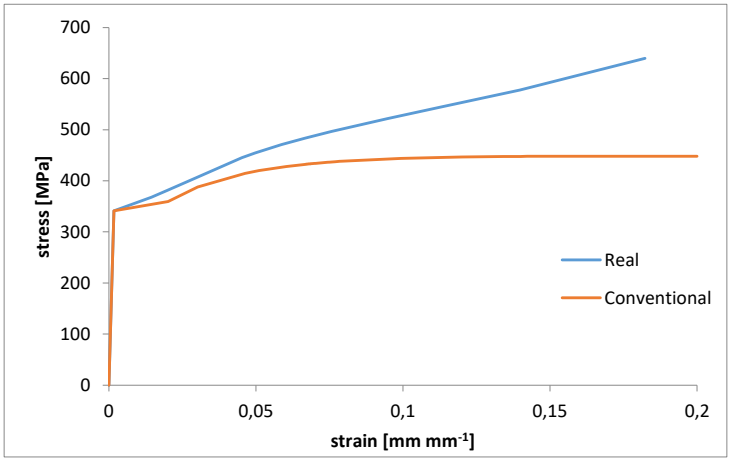

Figure 4.15 Constitutive law implemented into Ansys

The mechanical characteristics of the structural steel are reassumed in the Table 4.2:

Steel	E [Mpa]	G [Mpa]	σ_y [Mpa]	σ_u [Mpa]	ε_u (%)
A36	2,00E+05	7,93E+04	250	400-550	20

Table 4.2 Mechanical characteristics of structural steel

Where

E is Young's modulus

G is shear modulus

σ_y is yielding tensile strength

σ_u is ultimate tensile strength

ϵ_u is elongation at break

4.4 Geometry of Bozzo Shear Link

The geometry of devices is realized with the program AutoCAD 3D, and subsequently loaded into Ansys Workbench.

The geometry properties are equal to the real geometry properties, they are described in the previous chapter.

The following figures show the numerical model of Bozzo Shear Link and its meshing.

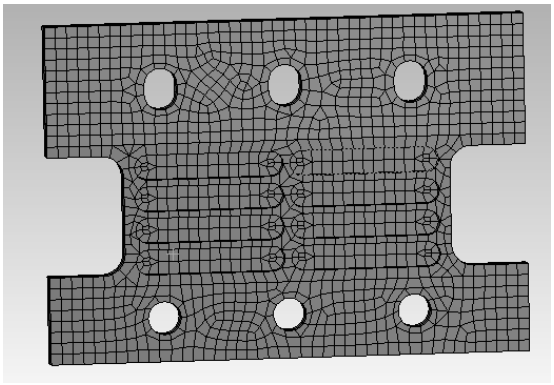

Figure 4.16 Meshing of SLB 30_3

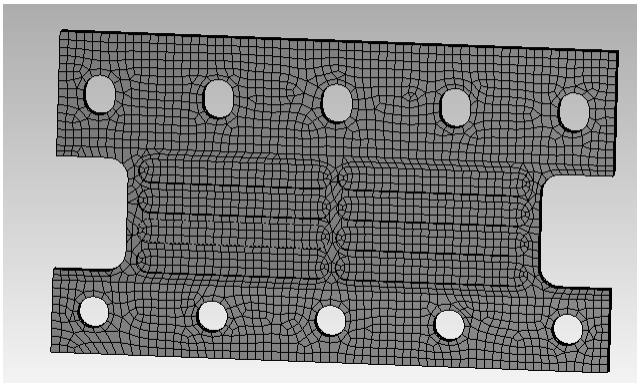

Figure 4.17 Meshing of SLB 40_3

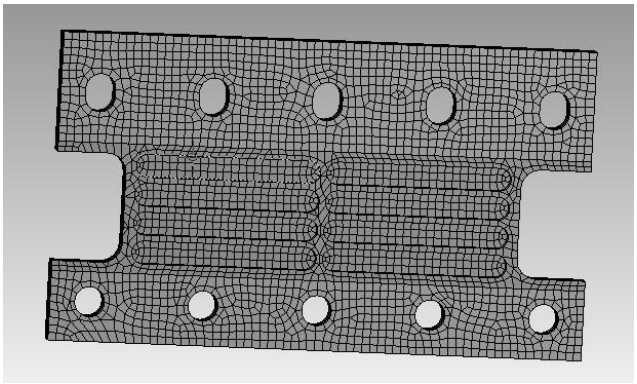

Figure 4.18 Meshing of SLB 40_5

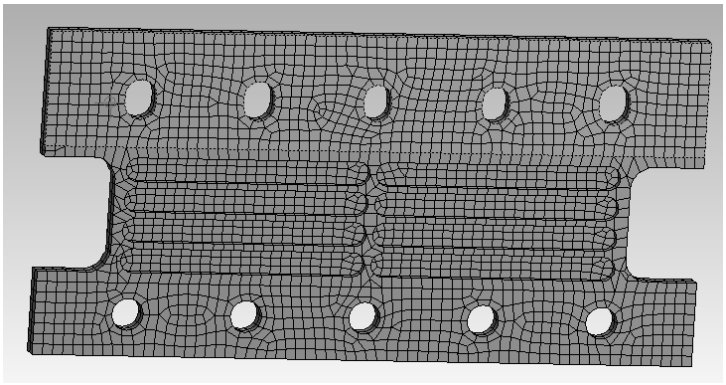

Figure 4.19 Meshing of SLB 50_3

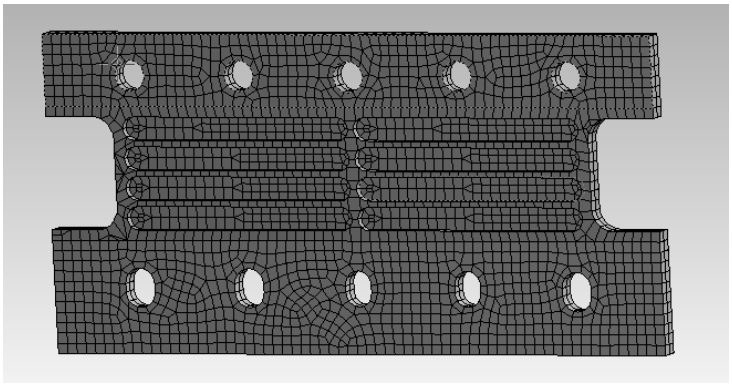

Figure 4.20 Meshing of SLB 50_5

4.5 Influence of meshing for Bozzo Shear Link

Meshing is an integral part of the computer-aided engineering simulation process. It in a discretization of body into a sufficient amount of mesh elements

The mesh influences the accuracy, convergence and speed of the solution. The Ansys Workbench program allows to choose different kind of meshing for 3D bodies. In this specific situation it is chosen the Hex Dominant Method, where a free hex dominant mesh is created. This option is recommended for bodies that cannot be swept. The mesh contains a combination of tetrahedron and pyramid cells with majority of cell being of hex type. Hex dominant meshing reduced element count.

The element size of meshing is should ensure accurate results, smaller is the size, greater is the density.

The density of the mesh is required to be sufficiently high in order to capture all the features but on the same note, it should not be so high that it captures unnecessary details, thus burdening the CPU and wasting more time.

For different values of size element there are different numbers of nodes and elements, which correspond different quality of elements. The mesh metric graph shows the distribution of the element quality. For a good quality the histograms should be closer to 1.

The goal is to find the size element for which the element quality is closed to 1 and the number of elements and nodes is not very high.

Three different values of size element have been tested, in order to evaluate the error entity which is committed using greater value of size element. These are 8 mm, 15 mm and 20 mm.

The following table shows the number of nodes and elements for each size element:

	Numbers	
	Nodes	**Element**
8 mm	40033	8160
15 mm	16482	4418
20 mm	11954	3384

Table 4.3 Number of nodes and elements

The mesh metric for each cases is shown in the imagines below:

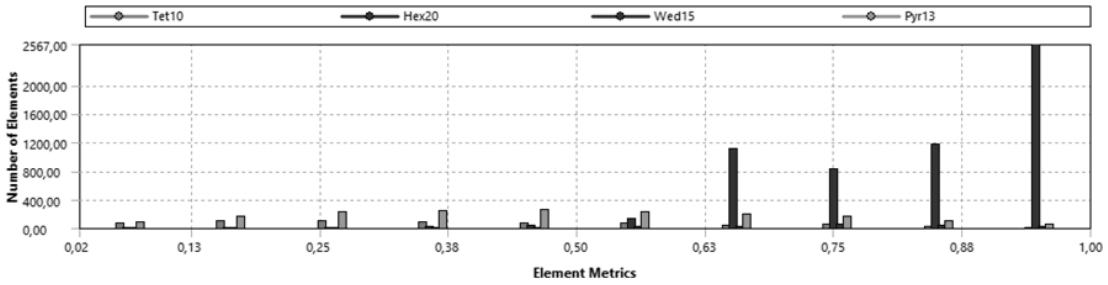

Figure 4.21 Mesh metric for element size of 8 mm

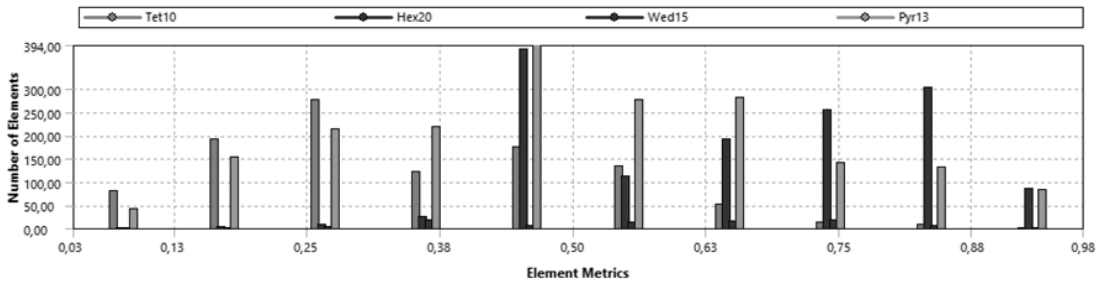

Figure 4.22 Mesh metric for element size of 15 mm

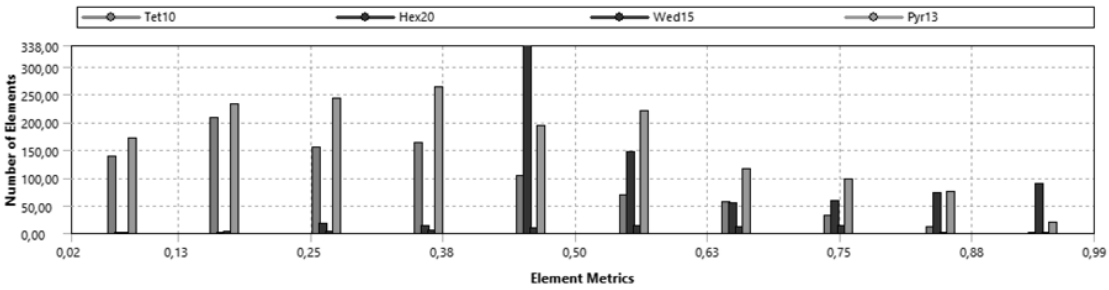

Figure 4.23 Mesh metric for element size of 20 mm

The different colour of the bars represents a different geometry of elements. For the element size 8 mm the element quality is better. However the results in terms of Force-displacement, for the three cases, are very closed, as shows in the following graph:

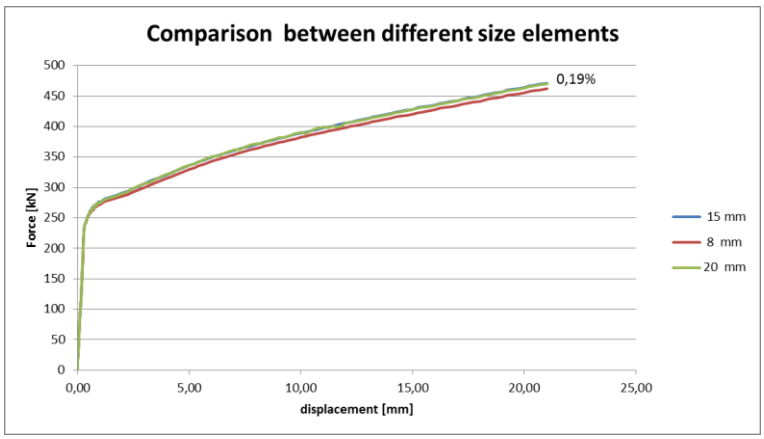

Figure 4.24 Comparison between different element size

The results for element size 15 mm and 20 mm are practically the same.

The numerical analysis are performed using element size of 15 mm for the monotonic case, for the cyclic case is choose element size 8 mm.

4.6 Boundary condition and loading condition

Two kind of boundary condition are performed. In the first condition, called fixed-fixed (FF), the extreme of device with slotted holes, cannot have displacement in y direction, it reproduces the condition in which at the left side of device there is tightening. The second condition, called fixed-nofixed (FNF), displacement in y direction is allowed, in the realty at the left side of device there is not tightening.

In both cases the device is fixed at the top, which represents the right side of the real device. At the bottom the displacement, which is orthogonal to the plane of the device (z direction), is not allowed.

In the Ansys Workbench these conditions are realized imposing the *fixed support* at the holes at the top of numerical model, the *displacement* zero in z direction at the bottom face, in y direction is free for the fixed-nofixed condition or zero for fixed-fixed condition.

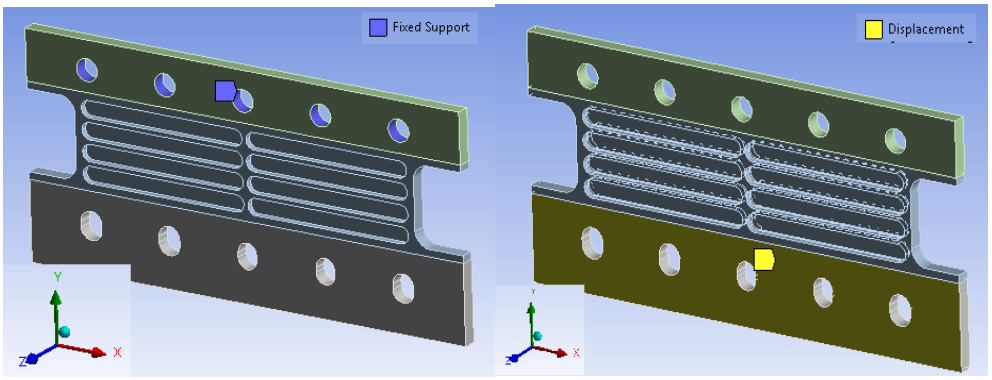

Figure 4.25 Boundary condition imposed to the SLB

The loading condition which is imposed depends on the kind of analysis and it is equal for all the devices.

For the monotonic analysis it is imposed a linear displacement, which increases step by step, it starts from 0 mm to 60 mm.

In order to evaluated the initial stiffness more accurately, the increment of displacement from 0 mm to 1 mm is decomposed into 10 steps, so each steps is 0,1 mm.

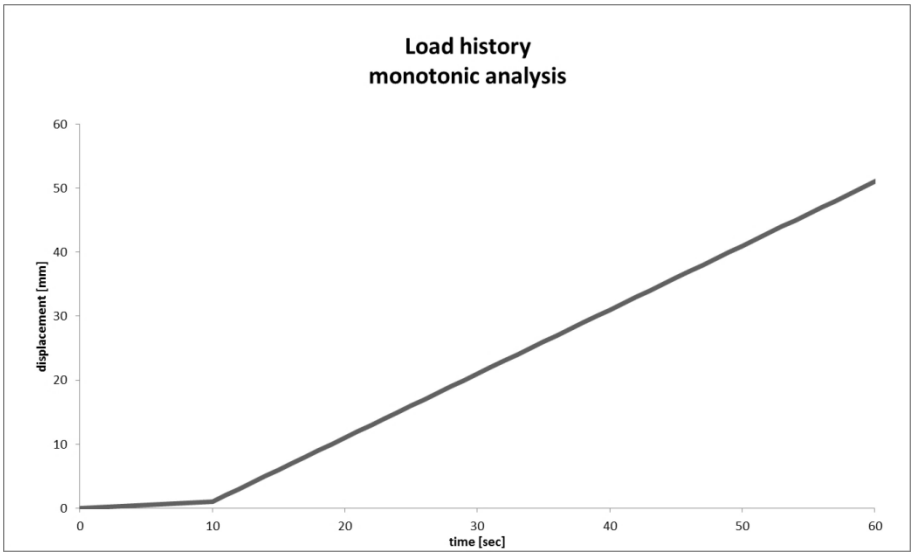

Figure 4.26 Load history for the monotonic analysis

For the cyclic analysis it is imposed a cyclic load history, with maximum displacement value of 20 mm:

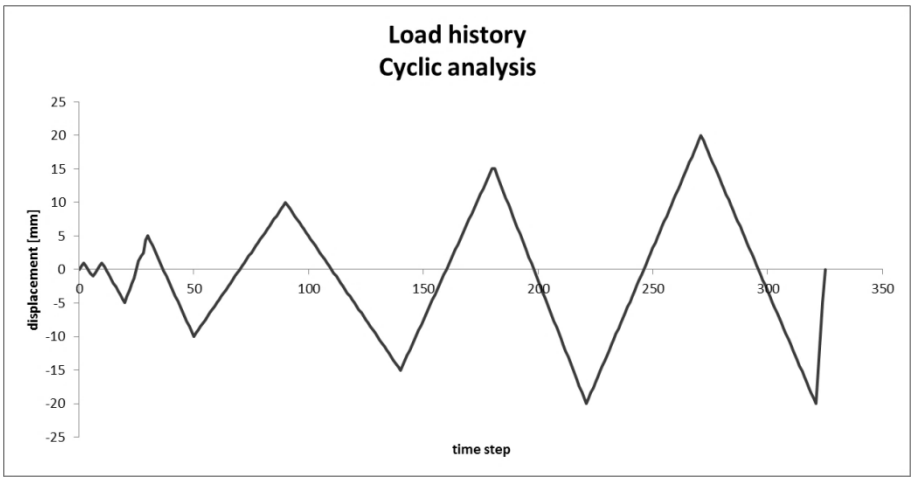

Figure 4.27 Load history for the cyclic analysis

The maximum displacement is imposed 20 mm because it is the value from that usually the degradation of device, under cyclic load, starts.

In both cases the load history is applied at the slotted holes, which are located at bottom face of the device as shown in the following figure:

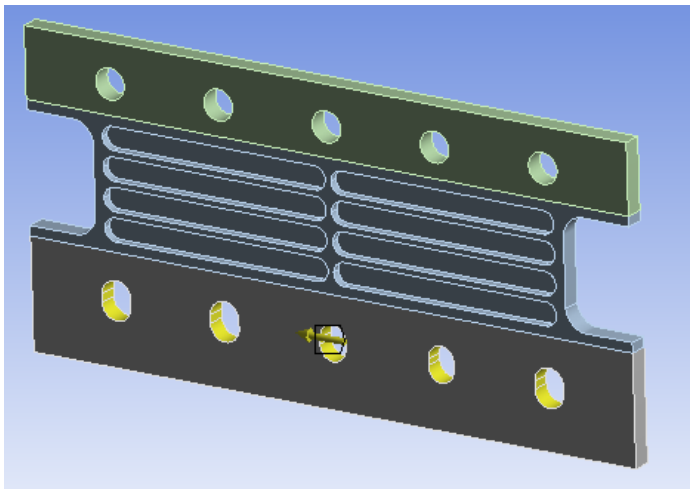

Figure 4.28 Load condition imposed to the SLB

4.7 Results of numerical modelling

The following subparagraphs illustrate the numerical calibration of Bozzo Shear Link devices. This calibration is made possible by the experimental results. In particular the results of the monotonic test and cyclic test are shown. Moreover there are attached the tables which reassume the design parameters.

A qualitative description of failure procedure is described for different kind of boundary conditions.

4.7.1 Monotonic analysis: evaluation of yielding force and maximum force

The numerical responses of Bozzo Shear Link under monotonic load, are reported below.

The horizontal axis represents the displacement, which is an input of program, and the vertical axis represents the Shear Force, which is an output of program. The shear force is obtained as reaction of device.

There is also reported the linearization of the monotonic curve. It is used in order to calibrate the value of Yielding force and its correspondent displacement.

The linearization is obtained by the criterion of equivalence of areas, it consists in to make equal the area under the monotonic curve derived from the numerical analysis with area under the bilinear curve.

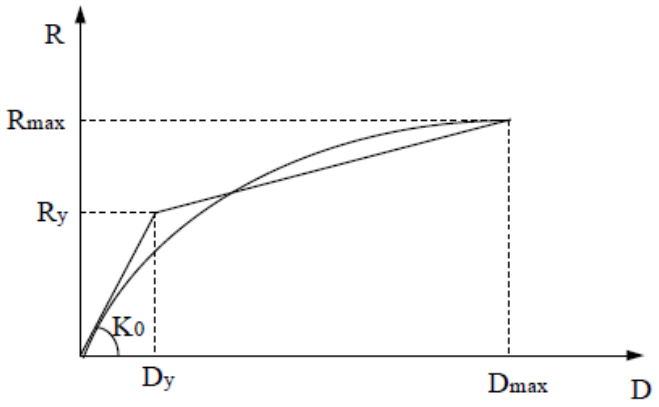

Figure 4.29 Monotonic curve and its linearization

It is necessary to impose the elastic stiffness equal to the elastic stiffness derived from the numerical analysis. The other imposition is the passage of the linearized curve for one point, the chosen point is the maximum experimental displacement under cyclic load of corresponding device. The areas, which are made equal, arrive to this point. In this way the unique unknowns are the yielding force and its displacement. Once linearized curve is obtained, it is also possible to compute the stiffness post yielding, k_2, which is the slope of the section of curve from yielding force to maximum force.

For each device is reproduced the same boundary condition performed in the experimental tests, they are summarised:

- SLB 30_3: fixed-fixed and fixed-nofixed
- SLB 40_3: fixed-fixed
- SLB 40_5: fixed-nofixed
- SLB 50_3: fixed-fixed and fixed-nofixed
- SLB 50_5: fixed-nofixed

The monotonic numerical curve and its correspondent linearization are shown below.

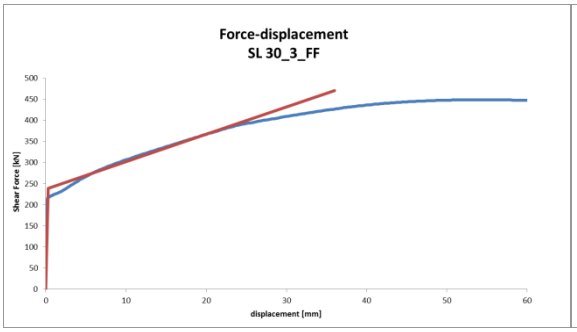

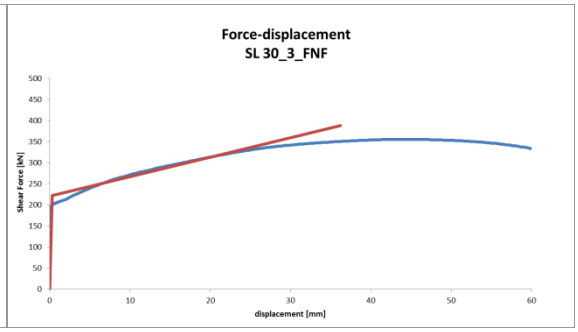

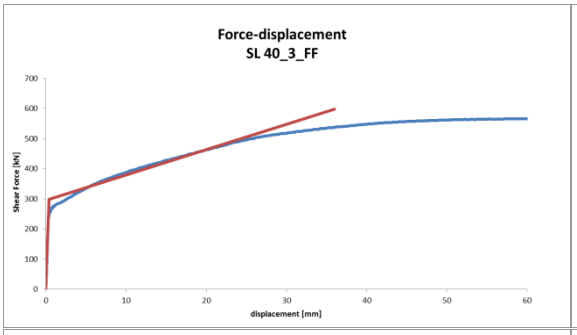

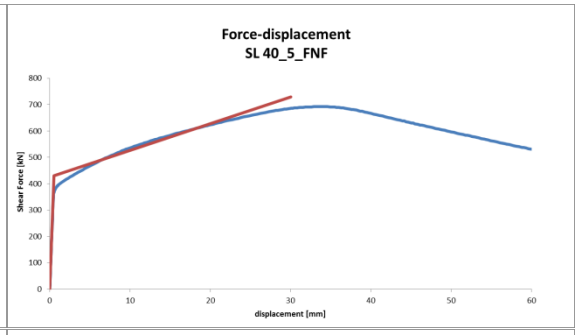

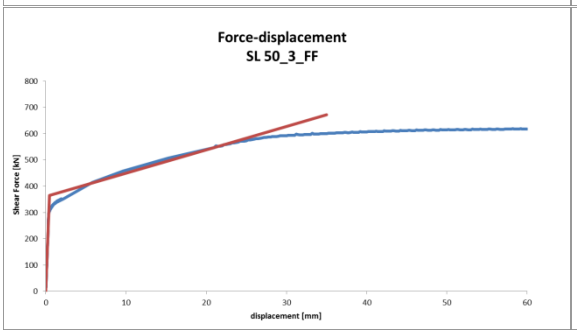

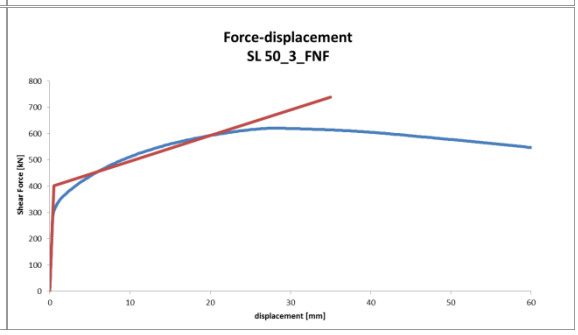

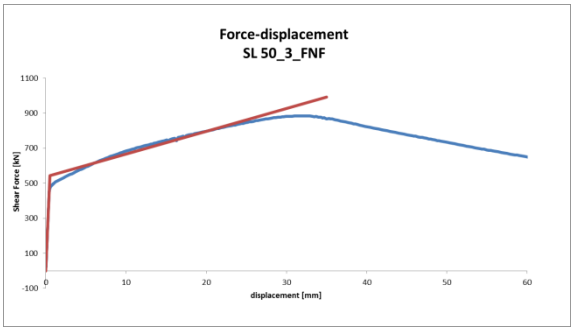

The loss of the resistance, observed in the graphs, is due to the buckling of the device.

The following table summarizes the design parameters of all device, i.e.:

f_y:yielding force given by the curve

d_y: yielding displacement given by the curve

F_y: Yielding force given by the linearization

d_y:yielding displacement given by the linearization

k_{el}: initial elastic stiffness

F_{Max}: maximum force, output of numerical analysis

d_{Max}:maximum displacement output of numerical analysis

k_2: stiffness post yielding

	f_y	d_y	F_y	D_y	k_{el}	F_{max}	d_{max}	k_2	k_2/k_{el}
	[kN]	[mm]	[kN]	[mm]	[kN/mm]	[kN]	[mm]	[kN/mm]	[-]
SL30_3_FF	216,4	0,3	240,0	0,3	798,0	449,0	51,4	6,5	0,0081
SL30_3_FNF	199,4	0,3	221,8	0,3	731,5	355,3	43,7	4,6	0,0063
SL40_3_FF	220,0	0,3	297,8	0,4	772,6	565,7	59,2	8,4	0,0109
SL40_5_FNF	347,7	0,4	431,1	0,5	874,4	702,8	36,4	10,1	0,0115
SL50_3_FF	272,4	0,3	364,7	0,4	842,0	619,0	59,2	8,9	0,0106
SL50_3_FNF	273,9	0,3	401,7	0,5	829,1	620,5	28,1	9,8	0,0118
SL50_5_FNF	459,8	0,4	544,0	0,5	1061,7	884,0	32,0	13,0	0,0122

It is possible to note that the value of yielding force, F_y which is obtained from the linearization, is greater than the yielding force f_y obtained from the curve. It means that the linearization overestimates the yielding force with an error about 20%.

The value of maximum force is not obtained from the linearized curve because it is overestimation value, so the maximum force comes out from the nonlinear curve.

4.7.2 Cyclic analysis and dissipated energy

The calibration of the numerical model of Bozzo Shear Link has been realized approximating as possible as the numerical hysteretic loop to the real hysteretic loop. In order to realize this, the Chaboche's parameters, which are chosen, are $C_1 = 14000$ and $\gamma_1 = 40$.

For each device the cyclic analysis is performed, all the curves are shown below.

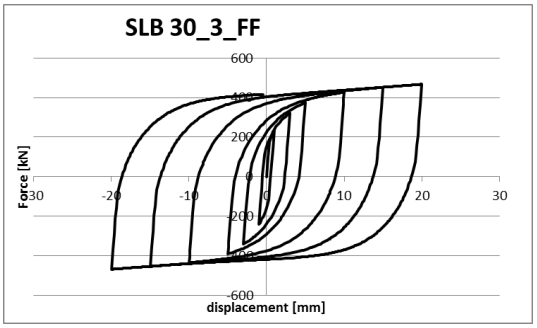

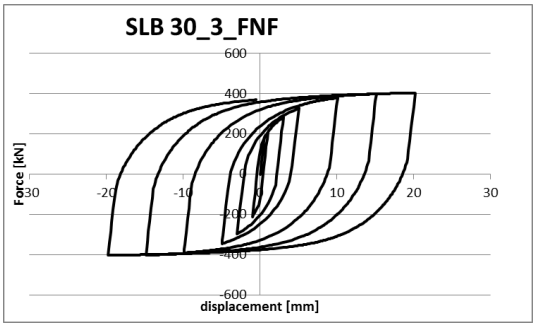

Graph 4-1 SLB 30_3: fixed-fixed condition and fixed-nofixed condition

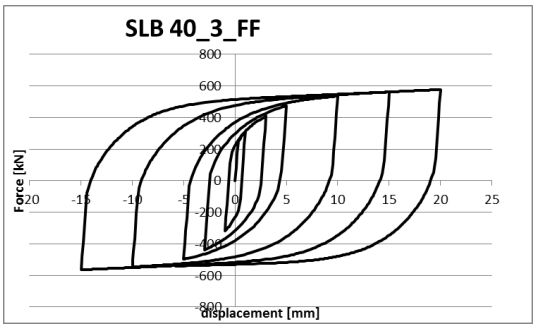

Graph 4-2 SLB 40_3:fixed-fixed condition

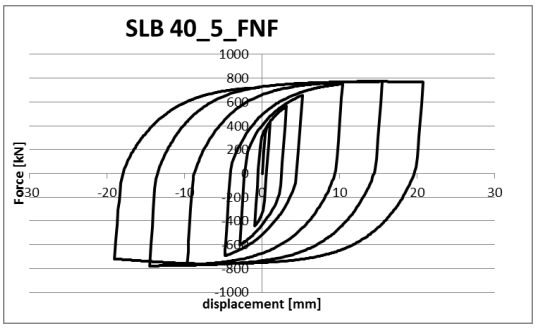

Graph 4-3 SLB 40_5:fixed-nofixed condition

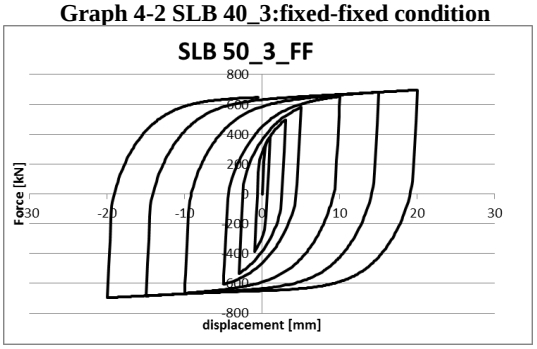

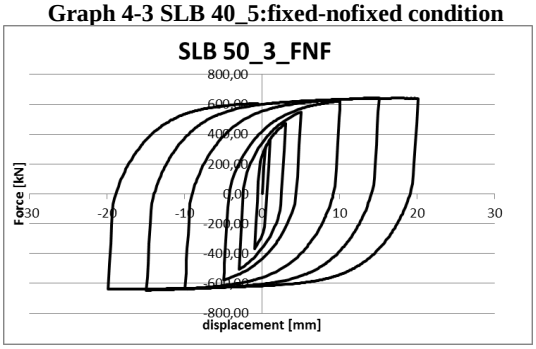

Graph 4-4 SLB 50_3:fixed-fixed condition and fixed-nofixed condition

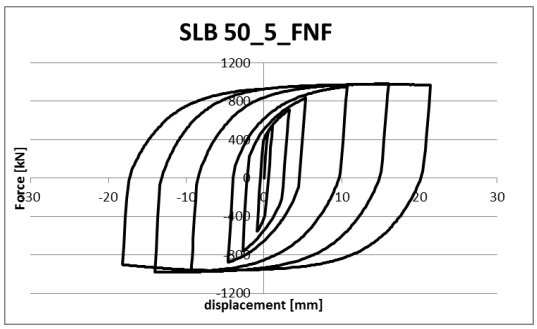

Graph 4-5 SLB 50_5: fixed-nofixed condition

The hysteretic loops are stable and symmetric with respect to the vertical and horizontal axis, for both boundary conditions. The greater loop is obtained for the SLB 50_5_FNF.

The maximum applied displacement is 20 mm because after this displacement the numerical model shows a loss of resistance due to the buckling of the web. The Ansys program does not associate to the damage the formation of the crack.

However it permits a good estimate of reached maximum force and dissipated energy.

As well as the experimental test, for the numerical test the total dissipated energy is evaluated as the sum of dissipated energy and elastic strain energy. It is also calculated the value of equivalent damping ratio, as the equation (3.12). The hysteretic loop, which the parameters are evaluated, is characterized by a maximum displacement of 15 mm, as shown in Figure 4.30.

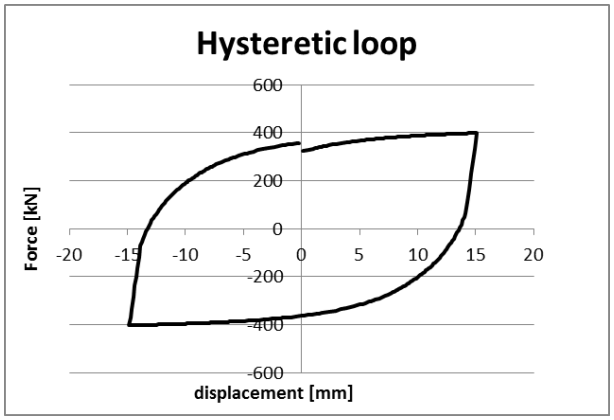

Figure 4.30 Hysteretic loop for which the total dissipated energy is computed

The results are shown in the Table 4.4.

	Ed	Es	Etot	ζ_{eq}
	[KJ]	[KJ]	[KJ]	[-]
SLB 30_3_FF	29,22	4,68	33,91	49,7%
SLB 30_3_FNF	25,14	4,04	29,17	49,6%
SLB 40_3_FF	37,42	5,77	43,20	51,6%
SLB 40_5_FNF	49,96	7,39	57,34	53,8%
SLB 50_3_FF	45,77	6,97	52,74	52,3%
SLB 50_3_FNF	42,49	6,39	48,88	52,9%
SLB 50_5_FNF	63,24	9,26	72,49	54,39%

Table 4.4 Numerical result: dissipated energy and equivalent damping ratio

It is possible to note that the different boundary conditions have not influence on the equivalent damping ratio, in fact the difference is about 1%.

However, the increase of thickness of milled area, from 3 mm to 5 mm, the equivalent damping ratio increases about 3%.

4.7.3 Analysis of post-elastic behaviour of Bozzo Shear Link

In this subparagraph the qualitative develop of failure of device is described.

The failure is assumed as the loss of resistance that is caused by the buckling of web of device. The constitutive law is an output of the program, it is determined by stress-strain point. The last point corresponds to the deformation $\epsilon = 0{,}2$, after this point the law is considered undefined, with increasing strain and constant stress. For this reason the program does not associate to the failure the formation of the crack.

However it is possible to do consideration on the plastic deformations distribution and its entity in order to have an idea where the damage starts and where it spreads.

From the tensile test on the material specimen it is observed that the damage starts for a deformation of 20%, so this value is considered as reference parameter for the beginning of the degradation.

The analysis is centred on the study of plastic deformation distribution and the research of point where the deformation is equal to the 20%.

The distribution of plastic strain is different for the two cases of boundary conditions and it refers to the monotonic load. For the fixed-fixed condition the deformed shape is rigid, the bottom face just translates. For low displacement the plastic deformations affect the web of device, they are distributed at central windows and at the lateral stiffeners, at left side near upper face (fixed restrain) and at right side near bottom face (applied displacement). With the increment of displacement, the plastic deformations increase and it spreads also at lateral windows. It is observed that the deformation of 20% is reached, at the beginning, in the milled area and then in the lateral stiffeners. It means that the degradation affects before the windows and after it interests the lateral stiffeners.

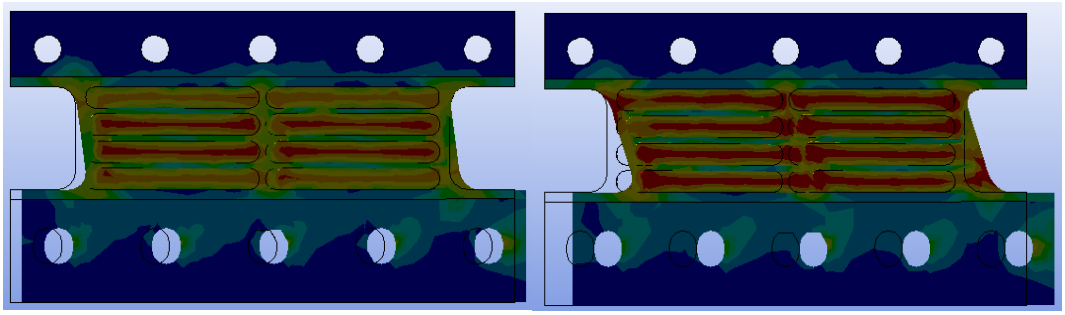

Figure 4.31 Distribution of plastic strain for fixed-fixed condition

When the boundary condition changes, the deformed shape changes too. The fixed-nofixed condition has typical deformed shape of a cantilever: the upper face represents the fixed restrain so its displacement is null, the bottom face is the free extreme, under a imposed displacement it translates and rotates. At the beginning the plastic deformations are concentrated at the lateral stiffeners at the top, near the upper face, and at the central windows. At the maximum force, the plastic deformations spread also at the lateral windows, as shown in the following figure.

It is observed that the deformation of 20% is reached, more or less, at the same time at lateral stiffeners and central windows, it means that the degradation concomitantly affects these zones.

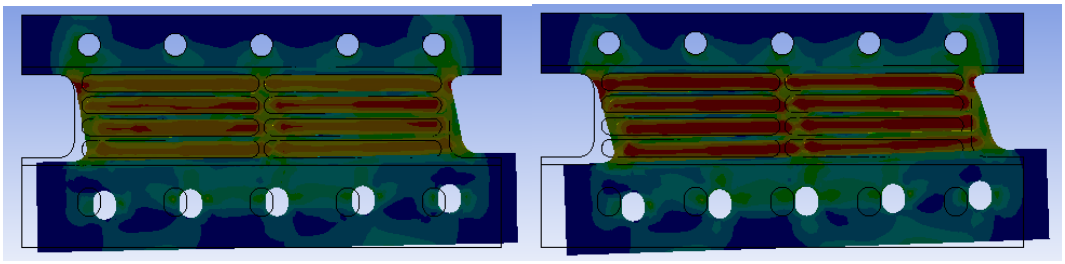

Figure 4.32 Distribution of plastic strain for fixed-nofixed condition

In the following figures the distribution of stress of Von Mises is shown. The figures depict the step of maximum force for each device. It is possible to observe that the distribution is in agreement with the distribution of plastic deformation.

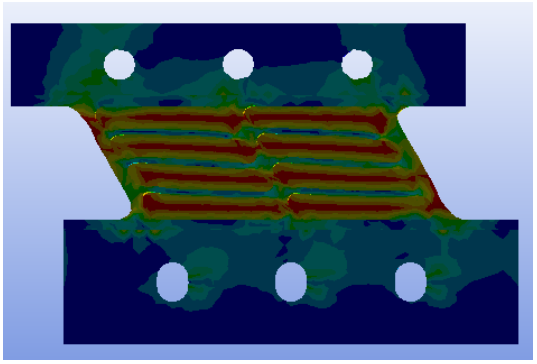

Figure 4.33 SLB 30_3_FF

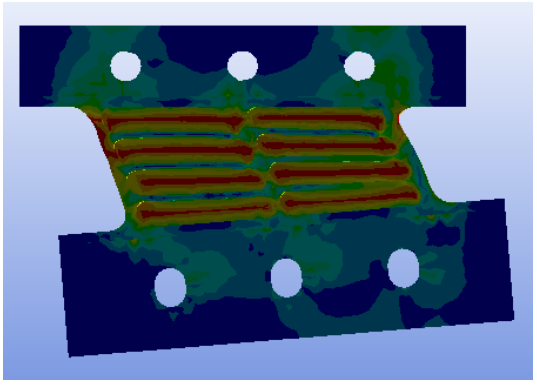

Figure 4.34 SLB30_3_FNF

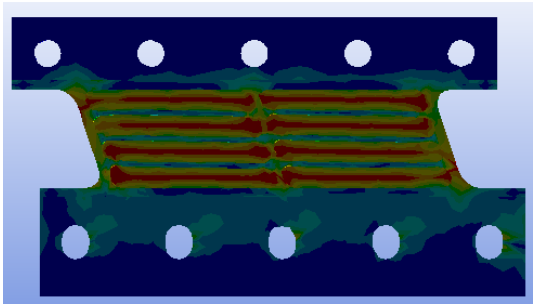

Figure 4.35 SLB 40_3_FF

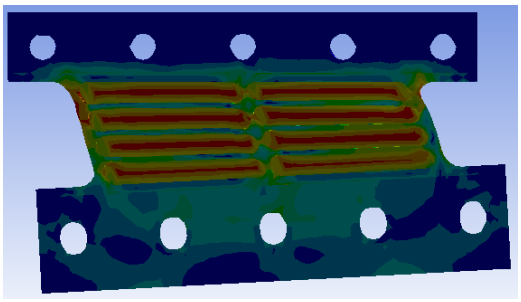

Figure 4.36 SLB 40_5_FNF

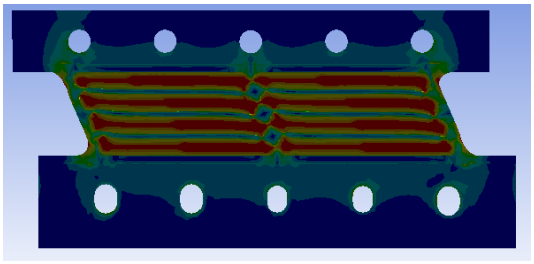

Figure 4.37 SLB 50_3_FF

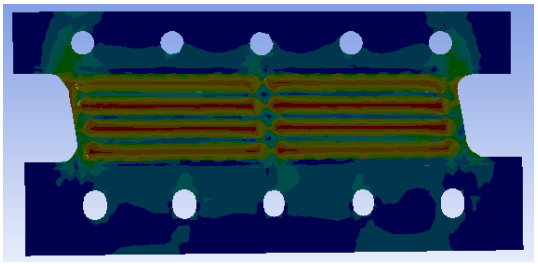

Figure 4.38 SLB 50_3_FNF

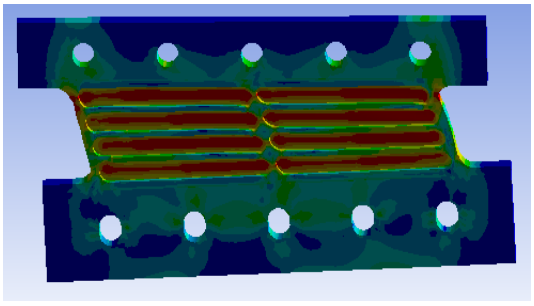

Figure 4.39 SLB 50_5_FNF

The values of the stress, which are evaluated according to the Von Mises criteria, are more or less equal for all devices. The tension distribution is uniform in the milled area.

4.8 Comparison of experimental results and numerical results

The numerical analysis is necessary in order to predict the nonlinear behaviour of Bozzo Shear Link device, used for the seismic design of the structures.

The main goal is to determine the parameters which define the numerical model of device so that the response is as possible as closed to the real behaviour. The best way of proceeding is calibrate the numerical model on the experimental results.

In this paragraph the comparison between experimental results and numerical results is illustrated, highlighting errors due to the numerical approximation.

4.8.1 Monotonic test results

Under the monotonic load it is possible to obtain the values of yielding force and maximum force. The SLB 40_3, the SLB 40_5 and the SLB 50_5 are performed under monotonic load, the others device are tested only under cyclic load. For the first the superposition of the monotonic curve is shown in the following graphs. For all numerical devices, the maximum displacement is imposed 60 mm, as in Figure 4.26.

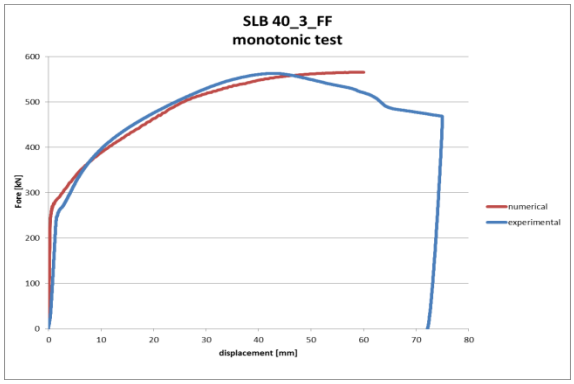

Graph 4-6 SLB 40_3: numerical and experimental monotonic curve

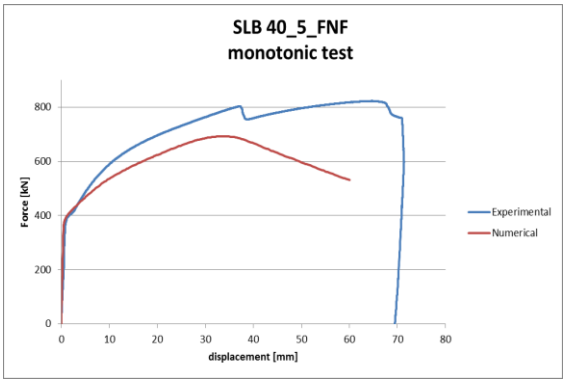

Graph 4-7 SLB 40_5: numerical and experimental monotonic curve

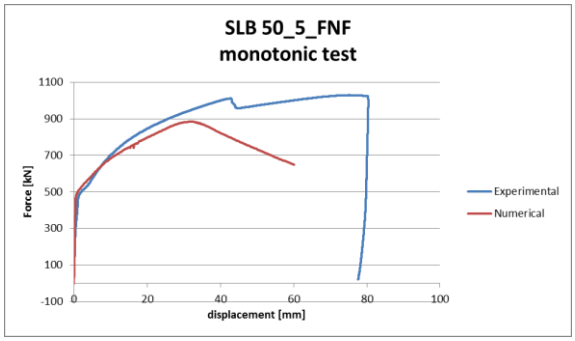

Graph 4-8 SLB 50_5: numerical and experimental monotonic curve

It is possible to note that the numerical yielding force is very closed to the experimental yielding force. However the numerical maximum force is equal to the experimental maximum force in the fixed-fixed condition of SLB 40_3. In the others boundary conditions the maximum force of numerical case is less than the experimental case, about 10%.

In the Graph 4-7 and Graph 4-8 the numerical curves show the loss of resistance, associated to the instability of the web of the dissipator.

In the Table 4.5 are shown the values of yielding force and maximum force for the experimental test and numerical test. The numerical yielding force do not come from the linearization of the monotonic curve. For the SLB 30_3 and SLB 50_3, which are performed only with cyclic test, these values are evaluated from the hysteretic loop.

	F_y			F_{max}		
	[kN]			[kN]		
	Experimental	Numerical	%	Experimental	Numerical	%
SL30_3_FF	137	216	37%	434	449	3%
SL30_3_FNF	208	199	4%	396	355	10%
SL40_3_FF	243	220	9%	563	566	0%
SL40_5_FNF	364	348	5%	804	703	13%
SL50_3_FF	325	272	16%	637	619	3%
SL50_3_FNF	228	274	17%	655	620	5%
SL50_5_FNF	334	460	27%	1011	884	13%

Table 4.5 Yielding force and maximum force: experimental and numerical results

As regard the elastic stiffness, the numerical model overestimates this parameter. In all cases the numerical elastic stiffness is greater than the experimental once at least 50%. The results are given by the table:

	k_{el}		
	[kN/mm]		
	Experimental	Numerical	%
SL30_3_FF	229	798,0	71,3%
SL30_3_FNF	66	731,5	91,0%
SL40_3_FF	163	772,6	78,9%
SL40_5_FNF	433	874,4	50,5%
SL50_3_FF	465	842,0	44,8%
SL50_3_FNF	456	829,1	45,0%
SL50_5_FNF	557	1061,7	47,6%

Table 4.6 Elastic stiffness: experimental and numerical results

The tolerance of the slotted holes, which is recorded in the experimental tests, causes the great difference between the value of experimental elastic stiffness and value of numerical elastic stiffness. The numerical model not reproduces this phenomenon so it returns greater results.

4.8.2 Cyclic test results

From the cyclic test, made in the laboratory, the maximum force, which the device reaches, are obtained. This value is compared with the maximum force, carried out by the numerical analysis.

In the Table 4.7, the results are shown, the third column gives the percentage error of the numerical model.

	F_{max} [kN]		
	Experimental	**Numerical**	**%**
SLB 30_3_FF	434,3	466,91	6,98%
SLB 30_3_FNF	396,2	404,2	1,99%
SLB 40_3_FF	517,0	577,24	10,44%
SLB 40_5_FNF	740,0	776,96	4,76%
SLB 50_3_FF	637,0	696,63	8,56%
SLB 50_3_FNF	655,0	645,29	1,50%
SLB 50_5_FNF	1000,0	900	11,11%

Table 4.7 Maximum force obtained from the cyclic test

The numerical results are very similar to the experimental results, the error does not exceed the 10%.

The following graphs illustrate the superposition of numerical hysteretic loop and experimental hysteretic loop. However, the numerical curves end at 20 mm, they not give a correct estimation of failure.

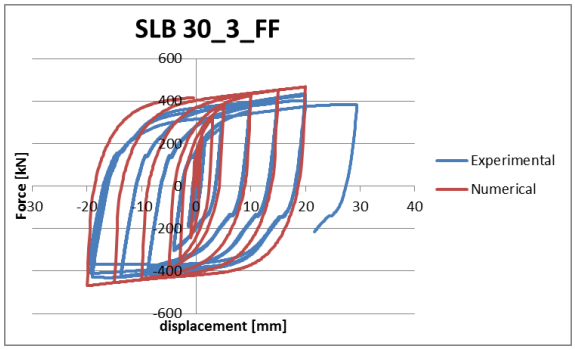

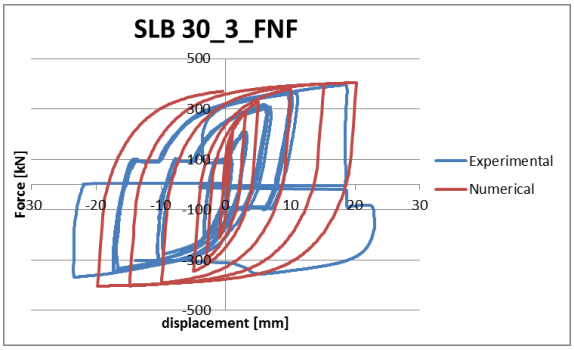

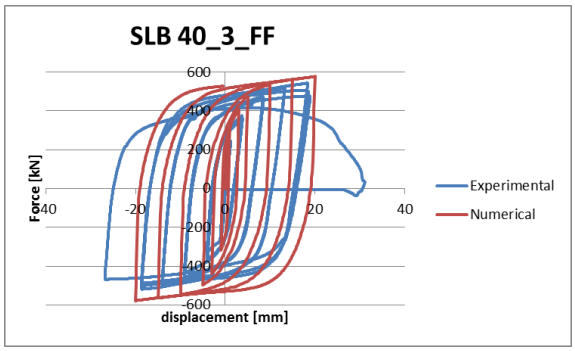

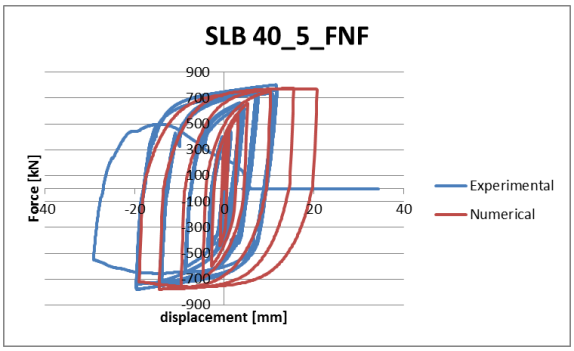

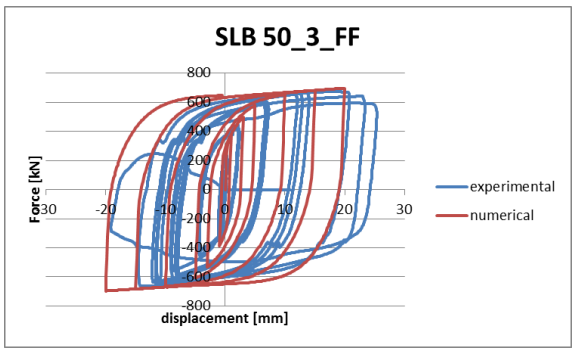

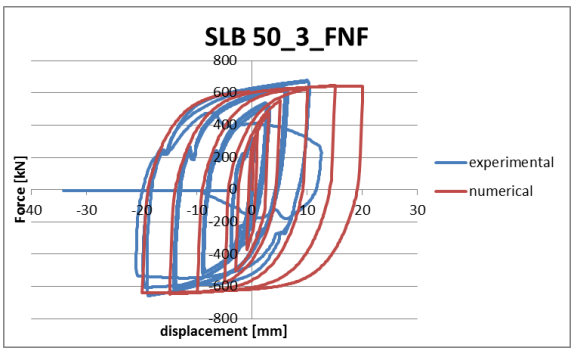

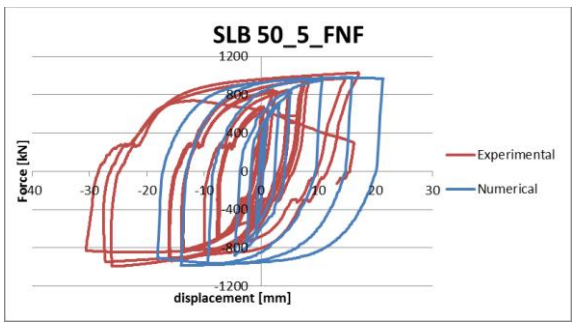

The numerical hysteretic curves appears stable and symmetric in all analysed cases, for both boundary conditions.

The numerical model simulates correctly the real behaviour in the fixed-fixed condition, except for the SLB50_3_FF, where there are accumulated deformations which the program cannot reproduce.

For the fixed-nofixed condition, it is possible to note that the real hysteretic loop is not symmetry, so the numerical curve is larger than this.

The experimental tests and the numerical tests are characterized by the same imposed displacement but the differences, shown before, arise because in the numerical model the displacement is applied directly on the device. Instead in the experimental tests the displacement is applied on the actuator, which transmits it to the device, through the rigid vertical element of the set up.

For this reason another numerical analysis is done, only for the SLB 50_5. The boundary condition remains the same but the load history is different, in particular the new load history is extrapolated from the real displacement of the device recorded during the experimental test, as shown in Figure 4.40. The experimental test has three cycles for each amplitude, the numerical analysis has one cycle for each amplitude.

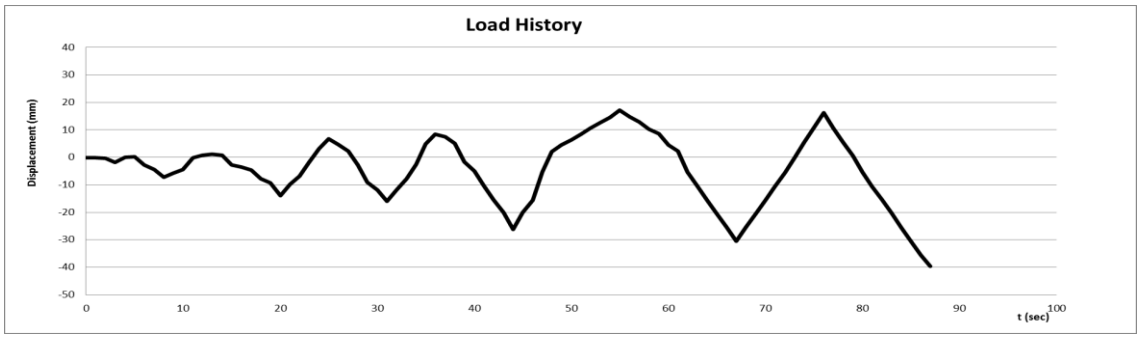

Figure 4.40 Load history of new test on SLB 50_5

The following graph shows the superposition of the numerical result of this new test and experimental result.

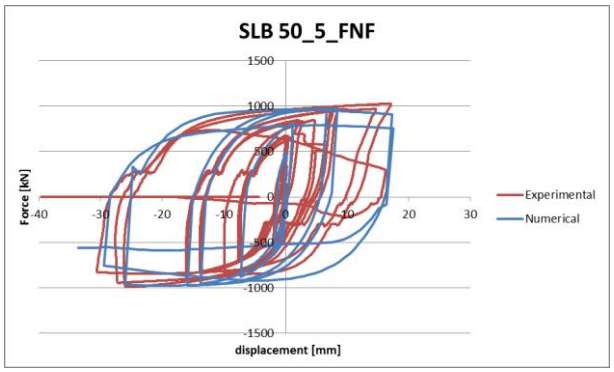

Graph 4-9 Experimental result vs new numerical result

The displacement is equal because it is imposed equal. The maximum numerical force is very closed to the real value, the committed error is around 4%, less than the previous analysis for which is around 11%, as shown in the Table 4.8.

	Fmax		
	[kN]		
	Experimental	Numerical	%
SLB 50_5_FNF	1000,0	962	3,95%

Table 4.8 SLB 50_5 Fmax: experimental result and new numerical result

In terms of elastic stiffness the result is the same of the previous analysis, the values is $k_{el} = 1061\ kN/mm$, the committed error is around 50%.

The equivalent damping ratio, for both experimental model and numerical model, is computed by reference to the greater loop before the failure occurs. It means that for all the experimental device the maximum displacement is around 15 mm, because for 20 mm the failure occurs, except for the SLB 50_5 because the failure occurs for 35 mm, so the considered loos is more than 20 mm. For the numerical models, the equivalent damping ratio refers to the loop characterized by maximum displacement of 15 mm.

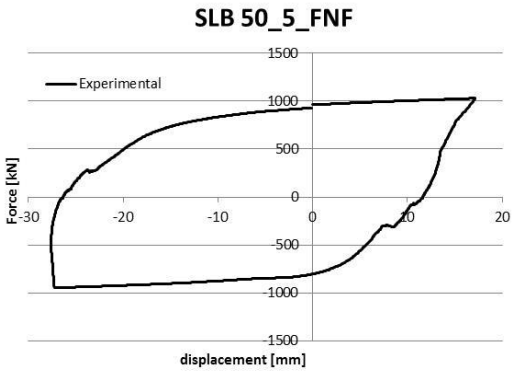

Graph 4-10 SLB 50_5_FNF:Experimental hysteretic loop

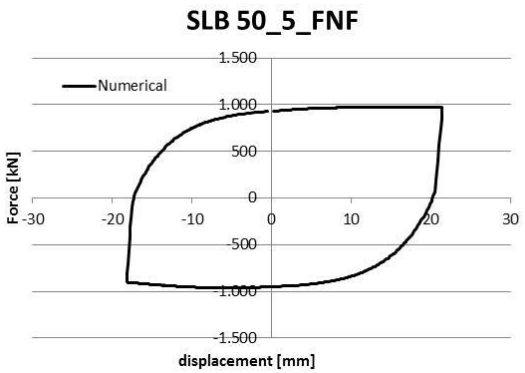

Graph 4-11 SLB 50_5_FNF:Numerical hysteretic loop

The error, which the numerical model commits, is more or less equal to the 20%, as shown in the following table:

	ζeq		
	[-]		
	Experimental	Numerical	%
SLB 30_3_FF	43,20%	48,0%	10,04%
SLB 30_3_FNF	39,74%	46,8%	15,13%
SLB 40_3_FF	48,36%	54,3%	10,96%
SLB 40_5_FNF	45,37%	49,7%	8,77%
SLB 50_3_FF	50,62%	50,5%	0,31%
SLB 50_3_FNF	44,20%	50,1%	11,81%
SLB 50_5_FNF	44,8%	54,39%	17,72%

Table 4.9 Equivalent damping ratio: experimental and numerical results

For the new load history is also evaluated the numerical equivalent damping ratio, but it refers to the loop of the range [-15 mm, 7 mm], which is very closed to the real loop, as shown in the following figure:

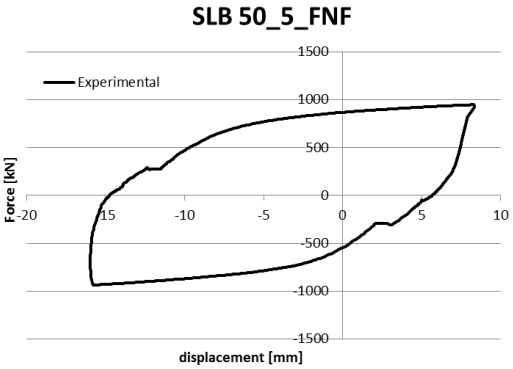

Graph 4-12 SLB 50_5_FNF:Experimental hysteretic loop

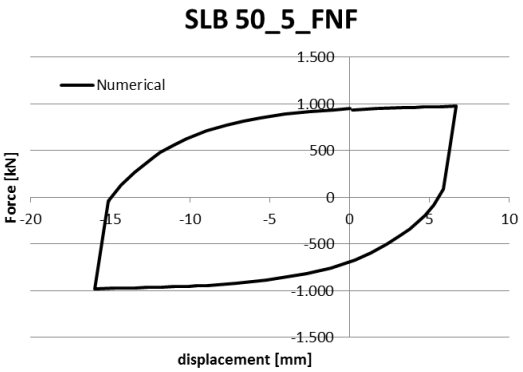

Graph 4-13 SLB 50_5_FNF:New Numerical hysteretic loop

The Table 4.10 shows the comparison between the experimental test and new numerical analysis.

	ζeq		
	[-]		
	Experimental	Numerical	%
SLB 50_5_FNF	42%	46,67%	10%

Table 4.10 Equivalent damping ratio: experimental and new numerical result

The numerical result is more accurate than the previous analysis, in fact the error has halved , about 10%.

4.8.3 Comparison of qualitative description of failure

As regard the development of failure, in the numerical model it is not possible to see the formation of crack at the lateral stiffeners as well as for the real specimen, but the loss of resistance is associated to the buckling of web.

However studying the distribution of plastic deformations and of the tension, it is possible to build the process of failure. It is described previously.

For the numerical model there are two kind of failure, closely related to the deformed shape, which depends on the boundary condition.

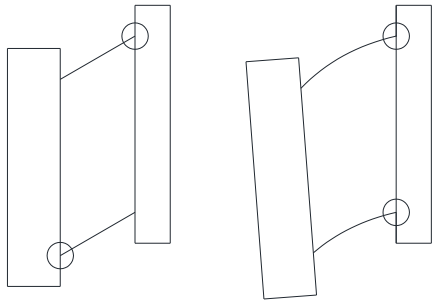

Figure 4.41 (a) fixed-fixed condition, (b) fixed-nofixed condition

As shown in the Figure 4.41, the highlighted points represents the zones where there is concentration of deformation. The figure (a) depicts the fixed-fixed condition, for which the deformed shape is rigid and the plastic deformations are located in the opposite points of lateral stiffeners, the figure (b) represents the fixed-nofixed condition, its deformed shape is no rigid, the left side is free to rotate and the deformations are concentrated at the stiffeners near the fixed side.

It is observed that the different applied load does not influence the mechanism of failure in the numerical model, so it is influenced by only the boundary condition.

The experimental behaviour exhibits two kind of failure process, dependent on the load condition. They are described in the second chapter.

For the experimental behaviour it is possible to see if the formation of the crack precedes the buckling of the web or the two phenomena are concomitant. This aspect is not highlighted by the numerical model, but it permits to predict where the crack could be formed.

5 CONCLUSIONS

The main goals of this thesis are to evaluate the experimental behaviour of Bozzo Shear Link energy dissipation device and to build a numerical model which simulates the real nonlinear behaviour.

The Bozzo Shear Link device represents a good solution to the seismic design of reinforced concrete buildings of low-cost public housing in Peru.

This type of device is inserted as a link in no standard system like rigid system, as masonry wall, or flexible system, and also in conventional system as steel frame and reinforced concrete.

Its simple installation in the structure, between chevron braces and upper beam through a bolted connection, allows its easy substitution, if damage occurs after a strong earthquake.

The manufacturing process allows to obtain the dimensions of cross section very small and low thickness, consequently the device starts to dissipate energy under little displacements.

The main characteristic of these devices is that they are versatile in terms of dimensions, it is possible to change the nonlinear behaviour of them as appropriate, changing the width or thickness of windows.

The aim of experimental campaign was to test the performance of Bozzo Shear Link under the action of a monotonic load and cyclic load. It permits to evaluate the entity of design parameters, in particular the dissipated energy under cyclic load, the reached maximum force and its corresponding displacement.

Five kind of device are tested, with different dimensions of section and different thickness of milled area. For all devices, under cyclic load, the maximum reached displacement is more or less 20 mm, it is in according with the admissible interstory drift.

From the analysis of the experimental results develops the new model of Bozzo Shear Link energy dissipation device, which is characterized by lateral stiffeners larger than the actual lateral stiffeners. This would ensure that the degradation of dissipator starts from the milled area and after affects also the lateral stiffeners.

The research of the numerical model of Bozzo Shear Link device is based on the experimental results, which allows to calibrate the numerical parameters, valid for all device.

The first step is to define the material, which represents the base of nonlinear behaviour of dissipators. In order to define it, the tensile test on the specimen has been performed, from this the constitutive law came out, which is implemented in the program Ansys Workbench.

Furthermore it is necessary to define a plasticity model and its characteristics so that they are equal for all devices. The best plasticity model, which describes the real behaviour of Bozzo Shear Link, is Chaboche's model. Its peculiarity is that it allows the isotropic hardening and kinematic hardening at the same time. It is defined thought two parameters, C_1 and γ_1, that in this thesis are found by trial and error.

The load conditions and boundary conditions performed in the numerical model reproduce the real conditions performed at the laboratory. The load conditions are two: monotonic load and cyclic load. The boundary conditions are two: fixed-fixed condition and fixed-nofixed condition which are realized in the laboratory through the application of tightening moment at the bolds of devices. In particular the right side of device is bolted at the fixed base, so there is the tightening moment, at the left side, where there displacement is applied, the tightening moment is equal to zero, so fixed-nofixed condition, or equal to 2800Nm, so fixed-fixed condition.

All the numerical results are analysed and commented, all the device have a great capacity of energy dissipation. They are compared with the experimental results, in order to prove the confidence of the numerical model and to estimate the error of assessment by the numerical model.

It is observed that, in terms of force and dissipated energy, the numerical model gives acceptable results, the difference not overcomes the 20%.

But it is also noted that the numerical model not shows acceptable results in terms of elastic stiffness, it is not able to represent the real behaviour of Bozzo Shear Link device. In fact, for all devices, the numerical results overestimate the experimental elastic stiffness, making an error greater than 50%. The phenomenon, which causes the low values of elastic stiffness in the

experimental test, is the tolerance in the slotted holes, the numerical model not reproduces this condition.

This is one of aspects that should be investigated in order to define a more precise numerical model of SLB device.

BIBLIOGRAPHY

B. Hortigón, E. N. (June de 2013). Analysis of the state of stresses and plastic strains during the necking process in ductile steels. Zaragoza.

B. Palazzo, L. P. (s.f.). Reduction factors for performance based seismic design of structures with supplemental dampers. Vancouver, Canada.

Bozzo, L. C. (1998). Shear type energy dissipator for the protection of the masonry infill walls. Seattle, Washington: Proceedings of the Sixth U.S. National Conference on Earthquake Engineering.

Cahis, X. T. (2000). An innovative elasto-plastic energy dissipator for the structural and no-structural building protection. Auckland, New Zeland: 12th World Conference on earthquake Engineering.

Clark PW, A. I. (1999). Design procedures for buildings incorporating hysteretic damping devices. *Passive Energy Dissipation and Active Control of Vibrations of Structures*. Cheju, South Korea.

D.R. Sahoo, D. R. (2010). Seismic strengthening of non-ductile reinforced concrete frames using aluminium shear links as energy-dissipation devices. *Engineering Structures 32*.

deust.wordpress.com. (2013). Obtenido de Meshing Methods (ANSYS Meshing).

F. Hurtado, L. B. (s.f.). Numerical and experimental analysis of a shear link energy dissipator for seismic protection of buildings. Beijing-China.

George, P. (1991). Automatic Mesh Generation.

Gheorghe FRUNZĂ, E. N. (2006). HYSTERESIS AND MECHANICAL FATIGUE. Romania: University ”Stefan cel Mare” of Suceava.

https://www.sharcnet.ca/Software/Ansys/16.2.3/en-us/help/wb_msh/msh_metrics.html. (s.f.).

I.Nuzzo. (2016). *Progetto del set-up per la realizzazione di prove statiche di tipo ciclico su dissipatori a taglio "Bozzo's Shear Link" (SLB) mediante macchina universale Italsigma 4 colonne.* Napoli.

Peláez, A. M. (s.f.). Fuerzas de diseño y control de desplazamietos en la norma peruana de diseño sismoresistente.

R.Hill. (1983). *The Matematichal theory of plasticity* . New York:Oxford university Press.

Radim Halama, J. S. (s.f.). Phenomenological Modelling of Cyclic Plasticity. Czech Republic: Department of Mechanics of Materials VŠB-Technical University of Ostrava.

Rai, D. a. (2000). Aluminium shear-link for seismic energy dissipation. *Proc. 12th world conf. on earthqk eng.*

Rezaiee-Pajand, M. (2008). *On the calibration of the Chaboche hardening model and a modified hardening rule for uniaxial ratcheting prediction.* Department of Civil Engineering, Ferdowsi University of Mashhad, Mashhad, Khorasan Razavi, Iran.

S. M. Humayun Kabir, T.-I. Y.-H. (2009). *Characterization of Material Parameters.* London, U.K.

T.T. Soong, B. S. (2002). Supplemental energy dissipation: state-of-art and state-of-the-practice. *Engineering Structures 24*.

Wada A, H. Y. (1999). Passive damping technology for buildings in Japan. Prog Struct Engn Mater.

X. Cahis i Carola, L. B. (2000). Desarrollo de un nuevo disipador de energía para diseño sismorresistente. Análisis numérico y validación experimental de su comportamiento. Barcelona.